Theory of Phonon Thermal Transport in Graphene and Graphite

Submitted by AYMAN SALMAN SHADID ALOFI to the University of Exeter as a thesis for the degree of Doctor of Philosophy in Physics.

June, 2014

I certify that all material in this thesis which is not my own work has been identified and that no material has previously submitted and approved for the award of a degree by this or any other university.

Abstract

Thermal properties of graphene and graphite have been investigated by employing the analytical expressions for the phonon dispersion relations and the vibrational density of states derived by Nihira and Iwata, which are based on the semicontinuum model proposed by Komatsu and Nagamiya. The thermal conductivities of graphene and graphite are computed within the framework of Callaway's effective relaxation time theory. The Normal-drift contribution (the correction term in Callaway's theory) produces a significant addition to the result obtained from the single-mode relaxation time theory, clearly suggesting that the single-mode relaxation time approach alone is inadequate for describing the phonon conductivity of graphene. Its contribution to the thermal conductivity arises from the consideration of the momentum conserving nature of three-phonon Normal processes and is found to be very important for explaining the magnitude as well as the temperature dependence of the experimentally measured results for graphene and graphite. This model has not been implemented before for studying the thermal conductivity of graphene. Also the model has been applied to compute the thermal conductivity of graphene, graphite basal planes, and graphite c-axis. This has further been used to investigate the evolution of thermal properties from graphene to graphite as a function of layer thickness and temperature. The effects of isotopes and tensile strain on the graphene thermal properties have been examined within this model and compared with other available studies.

Dedication

my parents,

my wife, and

my children, Sarah, Abdulaziz, and Lojain.

Acknowledgements

I would like to express my gratitude to my supervisor, professor G. P. Srivastava, whose expertise, understanding, persistent help, and incredible patience, added considerably to my graduate experience. His meticulous comments were an enormous help to me. This thesis would not have materialised without his guidance.

I am deeply grateful to my family for the support they provided through my entire life. In particular, my lovely wife, Tasneem, without whose love, and encouragement, I would not have finished this thesis.

I am indebted to my parents for their faith in me and allowing me to be as ambitious as I wanted. It was under their watchful eye that I gained so much drive and an ability to tackle challenges head on

Last but not least, I would like to offer my special thanks to Taibah University (Madinah, Saudi Arabia) for the financial support and also for granting me a PhD scolarship. The assistance from the Saudi Arabian Cultural Bureau in London is highly appreciated and totally acknowledged.

List of Publications

❶ **A. Alofi** and G. P. Srivastava, *The role of three-phonon Normal processes in the thermal conductivity of graphene*, **MRS Proceedings**, **1404**, mrsf11-1404-w08-02 doi:10.1557/opl.2012.358 (2012).

❷ **A. Alofi** and G. P. Srivastava, *Phonon conductivity in graphene*, **J. Appl. Phys**. **112**, 013517 (2012).

❸ **A. Alofi** and G. P. Srivastava, *Thermal conductivity of graphene and graphite*, **Phys. Rev. B 87**, 115421 (2013).

❹ **A. Alofi** and G. P. Srivastava, *Evolution of thermal properties from graphene to graphite*, **Appl. Phys. Lett. 104**, 031903 (2014).

❺ **A. Alofi** and G. P. Srivastava, *Effect of tensile strain on thermal properties of graphene* , **MRS Proceedings**, **1616**, mrsf13-1661-uu02-08 doi:10.1557/opl.2014.182 (2014).

Contents

List of Figures

List of Tables

Chapter 1

Introduction

1.1 From Carbon to Graphene

Carbon, derived from the Latin *carbo* for coal or charcoal, is one of the oldest and most intriguing elements known to mankind. It has been known and utilised since 5000 BC [1]. It is a member of group IV in the periodic table with symbol C and atomic number six. Most of carbon is found in the form of compounds in earth's crust with a concentration of 180 parts per million (ppm) [2].

Since ancient times, carbon has long been known to exist as graphite and diamond. Two other forms of carbon, spherical fullerenes and linear nanotubes, were discovered in 1985 and 1991, respectively. This has broadened the family of carbon-based systems and drawn the attention of researchers around the world.

In 2004 [3], A. Geim, K. Novoselov, and co-workers, at Manchester University, succeeded in isolating single-layer samples from graphite. In 2010, they were awarded the Nobel prize in Physics for that discovery. The techniques they used to prepare those layers is known as micromechanical exfoliation, or repeated peeling of small mesas of highly oriented pyrolytic graphite, commonly called

the Scotch-tape method. These individually extracted monolayers of graphite are called graphene. The name of graphene, which is recommended by International Union of Pure and Applied Chemistry (IUPAC), is given to a two-dimensional material of sp^2-hybridised carbon atoms with a hexagonal crystal structure. It is considered as the basic building block for several graphitic forms (allotropes), it can be stacked into 3D graphite, rolled into 1D nanotubes or wrapped up to form 0D buckyballs (fullerenes). It is interesting to find that the 2D graphene has been discovered many years after discovering 0D fullerenes and 1D nanotubes. The occurrence of these various allotropes with in part completely opposite properties gives carbon a uniquely interesting feature.

Shortly after the discovery of graphene, it remained a conceptual curiosity and met with distrust since it was long believed that strictly 2D crystals were thermodynamically unstable and thus could not exist in crystalline form. This was so until 2005, when the the Manchester group [4] (Geim's group) and Philip Kim's group [5] at Columbia University independently observed and measured the anomalous quantum Hall effect in graphene. The quantum Hall plateaus were found to be quantized in half-integer values providing, beyond doubt, the evidence of the two-dimensional massless nature of electrons in this system. These findings prompted intense research activities worldwide on graphene.

The exploding interest in graphene has been triggered by its electronic properties. Electrons in graphene have been shown to possess high mobility around 250,000 $\mathrm{cm}^2\mathrm{V}^{-1}\mathrm{s}^{-1}$ [5]. In addition, graphene is a zero-gap material, hence, it is a hybrid between a metal and a semiconductor. Moreover, this zero band gap can be modified by different approaches [6, 7, 8]. Although the Fermi velocity in graphene is $\sim 10^6$ m/s, which is 300 times smaller than the speed of light, electrons behave as the so-called Dirac particles [9].

Considerable amount of heat accumulation during a device operation has to be dissipated. Carbon allotropes are the best candidates for this purpose due to their high thermal conductivity, which is attributed to the C-C being the strongest known covalent bond. In graphene, the $2s, 2p_x, \text{and } 2p_y$ atomic orbitals overlap to form three strong sp^2 bonds, making graphene the hardest (strongest interatomic bonds) possible material; much harder than diamond.

The four common rules [10] accepted for finding nonmetallic crystals with high thermal conductivity are that the crystal should possess (i) low atomic mass, (ii) low anharmonicity, (iii) simple crystal structure, and (iv) strong interatomic bonding. Criteria (i) and (iv) imply a large Debye temperature and thus, high thermal conductivity. Moreover, and according to the predictions of Lindsay *et al.* [11], the combination of a wide frequency gap between acoustic and optic (a-o gap) phonons and the bunching of acoustic branches are among the factors that should entitle the material to be highly thermally conductive. These conditions are believed to be met by graphene: the first experimental measurement for thermal conductivity of graphene is about 5300 W m^{-1} K^{-1} [12]. Throughout this thesis, we will write the thermal conductivity unit as W m^{-1} K^{-1} or $W/m.K$. In general, the reported values for thermal conductivity of graphene at room temperature are in the range 2000 - 6000 $W/m.K$ [13, 14, 15]. These values are remarkably higher than other carbon-based materials such as graphite [16], and diamond [17]. This feature must pave the way for graphene for a wide-potential applications in graphene-based electronic devices.

While the electronic properties of graphene attracted a massive share of interest, studying the thermal and vibrational properties must be given a top priority as well. This is because the applications of the graphene have been envisioned for electronic devices, where thermal management is one of the major factors for

optimum performance and reliability of the electronic components. This point of interest creates a motivational step towards investigating the thermal properties of graphene, which will be addressed in the next section.

1.2 Motivation

Thermal conductivity is a measure of a material's ability to transport heat in the presence of a temperature gradient maintained across it. Phonons are the main heat energy carriers in carbon-based materials. They undergo several scattering mechanisms which primarily deteriorate the material capacity to conduct heat. These mechanisms originate from boundaries, impurities and defects, and other phonons. Phonon-phonon scattering is the only intrinsic scattering mechanism for phonons and divided into two processes, Normal and Umklapp processes. The investigation of the phonon-phonon scattering is very important and also requires complex mathematical treatment.

Several theories have been used for calculating the thermal conductivity of graphene and graphite separately. Moreover, some of the previous studies on graphene thermal conductivity ignored the Normal phonon processes and used different mathematical expressions for the Umklapp phonon processes which require too many fitting parameters for different phonon modes within different ranges of temperatures.

The main motivation for this thesis was to find a simple and a unified theoretical model, with a minimum number of adjustable parameters required for describing the phonon-phonon scattering process, to determine the thermal conductivity in graphene as well as in graphite. We use Callaway's effective relaxation-time theory [18] to incorporate the effect of the Normal phonon processes (N-drift).

Since most thermal properties of graphene are derived from those of graphite and inherit the nature of its crystal, we have employed a semicontinuum model proposed by Komatsu and Nagamiya [19] in 1951. We developed this model to investigate the thermal conductivity in graphene, graphite basal planes, and also along the graphite c-axis. Moreover, this model can describe the evolution process of thermal conductivity and specific heat from graphene to graphite.

1.3 Thesis outline

This thesis is divided into eight chapters along with six explanatory appendices at the end. In chapter 2, the crystal structure of both graphene and graphite is presented. An overview of the physical properties of graphene are introduced including mechanical, optical, electronic, and thermal properties. In addition, preparation methods and potential applications of graphene have been mentioned.

In chapter 3, the concepts of phonons and phonon dispersion relations for layered crystals are introduced. Commonly used theoretical models and experimental techniques for investigating the phonon spectrum of solids are provided. The phonon dispersion relations for graphene and graphite have been analysed and discussed using the analytical expressions of Nihira and Iwata based on the semicontinuum model proposed by Komatsu and Nagamiya. The boundary conditions which distinguish between the phonon dispersion relations of graphene and graphite have been elucidated.

Chapter 4 starts by introducing the definition of the phonon density of states and its key role towards understanding the thermal properties of solids. The Debye model, which is based on the isotropic continuum model, is presented.

The equations for the specific heat of graphene and graphite are expressed. The concepts of the Debye cut-off frequencies and the Debye-like cut-off frequencies are introduced. At low temperatures, the comparison between the phonon density of states and the specific heat for graphene and graphite is addressed and tabulated. Experimental measurements for the specific heat of graphite, at low temperatures, are compared against our theoretical results.

A theoretical background of phonon scattering (phonon-boundary scattering, phonon-defect scattering, phonon-isotope scattering, and phonon-phonon scattering) and heat transport in graphene is presented in chapter 5. The single-mode relaxation-time theory and the Callaway theory (or effective single-mode relaxation-time theory) for thermal conductivity have been discussed within the frame of the Boltzmann transport equation. The importance of Normal phonon-phonon scattering processes within the Callaway theory has been presented. A whole section is devoted to discuss the theoretical results for phonon conductivity in graphene. The mathematical expressions required for evaluating the thermal conductivity of graphene and graphite for both in-plane and out-of-plane modes are presented. The success of the theory in explaining the experimental measurements and in obtaining the correct magnitude and temperature variation of graphene thermal conductivity is described. The variation of the thermal conductivity of graphene samples with their geometrical sizes (micron and nano range) is investigated.

In chapter 6, several studies on tuning factors (tensile/compressive strain, isotopes, and edge roughness) that affect the thermal properties of solids, particularly graphene, are reviewed. The effect of those tuning factors on phonon dispersion relation, phonon density of states, specific heat, and thermal conductivity of graphene has been studied. The concept of the thermal conductivity tensor

has been introduced to calculate the thermal conductivity in graphene, graphite basal planes, and along the graphite c-axis. The effect of the applied compressive strain along graphite c-axis has been investigated. The theoretically obtained results for the thermal conductivity in graphene, graphite basal planes, and along graphite c-axis have been compared against the experimental available measurements. Moreover, the experimental measurements of the thermal conductivity of the isotopically doped graphene have been compared against the theoretical results obtained in this work.

The evolution of thermal properties from graphene to graphite as a function of the number of graphene layers and temperature has been reported in chapter 7. The role of the inter-layer compressional elastic constant and the shear elastic constant in the evolution process has been discussed. The rapid evolution of the thermal properties with the number of layers, approaching the 3D graphite has been shown. The temperature dependencies of the specific heat and in-plane thermal conductivity of single-layer to few-layer graphene is quantified at low temperatures.

A summary of the thesis and suggestions for future work are presented in chapter 8, along with an initial attempt to calculate the thermal conductance of a copper-graphene system. The findings of these calculations have been compared against different theoretical studies and good agreement has been noticed.

Bibliography

[1] A. Krueger, *Carbon Materials and Nanotechnology* (Wiley-VCH, Weinheim, 2010).

[2] G. M. Jenkins and K. Kawamura, *Polymeric Carbons* (Cambridge University Press, Cambridge, UK, 1976).

[3] K. S. Novoselov, A. K. Geim, S. V. Morozov, D. Jiang, Y. Zhang, S. V. Dubonos, I. V. Grigorieva, and A. A. Firsov, Science, **306**, 666 (2004).

[4] K. S. Novoselov, A. K. Geim, S. V. Morozov, D. Jiang, M. I. Katsnelson, I. V. Grigorieva, S. V. Dubonos, and A. A. Firsov, Nature (London) **438**, 197 (2005).

[5] Y. Zhang, Y. Tan, H. L. Stormer, and P. Kim, Nature (London) **438**, 201 (2005).

[6] V. Singh, D. Joung, L. Zhai, S. Das, S. Khondaker, and S. Seal, Prog. Mater. Sci. **56**, 1178 (2011).

[7] V. M. Pereira and A. H. Castro Neto, Phys. Rev. Lett. **103**, 046801 (2009).

[8] V. M. Pereira, A. H. Castr Neto, and N. M. R. Peres, Phys. Rev. B. **80**, 045401 (2009).

[9] A. H. Castro Neto, F. Guinea, N. M. R. Peres, K. S. Novoselov, and A. K. Geim, Rev. Mod. Phys. **81**, 109 (2009).

[10] G. A. Slack, J. Phys. Chem. Solids **34**, 321 (1973).

[11] L. Lindsay, D. A. Broido, and T. L. Reinecke, Phys. Rev. Lett. **111**, 025901 (2013).

[12] A. A. Balandin, S. Ghosh, W. Bao, I. Calizo, D. Teweldebrhan, F. Miao, and C. N. Lau, Nano Lett. **8**, 902 (2008).

[13] D. L. Nika, E. P. Pokatilov, A. S. Askerov, and A. A. Balandin, Phys. Rev. B **79**, 155413 (2009).

[14] J. H. Seol, I. Jo, A. L. Moore, L. Lindsay, Z. H. Aitken, M. T. Pettes, X. Li, Z. Yao, R. huang, D. Broido, N. Mingo, R. S. Ruoff, and L. Shi, Science, **328**, 213 (2010).

[15] S. Ghosh, I. Calizo, D. Teweldebrhan, E. P. Pokatilov, D. L. Nika, A. A. Balandin, W. Bao, F. Miao, and C. N. Lau, Appl.Phys.Lett, **92**, 151911 (2008).

[16] G. A. Slack, Phys. Rev. **127**, 694 (1962).

[17] D. G. Onn, A. Witek, Y. Z. Qiu, T. R. Anthony, and W. F. Banholzer, Phys. Rev. Lett.**68**, 2806 (1992).

[18] J. Callaway, Phys. Rev. **113**, 1046 (1959).

[19] K. Komatsu and T. Nagamiya, J. Phys. Soc. Japan **6**, 438 (1951).

Chapter 2

An Overview on Graphene

2.1 Introduction

The source of the word ”graphite” is the Greek word ”graphein” which means ”to write”. Graphite has been used for writing and drawing since the dawn of history and the first pencils were produced in England in the 15th century. In the 18th century, graphite was considered as an allotrope of carbon [1].

Carbon is polymorphic and one of the most interesting elements from the periodic table due to its wide variety of allotropes which span a large range of physical properties: from hard to soft, conducting to insulating, transparent to opaque. All carbon allotropes of different dimensionalities are known to exist from zero to three dimensions as seen in Fig.2.1. By the end of the 19th century, three carbon allotropes were known: amorphous carbon (carbon/charcoal), graphite , and diamond. In 1952, images of the one-dimensional carbon allotropes were published in the Soviet Journal of Physical Chemistry by L. V. Radushkevich and V. M. Lukyanovich [2]. The next remarkable carbon-related discovery took place in 1985 by H. Kroto *et al.* at Rice University, where they synthesized the first fullerene molecule, C_{60} [3].

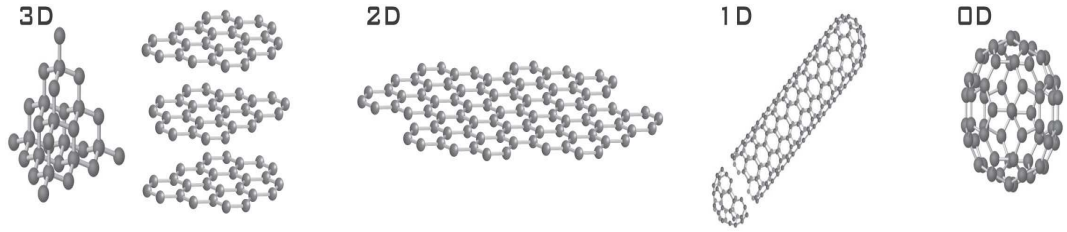

Figure 2.1: Different dimensions for carbon allotropes. From left to right: Three-dimensional (3D) diamond and graphite, two-dimensional (2D) graphene, one-dimensional (1D) nanotubes, and zero-dimensional (0D) buckyballs or fullerene (C_{60}). Reproduced from Ref. [4].

The ability of carbon atoms to form different crystal structures stems from the fact that theses atoms can form several types of valence bonds due to the hybridisation of atomic orbitals. Carbon is the sixth element in the periodic table and thus has six electrons. Two of these occupy the $1s^2$ orbital and are tightly bound to the nucleus. The other four electrons are loosely or more weakly bound and have the electron configuration $2s^2 2p^2$. These electrons are responsible for the formation of covalent bonding with other atoms. The mixing of one of the $2s$ orbitals with $n2p$ orbitals is called sp^n hybridisation. For carbon, there are three available hybridisations: sp, sp^2 and sp^3. Table 2.1 summarises the different types of carbon allotropes based on the hybridised orbitals. For more detailed information on the hybridised orbitals, we refer the reader to Ref. [5].

Table 2.1: Some allotropes of carbon. Reproduced from Ref. [6].

Dimension	0D	1D	2D	3D
Allotrope	C_{60} buckyball	Carbon nanotubes	Graphene	Graphite
Structure	Spherical	Cylindrical	Planar	Stacked planar
Hybridisation	sp^2	sp^2	sp^2	sp^2
Electronic properties	Semiconductor	Metal or semiconductor	Semi-metal	Metal

2.2 Graphene

Graphene was discovered in 2004 by A. Geim and K. Novoselov as the world's first truly two-dimensional material [7]. It is a monolayer of carbon atoms packed in a hexagonal lattice and it is the building block of all other graphitic materials such as graphite, carbon nanotubes and fullerenes. The discovery of graphene led to an explosion of interest for the following two reasons:

(i) The stability of (2D) crystals has been a debatable subject for a long time. It has been pointed out [8, 9] that these low-dimensional crystals are thermodynamically unstable at finite temperatures. This is due to thermal fluctuations which cause the atomic displacements to be larger compared to the interatomic distances and thus the long-range order of those crystals will be broken.

(ii) Quasi-2D films are usually grown on a supporting substrate which has a strong effect on the electrical properties of these films due to its vital role in growth conditions [10]. In contrast, the mechanical exfoliation method which was used to extract graphene layers from graphite results in a graphene layer weakly bonded to the substrate due to weak van der Waals forces and could be isolated easily by just etching away the substrate. The absence of a supporting substrate will lead to minimizing any induced effects from the substrate on graphene and allow for the investigation of the intrinsic properties [11, 12, 13, 14].

Detailed analysis of 2D crystals [15, 16, 17] led to the conclusion that the atomic stability of thin membranes can be attained through their deformation (crumbling) in the third dimension. This crumpling of mono- or few-layer graphene leads to the creation of ripples as shown in Fig. 2.2.

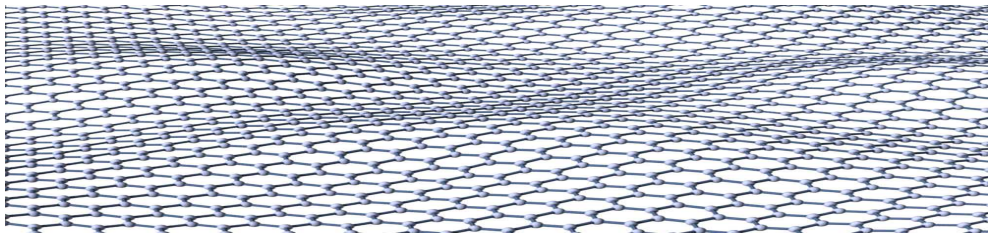

Figure 2.2: Wavy surface of graphene (ripples). Reproduced from [18].

2.2.1 Crystal structure and overview properties

The crystal structure of graphene is shown in Fig. 2.3. It can be considered as the hexagonal Bravais lattice with a basis of two atoms A and B per unit cell. The primitive unit cell can be considered as an equilateral parallelogram with a lattice constant $a = a_{\mathrm{c-c}}\sqrt{3} = 2.46$ Å, where $a_{\mathrm{c-c}}$ is the carbon-carbon bond length. The primitive unit vectors can be defined as

$$\mathbf{a_1} = \left(\frac{a\sqrt{3}}{2}, \frac{a}{2}\right), \mathbf{a_2} = \left(\frac{a\sqrt{3}}{2}, -\frac{a}{2}\right), \tag{2.1}$$

where $|\mathbf{a_1}| = |\mathbf{a_2}| = a$. As shown in Fig. 2.3, there are three vectors, namely $\mathbf{R_1}$, $\mathbf{R_2}$, and $\mathbf{R_3}$ which describe the separation between three nearest carbon atoms of a type (A or B) and defined as

$$\begin{aligned} \mathbf{R_1} &= \left(\frac{a}{\sqrt{3}}, 0\right), \\ \mathbf{R_2} &= \mathbf{R_1} - \mathbf{a_2} = \left(-\frac{a}{2\sqrt{3}}, \frac{a}{2}\right), \\ \mathbf{R_3} &= \mathbf{R_1} - \mathbf{a_1} = \left(-\frac{a}{2\sqrt{3}}, -\frac{a}{2}\right), \end{aligned} \tag{2.2}$$

with $|\mathbf{R_1}| = |\mathbf{R_2}| = |\mathbf{R_3}| = a_{\mathrm{c-c}}$.

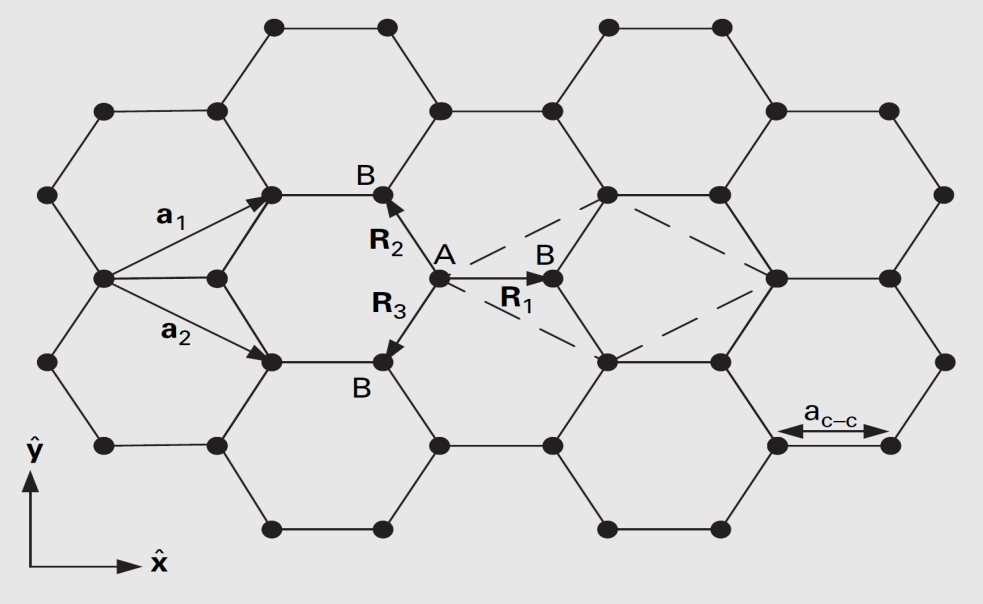

Figure 2.3: Crystal structure of graphene. The equilateral parallelogram (dashed lines) represents the primitive unit cell with a basis of two atoms labeled as A and B. Reproduced from Ref. [6].

The molar area of graphene can be evaluated as follows:

$$A_m = \frac{N_A \cdot A_u}{N_{au}}, \tag{2.3}$$

where A_m is the molar area, $N_A = 6.022 \times 10^{23}$ mole^{-1} is Avogadro's number, A_u is the area of graphene unit cell ($A_u = |\mathbf{a_2} \times \mathbf{a_1}| = a^2\sqrt{3}/2 = 0.0524$ nm^2), and ($N_{au} = 2$) is the number of atoms per graphene unit cell. The number of graphene unit cells per mole is $N_A/N_{au} = 3.011 \times 10^{23}$. Thus, $A_m = 15780.65$ m^2/mole.

The graphene reciprocal lattice is a $90^\circ - \text{degree}$ rotated hexagonal lattice with respect to the direct lattice as shown in Fig. 2.4. The reciprocal lattice vectors $\mathbf{b_1}$ and $\mathbf{b_2}$ can be written as

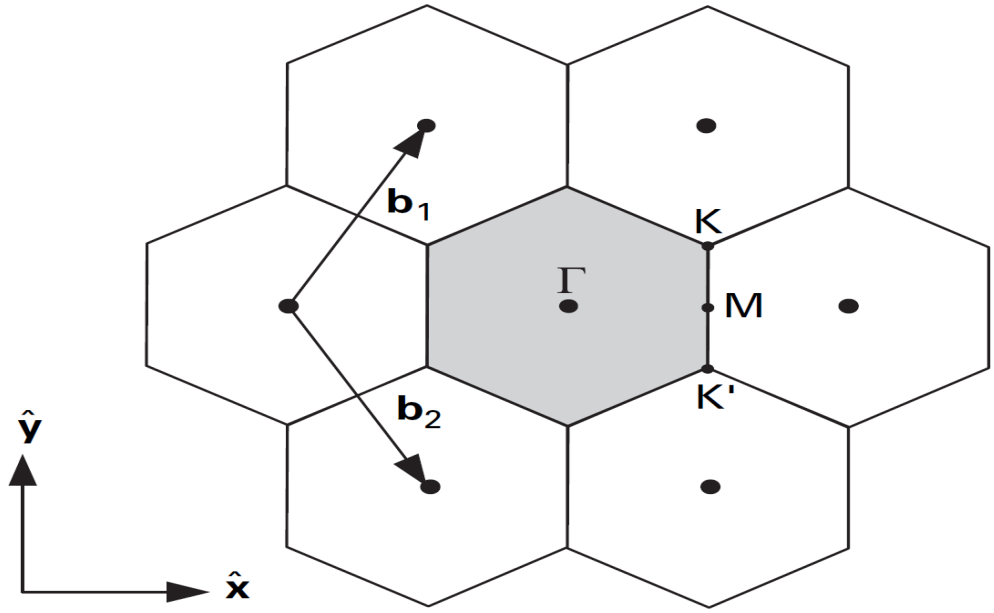

Figure 2.4: The reciprocal lattice of graphene. The first BZ of graphene is the shaded hexagon with the labels for special symmetry points. These points are conveniently identified as Γ, M, and K located at the center, midpoint of the side, and corner of the hexagon respectively. Reproduced from Ref. [6].

$$\mathbf{b_1} = \frac{2\pi}{a}\left(\frac{1}{\sqrt{3}}, 1\right), \mathbf{b_2} = \frac{2\pi}{a}\left(\frac{1}{\sqrt{3}}, -1\right), \tag{2.4}$$

with $|\mathbf{b_1}| = |\mathbf{b_2}| = 4\pi/a\sqrt{3}$. The Brillouin zone (BZ) is illustrated as the shaded hexagon in Fig. 2.4 with sides of length $b_{BZ} = b_1/\sqrt{3} = 4\pi/3a$ and area $A_{BZ} = (2\pi)^2/A_u$. There are three key locations or points of high symmetry in the graphene BZ as shown in Fig. 2.4. These points are conveniently identified as the Γ-point, the M-point, and the K-point. There are six K-points and six M-points within the Brillouin zone and the Γ-point is at the center of the Brillouin zone.

Graphite is composed of a series of stacked parallel graphene layers or basal planes as shown schematically in Fig. 2.5. Within each plane, the carbon atom is

covalently bonded to three adjacent carbon atoms forming the trigonal sp^2 bonds. This bond is σ type with short length and high bonding energy of approximately 5.9 eV [1]. By contrast, the layers themselves are held together by comparatively weak van der Waals forces ($\pi-$bond) (~ 50 meV) [19] arising from the overlap of partially occupied $\mathrm{p_z}$ orbitals perpendicular to the three hybridised orbitals. The bond energies differ by more than two orders of magnitude and the spacing between the layers ($c = 3.35$ Å) is more than twice the spacing between two carbon atoms within the basal plane.

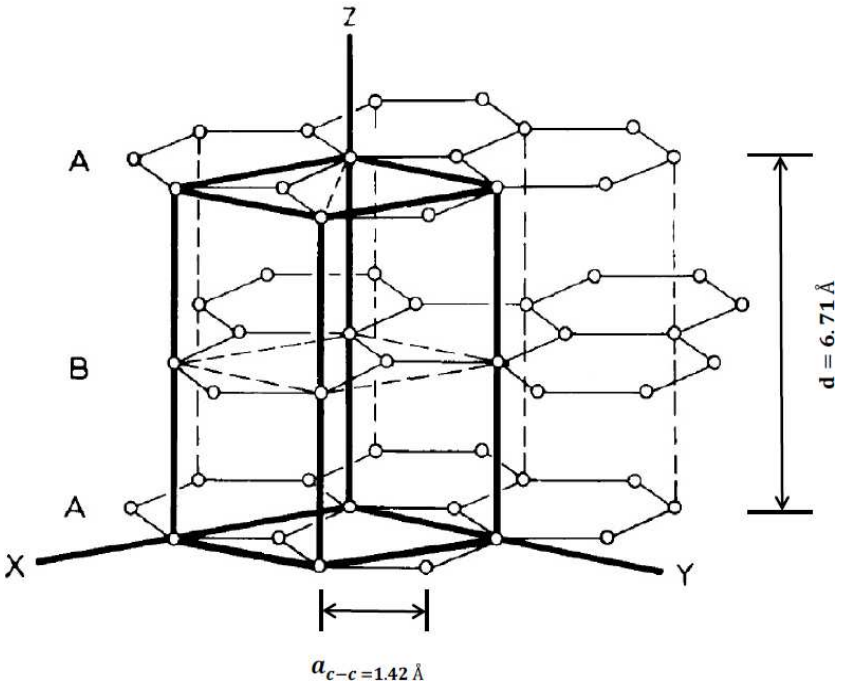

Figure 2.5: The crystal structure of graphite (alpha or Bernal structure) with -ABAB- stacking sequence. The unit cell contains four atoms. The interlayer distance and the bond length are 3.35 Å and 1.42 Å, respectively. Reproduced from Ref.[20].

Figure 2.5 shows the most common and abundant stacking sequence of the graphite crystal which has hexagonal (alpha or Bernal) structure with a -ABAB- stacking order. Almost 85% of all natural graphite has this stacking. The unit cell of this type contains four carbon atoms, two in each layer. The crystal lattice parameters

are: $a = 0.245$ nm and $d = 0.6708$ nm (see Fig. 2.5). In all artificial materials, hexagonal graphite is found to be the most thermodynamically stable structure over a range of temperatures and pressures (T $<\sim$ 2273 K, $P < 130$ kbar) [20]. In the remainder of this thesis we will mean this type of stacking whenever we refer to graphite. The other graphite structure is rhombohedral with the stacking order -ABCABC- and it makes up for about 15% of natural graphite. Its unit cell has six atoms. The crystal lattice parameters for this structure are: $a = 0.2256$ nm and $d = 1.006$ nm. Rhombohedral graphite is thermodynamically unstable and is never found naturally in pure form but in combination with hexagonal graphite. Rhombohedral graphite is a metastable phase, disappearing at elevated temperatures (T > 2273 K) [20] and it usually reverts to the hexagonal structure after a 1573 K annealing process [1].

The in-plane primitive vectors of graphite are the same as those of graphene, the additional lattice vector has only one component in the z-direction which is equal to d for Bernal stacked graphite. The translation vectors of the graphite crystal structure are

$$\begin{aligned} \mathbf{a_1} &= \left(\frac{a\sqrt{3}}{2}, \frac{a}{2}, 0\right), \ |\mathbf{a_1}| = a = 2.46 \text{ Å} \\ \mathbf{a_2} &= \left(\frac{a\sqrt{3}}{2}, -\frac{a}{2}, 0\right), \ |\mathbf{a_2}| = a = 2.46 \text{ Å} \\ \mathbf{a_3} &= (0, 0, d), \qquad\qquad |\mathbf{a_3}| = d = 6.71 \text{ Å} \end{aligned} \tag{2.5}$$

The volume of the graphite unit cell is $V_{cell} = \mathbf{a_1} \cdot (\mathbf{a_2} \times \mathbf{a_3}) = a^2 d\sqrt{3}/2$, this is equivalent to 0.03516 nm^3. For graphite, there are 1.5055×10^{23} unit cells per mole and the molar volume V_m is 5.3 cm^3. mol^{-1}. Figure 2.6 illustrates the BZ of graphite. The reciprocal lattice vectors are

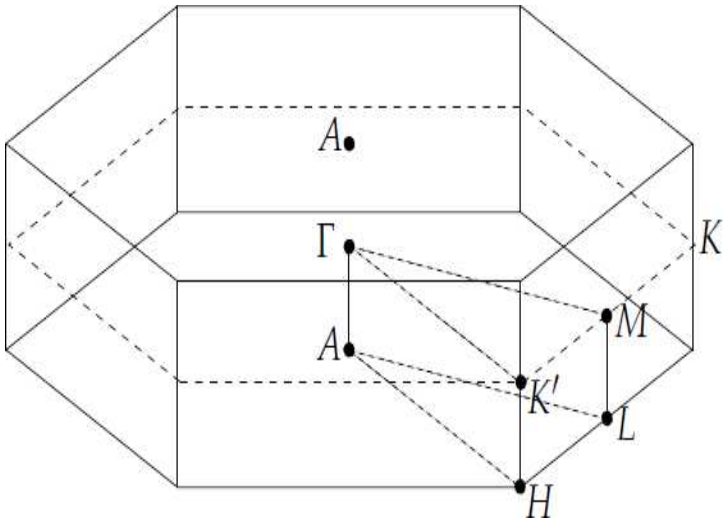

Figure 2.6: The Brillouin zone of graphite with labels for high symmetry points Γ, M, and K. The distances between these points are $\Gamma - \mathrm{K} = 4\pi/3a$, $\Gamma - \mathrm{M} = 2\pi/a\sqrt{3}$, and $\mathrm{K} - \mathrm{M} = 2\pi/3a$ [21]. Reproduced from Ref. [22].

$$\begin{aligned} \mathbf{b_1} &= \frac{2\pi}{a}\left(-\frac{1}{\sqrt{3}}, -1, 0\right), \ |\mathbf{b_1}| = \frac{2\pi}{a}\frac{2}{\sqrt{3}} \\ \mathbf{b_2} &= \frac{2\pi}{a}\left(-\frac{1}{\sqrt{3}}, 1, 0\right), \ |\mathbf{b_2}| = \frac{2\pi}{a}\frac{2}{\sqrt{3}} \\ \mathbf{b_3} &= \frac{2\pi}{d}\left(0, 0, -1\right), \ |\mathbf{b_3}| = \frac{2\pi}{d} \end{aligned} \tag{2.6}$$

2.2.2 Graphene fabrication

Many processes have been developed to synthesize few- to single-layer graphene. One of the primary goals in graphene preparation methods is producing graphene samples with high quality or low density of defects. The methods for synthesis of graphene include mechanical exfoliation of graphite [7, 23], chemical vapour deposition (CVD) [24, 25], epitaxial growth on electrically insulating substrates such as silicon carbide (SiC) [26, 27], chemical reduction of graphite oxide (GO) [28, 29], arc-discharge method [30], other chemical methods [31], and so on. Figure 2.7

provides a schematic illustration of the main graphene preparation methods. Among the aforementioned methods, the arc-discharge method has its exclusive advantages: high quality graphene could be produced in decagram-scale in low cost, no metal catalyst is used, the preparation process is timesaving and facile.

2.2.3 Properties of graphene

2.2.3.1 Specific surface area

With a thin single-atomic-layer, specific surface area of a monolayer graphene is 2630 m^2/g [32]. It has been found that the intrinsic capacitance of graphene is 21 $\mu F/cm^2$ [33] which sets the upper limit of electrical double-layer (EDL) capacitance for all carbon-based materials. A study [34] asserts that graphene is capable of storing an EDL capacitance value of up to 550 F/g. Due to the ultra-high specific surface area of graphene, it can be utilised as ultracapacitor in a wide range of energy storage applications.

2.2.3.2 Mechanical properties

In 2008, Lee *et al.* [36] have measured the elastic properties and intrinsic strength of monolayer graphene. It has been found that the spring constant is in the range $1 - 5$ N/m, a measured Young's modulus of 1 ± 0.1 TPa, an average breaking strength of 55 N/m, and a tensile strength as high as 130 ± 10 GPa. Thus graphene is considered to be the strongest material in the world. The elastic properties of a hexagonal crystal in the layer plane are isotropic and are described by the elastic moduli C_{11} and C_{12} which characterise Young's modulus and Poisson ratio. The constant C_{33} determines Young's modulus in the perpendicular direction, and C_{13} is the corresponding Poisson ratio. The constant C_{44} describes stresses caused by

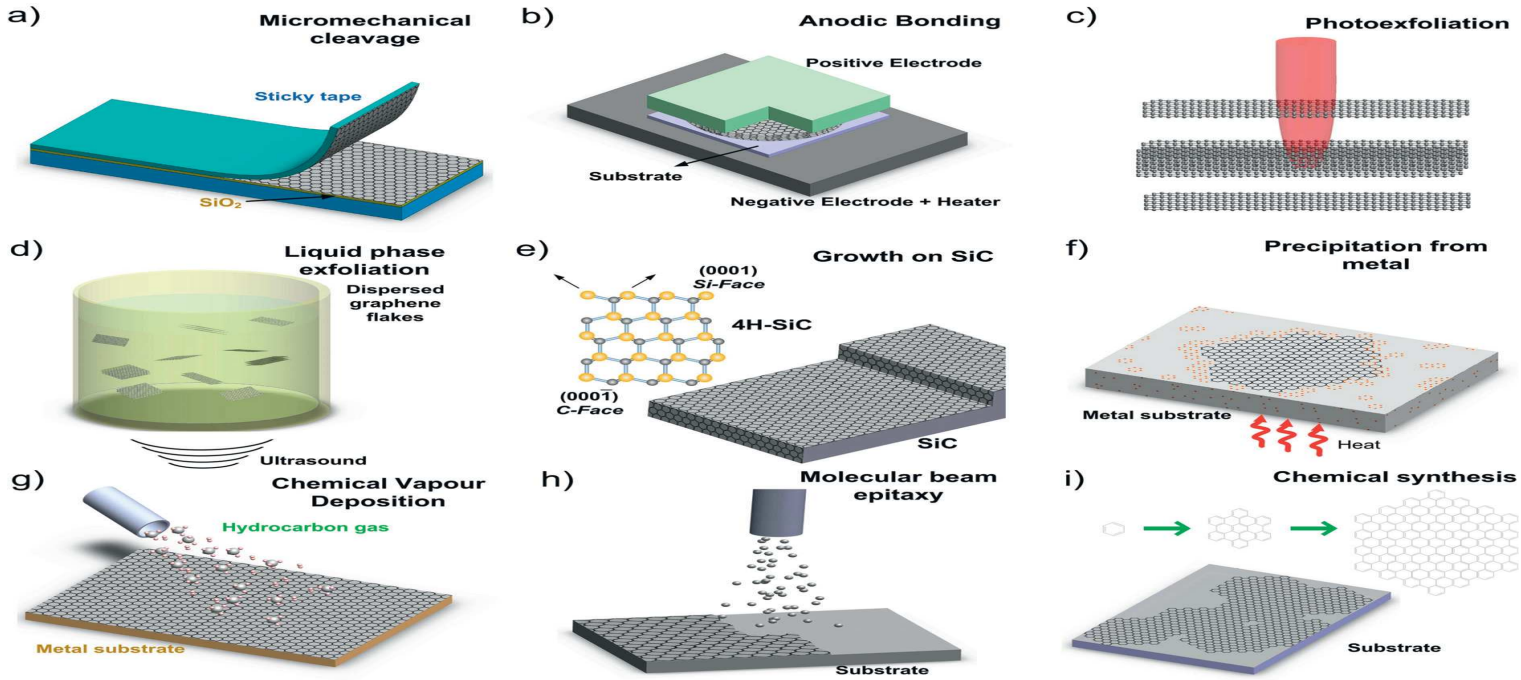

Figure 2.7: Schematic illustration of the main graphene preparation methods. a) Micromechanical cleavage. (b) Anodic bonding. (c) Photoexfoliation. (d) Liquid phase exfoliation.(e) Growth on SiC. Gold and grey spheres represent Si and C atoms, respectively. At high Temperatures, Si atoms dissipiate (arrows) and leave behind carbon atoms that form graphene layers. (f) Segregation/precipitation from carbon accommodating metal substrate. (g) Chemical vapor deposition. (h) Molecular Beam epitaxy. (i) Chemical synthesis using benzene as an ingredient. Reproduced from Ref. [35].

displacements of the layers with respect to each other [37]. The values of these elastic constants are [38, 39]:

$C_{11} = 106 \times 10^{11}\ \mathrm{dyn/cm^2}$

$C_{12} = 18 \times 10^{11}\ \mathrm{dyn/cm^2}$

$C_{13} = 1.5 \times 10^{11}\ \mathrm{dyn/cm^2}$

$C_{33} = 3.65 \times 10^{11}\ \mathrm{dyn/cm^2}$

$C_{44} = 0.425 \times 10^{11}\ \mathrm{dyn/cm^2}$

2.2.3.3 Optical properties

Graphene opacity is significant, it absorbs $2.3 \pm 0.1\%$ of incident white light [40] as can be seen in Fig. 2.8. This is a consequence of its unique electronic structure. The reflectance is negligible, less than 0.1%, which increases up to 2% for ten layers [40, 41].

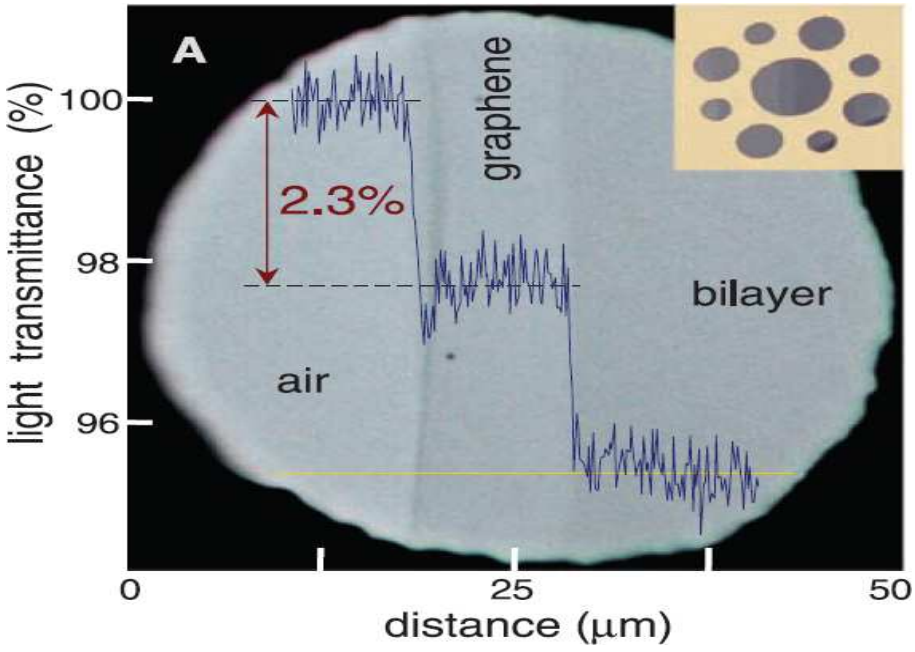

Figure 2.8: Transmitted white light through graphene along the yellow line. The inset shows the sample design. Taken form Ref. [40].

2.2.3.4 Electronic properties

Here, we summarize some of the interesting electronic properties of graphene compared to conventional semiconductors; i.e., silicon, gallium arsenide, etc [42].

(i) Graphene is a zero bandgap semiconductor because the valence band and conduction band meets at the Dirac points (see Fig.2.9). The Dirac points are locations in momentum space on the edge of the BZ.

(ii) The Fermi level in graphene is always within the conduction or valence band whereas it often falls within the bandgap in conventional semiconductors.

(iii) The dispersion relation for graphene is linear while other semiconductors tend to show a quadratic behaviour. This fact was believed to be the cause of many of the impressive electronic properties.

(iv) Graphene is an exactly one-atomic-thick layer. This makes graphene thinner than a traditional 2D electron gas (2DEG) in quantum wells or heterostructures which tends to have a thickness around $5 - 50$ nm. Thus, conducting electrons are constrained in the out of plane direction to a much greater extent than those that conduct through traditional 2DEG.

(v) Ultrahigh electron mobility in suspended graphene was measured and found to be in excess of 2×10^5 cm^{2}V^{-1}s^{-1} at electron densities of $\sim 2 \times 10^{11}$ cm^{-2} [12].

In this thesis however, we will not be interested in the electronic properties of graphene. Our interest is in the calculation of its thermal conductivity.

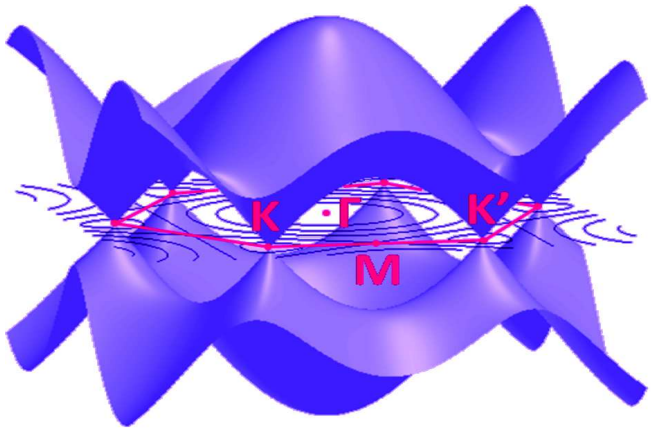

Figure 2.9: Electron band structure of graphene and Brillouin zone. The high symmetry points labeled in red. K and K′ known as the Dirac points which are useful for studying the electronic properties of graphene [43].

2.2.3.5 Thermal properties

As graphite is composed of a series of parallel graphene layers, most of the thermal properties of graphene are inherited from graphite. The specific heat of graphene has not been measured directly but deduced from experimental data available for graphite. At room temperature, the specific heat of graphite $C_{v,p}$ was calculated [38, 44, 45, 46] and compared against experimental data with very good agreement. At room temperature, values of the specific heat of graphene and graphite are similar and estimated to be around $C_v \sim 700$ J kg^{-1} K^{-1} [44]. However, at low temperatures, the specific heat of graphene is higher than that of graphite.

The thermal conductivity of carbon allotropes span a large range of values from ~ 0.01 W/m.K in amorphous carbon to several thousands of W/m.K at room temperature in graphene or diamond [47]. Reported values for thermal conductivity

of graphene at room temperature are in the range of about $2000-6000$ W/m.K [48, 49, 50]. These values are extremely high compared to carbon-based materials such as graphite [51] and diamond [52]. This property of graphene must prove useful for improved reliability and speed of graphene-based electronic and opto-electronic devices. There is a wide range of experimentally measured values for graphene thermal conductivity, this is strongly dependent on the different preparation and characterisation methods [47].

According to some available experimental data, graphene possesses the highest thermal conductivity among solids at room temperature (RT). Balandin *et al.* [53], reported the first experimental measurement of the thermal conductivity in suspended graphene by using optothermal Raman technique. Graphene samples were prepared by the mechanical cleavage of bulk graphite. The thermal conductivity at RT was found to be in the range $4840 - 5300$ W/m.K, exceeding those of the isotopically pure diamond (3320 W/m.K [54]) and single-walled carbon nanotubes (3500 W/m.K [55]).

A following independent study by Cai *et al.* [56] also used the Raman technique to measure the thermal conductivity of graphene. They used a sample of a monolyer graphene grown by CVD onto copper and then suspended over a hole with a sample length of 3.8 μm. It was found that the thermal conductivity exceeded ~ 2500 W/m.K at 350 K, and was as high as ~ 1400 W/m.K at 500 K.

In another experiment, Chen *et al.* [57] used a sample of a monolayer graphene grown by CVD on copper and then suspended over holes with different diameters ranging from 2.9 to 9.7 μm. By using Raman Spectroscopy , they reported thermal conductivity values ranging from $2600 - 3000$ W/m.K near 300 K. Tables 2.2 and 2.3 summarize the experimental results and the theoretical approaches

for evaluating the thermal conductivity of graphene, respectively.

2.2.4 Structural defects in graphene

It can hardly be expected that graphene would have a perfect structure. This is due to a wide range of synthesis methods and preparation conditions. The graphene surface contains structural defects that influence its phononic and electronic spectra and create scattering centers for phonons and electrons. The most important types of structural defects in graphene are shown in Fig. 2.10. The vacancy defect corresponds to the lack of a carbon atom, the Stone-Wales defect which is a transformation of a pair of hexagons into a pentagon-heptagon pair. Other defects are grain boundaries, chemical functionalisation, isotropic impurities (^{13}C) or substitutional defects, and wrinkles or ripples.

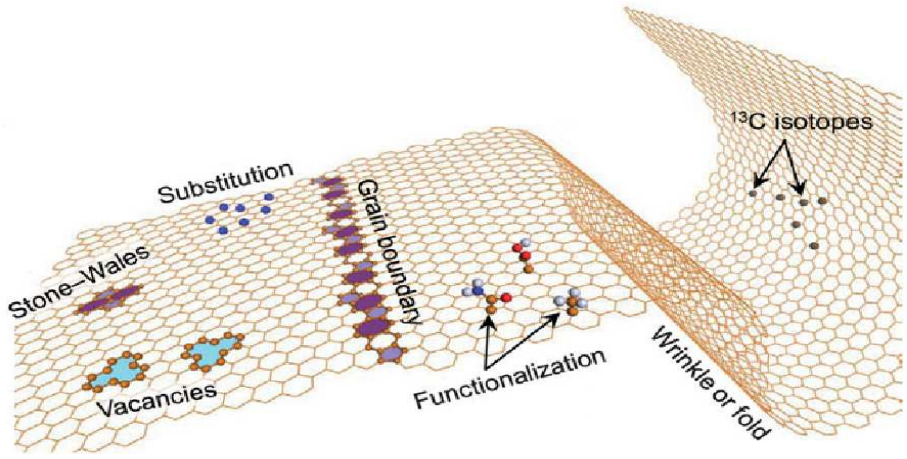

Figure 2.10: Structural defects expected to be presented in graphene (vacancies, grain boundaries, isotopes, Stone-Wales defects, wrinkles or folds, and substitutional and functionalisation defects). Reproduced from Ref. [58].

Table 2.2: Experimental measurements for graphene thermal conductivity by various authors.

Preparation method	Measuring technique	Sample size (μm)	Comments	Temperature K	K $(\mathrm{W/m.K})$	References
Mechanical exfoliation	Seebeck effect	$1.5 - 3.2$(width);$9.5 - 12.5$(length)	supported on SiO_2 substrate	$80 - 300$	630	[49]
Mechanical exfoliation	Raman spectra	≤ 5	suspended	300	$\sim 3080 - 5150$	[50]
Mechanical exfoliation	Raman spectra	≤ 5	suspended	300	$\sim 4840 - 5300$	[53]
CVD	Raman spectra	3.8	suspended	350	~ 2500	[56]
CVD	Raman spectra	$2.9 - 9.7$	suspended	300	$\sim 2600 - 3100$	[57]
Mechanical exfoliation	Raman spectra	44	suspended	300	630	[59]
Mechanical exfoliation	Raman spectra	$2.6 - 6.6$	suspended	325	~ 1800	[60]

Table 2.3: Theoretical calculations for RT graphene thermal conductivity by various authors.

K (W/m.K)	Method	References
$2000 - 5000$	Valence force field, Boltzmann transport equation	[48]
$1000 - 5000$	Relaxation-time approximation	[61]
2400	Boltzmann transport equation	[62]
~ 4000	Elastic-shell model	[63]
$\sim 3800 - 6000$	Semicontinuum model	[64, 65][1]

2.2.5 Graphene melting point

Savvatimskiy [66] has provided a thorough compilation and review of the scientific literature on the melting temperature of graphite. He pointed out that the majority of experimental results report the melting temperature of graphite of $4600 - 5000$ K at pressures above 10 Mpa. Graphene may have a similar melting point as graphite, but this would depend on the mechanisms that give rise to melting process. Atomistic simulations based on an interatomic potential for carbon atoms have been used by Zakharchenko *et al.* [67] for studying the high temperature behaviour of graphene. They found that clustering of Stone-Wales defects are leading to the spontaneous melting around 4900 K. As mentioned earlier, Stone-Wales cluster involves transformation of hexagons into pentagons, heptagons, and octagons as shown in Fig. 2.11.

[1] Our published papers.

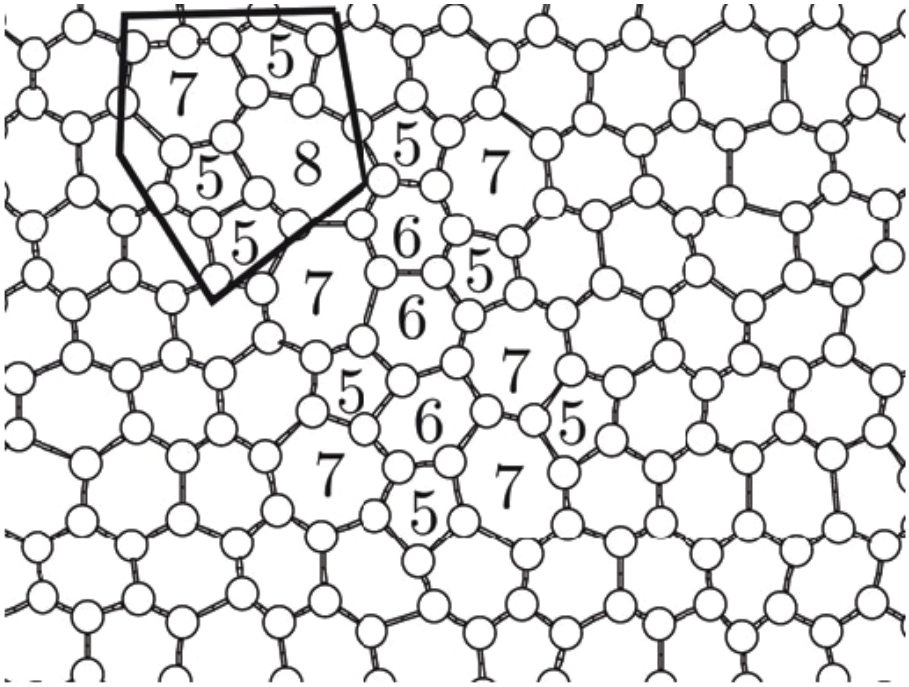

Figure 2.11: Typical transformation within a cluster of Stone-Wales defects. Reproduced from Ref. [67].

2.2.6 Graphene applications

Graphene has strongly attracted scientific and technological interest. It has shown great promise in many applications, such as Field Effect transistors, electrochemical sensors and biosensors, transparent conductive films, graphene-polymer nanocomposites, energy storage and conversion units, and solar cells [58, 68, 69].

2.3 Summary

In this chapter, the crystal structure of graphene and graphite has been described. Graphene fabrication methods have been presented. Useful properties of graphene have been reviewed, including mechanical, optical, electronic, and thermal properties. Graphene structural defects and the process of melting of graphene have

been introduced. Finally, the potential applications of graphene have been mentioned. Being stronger than diamond, more conductive than copper, more flexible than rubber, transparent such that it can be barely seen with the naked eye, this makes graphene an extraordinary material.

Bibliography

[1] H.O. Pierson, *Handbook of Carbon, Graphite, Diamond and Fullerenes: Properties, Processing and Applications* (Noyes Publications , Park Ridge, NJ , 1993).

[2] L. V. Radushkevich and V. M. Lukyanovich. Zurn. Fisic. Chim. **26**, 88 (1952).

[3] H. W. Kroto, J. R. Heath, S. C. OBrien, R. F. Curl, and R. E. Smalley, Nature. **318**, 162 (1985).

[4] M. I. Katsnelson, Mat. Today, **10**, 20 (2007).

[5] R. Saito, G. Dresselhaus, and M. S. Dresselhaus *Physical properties of Carbon Nanotubes* (World Scientific Publishing Company , London, 1998).

[6] H. Wong and D. Akinwande, *Carbon Nanotube and Graphene Device Physics* (Cambridge University Press, New York, 2011).

[7] K. S. Novoselov, A. K. Geim, S. V. Morozov, D. Jiang, Y. Zhang, S. V. Dubonos, I. V. Grigorieva, and A. A. Firsov, Science, **306**, 666 (2004).

[8] N. D. Mermin, Phys. Rev. **176**, 250 (1968).

[9] L. D. Landau and E. M. Lifshitz, *Statistical Physics, Part I* (Pergamon, Oxford, 1980).

[10] J. Stangl, V. Holý, and G. Bauer, Rev. Mod. Phys. **76** , 725 (2004).

[11] J. C. Meyer, A. K. Geim, M. I. Katsnelson, K. S. Novoselov, T. J. Booth, and S. Roth, Nature **446** , 60 (2007).

[12] K. I. Bolotin, K. J. Sikes, Z. Jiang, M. Klima, G. Fudenberg, J. Hone, P. Kim, and H.L. Stormer, Solid State Commun. **146** , 351 (2008).

[13] K. I. Bolotin, K. J. Sikes, J. Hone, H.L. Stormer, and P. Kim, Phys. Rev. Lett. **101** , 096802 (2008).

[14] K. S. Novoselov, D. Jiang, F. Schedin, T. J. Booth, V. V. Khotkevich, S. V. Morozov , and A. K. Geim, Proc. Natl. Acad. Sci. U.S.A. **102** , 10451 (2005).

[15] D. R. Nelson and L. Peliti, J. Phys. **48**, 1085 (1987).

[16] P. Le Doussal and L. Radzihovsky, Phys. Rev. Lett. **69**, 1209 (1992).

[17] D. Nelson, T. Piran, and S. Weinberg, *Statistical Mechanics of Membranes and Surfaces* (World Scientific, Singapore, 2004).

[18] http://www.jameshedberg.com/index.php

[19] M. C. Schabel and J. L. Martins, Phys. Rev. B **46** , 7185 (1992).

[20] B. Kwiecińska and H. I. Petersenb, Int. J. Coal Geol. **57**, 99 (2004).

[21] M. Mohr, J. Maultzsch, E. Dobardžić, S. Reich, I. Milošević, A. Bosak, M. Krisch, and C. Thomsen, Phys. Rev. B **76**, 035439 (2007).

[22] L. Karssemeijerd, *Thermal expansion of carbon structures*, Master's thesis, Radboud University Nijmegen, Netherlands, 2010.

[23] S. Niyogi, E. Bekyarova, M. E. Itkis, J. L. McWilliams, M. A. Hamon, and R. C. Haddon, J. Am. Chem. Soc. **128**, 7720 (2006).

[24] G. D. Yuan, W. J. Zhang, Y. Yang, Y. B. Tang, Y. Q. Li, J. X. Wang, X. M. Meng, Z. B. He, C. M. L. Wu, I. Bello, C. S. Lee, S. T. Lee, Chem. Phys. Lett. **467**, 361 (2009).

[25] E. Dervishi, Z. Li, F. Watanabe, A. Biswas, Y. Xu, A. R. Biris, V. Saini, and A. S. Biris, Chem. Commun. **27**, 4061 (2009).

[26] Z. Y. Juang, C. Y. Wu, C. W. Lo, W. Y. Chen, C. F. Huang, J. C. Hwang, F. R. Chen, K. C. Leou, C. H. Tsai, Carbon, **47**, 2026 (2009).

[27] K. V. Emtsev, A. Bostwick, K. Horn, J. Jobst, G. L. Kellog, L. Ley, J. L. McChesney, T. Ohta, S. A. Reshanov, J. Rõhrl, E. Rotenberg, A. K. Schmid, D. Waldmann, H. B. Weber, and T. Seyller, Nat. Mater. **8**, 203 (2009).

[28] M. J. McAllister, J. L. Li, D. H. Adamson, H. C. Schniepp, A. A. Abdala, J. Liu, M. Herrera-Alonso, D. L. Milius, R. Car, R. K. Prud'homme, and I. A. Aksay, Chem. Mater. **19**, 4396 (2007).

[29] X. Fan, W. Peng, Y. Li, X. Li, S. Wang, G. Zhang, and F. Zhang, Adv. Mater. **20**, 4490 (2008).

[30] K. S. Subrahmanyam, L. S. Panchakarla, A. Govindaraj, and C. N. R. Rao, J. Phys. Chem. C, **113**, 4257 (2009).

[31] M. Choucair, P. Thordarson, and J. A. Stride, Nat. Nanotechnol. **4**, 30 (2009).

[32] M. D. Stoller, S. Park, Y. Zhu, J. An, and R. S. Ruoff, Nano. Lett. **8** , 3498 (2008).

[33] J. Xia, F. Chen, J. Li, and N. Tao, Nat. Nanotechnol. **4** , 505 (2009).

[34] C. Liu, Z. Yu, D. Neff, A. Zhamu, and B. Z. Jang, Nano Lett. **10** , 4863 (2010).

[35] F. Bonaccorso, A. Lombardo, T. Hasan, Z. Sun, L. Colombo, and A. Ferrari, Mat. Today, **15**, 564 (2012).

[36] C. Lee, X. Wei, J. Kysar, and J. Honel, Science, **321** , 385 (2008).

[37] N. A. Abdullaev, Phys. Solid State, **48**, 663, (2006).

[38] T. Nihira and T. Iwata, Phys. Rev. B **68**, 134305 (2003).

[39] O. Blakslee, D. G. Proctor, G. B. Spence, and T. Weng, J. Appl. Phys. **41**, 3373 (1970).

[40] R. R. Nair, P. Blake, A. N. Grigorenko, K. S. Novoselov, T. J. Booth, T. Stauber, N. M. R. Peres, and A. K. Geim, Science, **320** , 1308 (2008).

[41] C. Casiraghi, S. Pisana, K. S. Novoselov, A. K. Geim, and A. C. Ferrari, Appl. Phys. Lett. **91**, 233108 (2007).

[42] D. R. Cooper, B. D'Anjou, N. Ghattamaneni, B. Harack, M. Hilke, A. Horth, M. Hilke, A. Horth, N. Majlis, M. Massicotte, L. Vandsburger, E. Whiteway, and V. Yu, *ISRN* Condensed Matter Physics, **2012**, (2012).

[43] E. Whiteway, *Chemical Vapour Deposition and Raman Spectroscopy of Large Scale C*-12 *and C*-13 *Graphene Monolayers*, Doctoral dissertation, McGill University, Canada, 2012.

[44] N. Mounet and N. Marzari, Phys. Rev. B **71**, 205214 (2005).

[45] L.E. Fried and W. M. Howard, Phys. Rev. B **61**, 8734 (2000)

[46] T. Tohei, A. Kuwabara, F. Oba, and I. Tanaka, Phys. Rev. B **73**, 064304 (2006).

[47] A. Balandin, Nature mater. **10**, 569 (2011).

[48] D. L. Nika, E. P. Pokatilov, A. S. Askerov, and A. A. Balandin, Phys. Rev. B **79**, 155413 (2009).

[49] J. H. Seol, I. Jo, A. L. Moore, L. Lindsay, Z. H. Aitken, M. T. Pettes, X. Li, Z. Yao, R. huang, D. Broido, N. Mingo, R. S. Ruoff, and L. Shi, Science, **328**, 213 (2010).

[50] S. Ghosh, I. Calizo, D. Teweldebrhan, E. P. Pokatilov, D. L. Nika, A. A. Balandin, W. Bao, F. Miao, and C. N. Lau, Appl. Phys. Lett. **92**, 151911 (2008).

[51] G. A. Slack, Phys. Rev. **127**, 694 (1962).

[52] D. G. Onn, A. Witek, Y. Z. Qiu, T. R. Anthony, and W. F. Banholzer, Phys. Rev. Lett. **68**, 2806 (1992).

[53] A. A. Balandin, S. Ghosh, W. Bao, I. Calizo, D. Teweldebrhan, F. Miao, and C. N. Lau, Nano Lett. **8**, 902 (2008).

[54] T. R. Anthony, W. F. Banholzer, J. F. Fleischer, L. Wei, P . K. Kuo, R. L. Thomas, and R. W. Pryor, Phys. Rev. B **42**, 1104 (1990).

[55] E. Pop, D. Mann, Q. Wang, K. Goodson, and H. Dai, Nano Lett. **6**, 96 (2006).

[56] W. Cai, A. L. Moore, Y. Zhu, X. Li, S. Chen, L. Shi, and R. S. Ruoff, Nano Lett. **10**, 1645 (2010).

[57] S. Chen, A. L. Moore, W. Cai, J. W. Suk, J. An, C. Mishra, C. Amos. C. W. Magnuson, J. Kang, L. Shi, and R. S. Ruff, ACS Nano **5**, 321 (2011).

[58] E. Pop, V. Varshney, and A. K. Roy, MRS Bull. **37**, 1273 (2012).

[59] C. Faugeras, B. Faugeras, M. Orlita, M. Potemski, R. R. Nair, and A. K. Geim, ACS Nano **4**, 1889 (2010).

[60] J.-U. Lee, D. Yoon, H. Kim, S. W. Lee, and H. Cheong, Phys. Rev. B **83**, 081419(R) (2011).

[61] D. L. Nika, S. Ghosh, E. P. Pokatilov, and A. A. Balandin, Appl. Phys. Lett. **94**, 203103 (2009).

[62] L. Lindsay, D. A. Broido, N. Mingo, Phys. Rev. B **82**, 161402 (2010).

[63] E. Munoz, J. Lu, and B. I. Yakobson, Nano Lett. **10**, 1652 (2010).

[64] A. Alofi and G. P. Srivastava, J. Appl. Phys. **112**, 013517 (2012).

[65] A. Alofi and G. P. Srivastava, Phys. Rev. B **87**, 115421 (2013).

[66] A. I. Savvatimskiy, Carbon, **43**, 1115 (2003).

[67] K. V. Zakharchenko, A. Fasolino, J. H. Los and M. I. Katsnelson, J. Phys.: Condens. Matter **23**, 202202 (2011).

[68] Y. Zhu, S. Murali, W. Cai, X. Li, J. Suk, J. Potts, and R. S. Ruoff, Adv. Mater. **22**, 3906 (2010).

[69] Y. Shao, J. Wang, H. Wu, J. Liu, Il. A. Aksay, Y. Lina, Electroanalysis **22**, 1027 (2010).

Chapter 3

Phonon Dispersion for Graphene and Graphite

3.1 Introduction

In crystalline solids, the constituent atoms oscillate around their equilibrium positions due to the temperature of that system of atoms. These vibrations are quantized elastic waves and can be seen as quasi particles or phonons. Phonons represent lattice-thermal-vibration waves that propagate through a crystalline solid. Most lattice vibrations have higher frequencies than audible sound, ultrasound, and even hypersound. Figure 3.1 shows the various sound- and vibrational-wave regimes.

In solids, there are two categories of phonons: acoustic phonons denoted with the letter (A) and optical phonons denoted with letter (O). Acoustic phonons arise in crystals when two neighbouring atoms move in-phase with one another, and optical phonons arise when two neighbouring atoms move out-of-phase with one another. Longitudinal acoustic phonons and transverse acoustic phonons are often labelled as LA and TA phonons, respectively. Similarly, for longitudinal op-

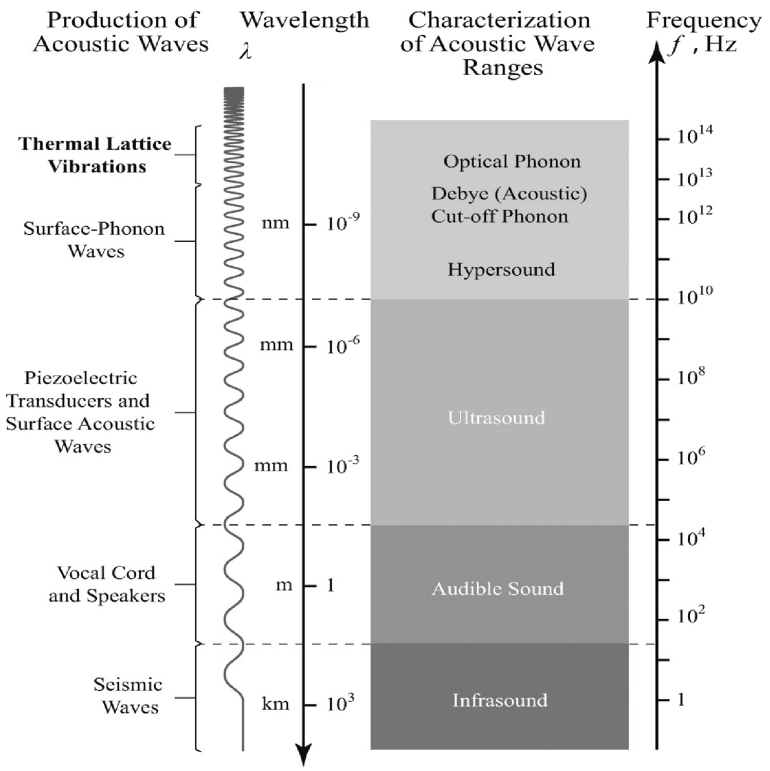

Figure 3.1: Spectra of acoustic- and vibrational- (mechanical- and thermal-) wave regimes. Taken from Ref. [1].

tical and transverse optical phonons there are labelled as LO and TO phonons, respectively, see Fig.3.2. The frequency of acoustic phonons approches zero for long wavelengths while the optical phonons have a minimum frequency even when their wavelength is infinite. For the acoustic and optical branches, there are three polarisations, one longitudinal and two transverse. In general, if there are N atoms per unit cell, there will be three acoustic and $3(N-1)$ optical branches. Some of the characteristics of phonon modes are listed in Table 3.1.

The relationship between the phonon frequency (ω) and its wave vector ($\mathbf{q}$) is termed the phonon spectrum or phonon dispersion relation. The phonon dispersion is a fundamental physical characteristic of solids, from which one can derive

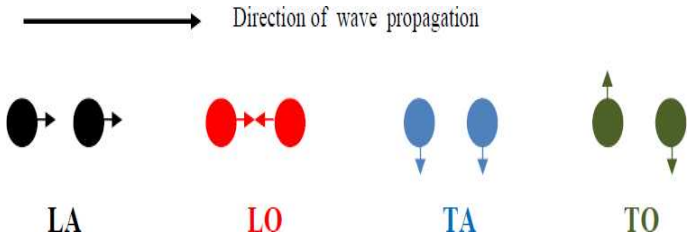

Figure 3.2: Types of atomic motions for two atoms in the unit cell.

Table 3.1: Characteristics of acoustic and optical phonons

Characteristic	**Acoustic polarisation**	**Optical polarisation**
Group velocity	sound waves and linear as $q \rightarrow 0$	smaller than acoustic polarisation
Displacement of adjacent atoms	in-phase	out-of-phase
Largest frequency	towards the edge of the Brillouin zone	higher than acoustic polarisation
Number of polarisations	two transverse and one longitudinal per unit cell	number of atoms per unit cell times 3 minus 3
Dispersion relation	long-wavelength modes have smaller frequency and for $\lambda \rightarrow \infty, \omega \rightarrow 0$	even long-wavelength modes have a finite frequency
External excitement	excited by microwave radiation	excited by infrared radiation and cause time-varying electrical dipole moments

the sound velocity and calculate thermodynamic quantities such as specific heat and thermal conductivity.

3.1.1 Phonons in layered crystals

Unlike the isotropic crystals, layered crystals such as graphite, molybdenum disulphide MoS_2, tantalum disulphide TaS_2, germanium selenide GeSe, or boron nitride BN, show highly anisotropic structural and elastic properties. They are characterized by weakly bonded layers perpendicular to each other. The phonon dispersion of layered crystals are characterized by soft modes (ZA) and high frequency intra-layer modes (LA and TA). The ZA mode is shown in Fig. 3.3 and will be discussed in the next section. The energy difference between the in-plane atomic potential energy and out-of-plane layer potential is a measure of the anisotropy of the material.

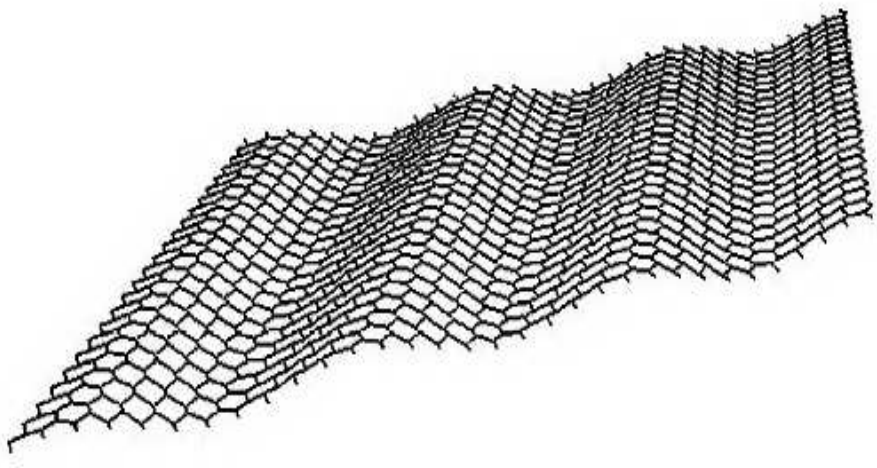

Figure 3.3: ZA bending mode of a graphene layer. Taken from Ref. [2].

3.1.2 Experimental techniques and calculation models

3.1.2.1 Experimental methods

There are several experimental techniques used for the investigation of the phonon dispersion of graphite such as inelastic neutron scattering (INS) [3], electron energy-loss spectroscopy (EELS) [4, 5, 6], and inelastic x-ray scattering (IXS) [7]. Double resonance (DR) Raman scattering technique [8], has been a successful experimental tool to determine the LA and TO phonon dispersion relations of graphene near the Dirac point. Yet, there is no extensive data for the phonon dispersion of graphene compared to graphite but it is expected to be very similar to graphite, since the coupling between planes is relatively very weak.

3.1.2.2 Theoretical models

From a theoretical point of view, the phonon spectrum of a material is principally determined in the harmonic approximation, which is beyond the scope of this thesis. This is done by considering the displacement of each atom from its equilibrium position. The force constant matrix expresses the second derivative of the energy E of the system with respect to the atom displacement u:

$$C_{\alpha i,\beta j}(\mathbf{R}-\mathbf{R}') = \frac{\partial^2 E}{\partial u_{\alpha i}(\mathbf{R})\partial u_{\beta j}(\mathbf{R}')}, \tag{3.1}$$

where $\mathbf{R}$ and $\mathbf{R}'$ are the lattice vectors, i and j indicates the ith and jth atoms of the unit cell, and α and β represent the directions of the coordinate axes. Through the known force constants, the dynamical matrix could be expressed:

$$D_{\alpha i,\beta j}(\mathbf{q}) = \frac{1}{\sqrt{M_i M_j}} \sum_{\mathbf{R}} C_{\alpha i,\beta j}(\mathbf{R}) e^{-i\mathbf{q}.\mathbf{R}}, \tag{3.2}$$

where M_i is the mass of the ith atom. Phonon frequencies at any wave vector $\mathbf{q}$

of the Brillouin zone are the solutions of the eigenvalue problem:

$$\omega^2(\mathbf{q})u_{\alpha i}(\mathbf{q}) = \sum_{\beta j} D_{\alpha i,\beta j}(\mathbf{q})u_{\beta j}(\mathbf{q}). \tag{3.3}$$

For a unit cell containing N atoms, the dynamical matrix will have $3N \times 3N$ components and so there are $3N$ solutions or frequencies ω for each $\mathbf{q}$ written as $\omega_p(\mathbf{q})$, with $p = 1, ..., 3N$.

There are various theoretical models that have been employed by research groups to construct the dynamical matrix and determine the full-phonon dispersion relation in graphite and graphene, including, semicontinuum models [9, 10], Born-von-Kármán model [11], ab-initio methods employing the Perdew-Burke-Ernzerhof generalized gradient approximation (GGA) [2, 7, 12], or the local density function approximation (LDA) [2, 13, 14], fourth- and fifth-nearest neighbor force constant (4NNFC and 5NNFC) approaches [12, 15, 16], and valence force field (VFF) model [17].

The graphene and graphite phonon dispersions are shown in Fig. 3.4. Graphene possesses two carbon atoms in its unit cell, which produces six phonon branches in its phonon spectrum. These branches are: **(i)** in-plane acoustic phonons (LA and TA) and in-plane optical phonons (LO and TO) which corresponds to atomic vibrations within the graphene plane , **(ii)** out-of-plane acoustic phonons (ZA) and out-of-plane optical phonons (ZO) which corresponds to atomic vibtrations along the z-axis and perpendicular to the graphene plane. While the LA and TA modes show the normal linear dispersion around the Γ -point, the ZA mode shows a quadratic ($\omega \sim q^2$) dispersion.

In this thesis, we adopt the the semicontinuum model used by Nihira and Iwata [10],

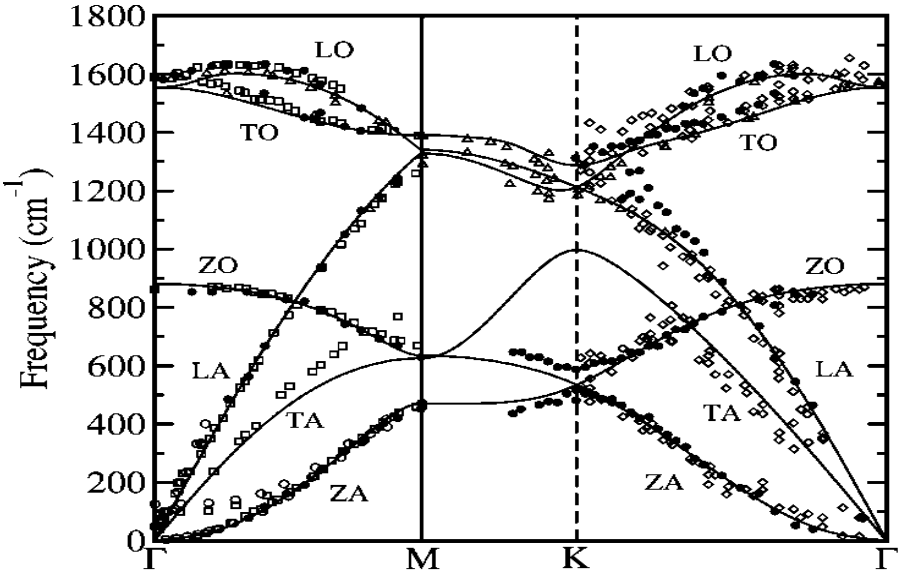

Figure 3.4: GGA *ab initio* phonon dispersions for graphene (solid lines) together with the experimental results for graphite. Reproduced from Ref. [18].

Table 3.2: Reported values for in-plane and out-of-plane phonon velocities by different authors.

Velocity km/s	Komatsu *et al.* [9]	Falkovsky [11]	Klemens *et al.* [19]	Nika *et al.* [20]
v_{LA}	20.1	19.5	23.6	21.3
v_{TA}	12.3	12.2	15.9	13.6
v_{ZA}	–	1.6	5.3	–

which is based on the work by Komatsu and Nagamiya [9], to calculate the phonon dispersion relations for graphene and graphite.

3.1.3 Continuum and semicontinuum models

Matter is formed of molecules, which in turn consist of atoms and subatomic particles. Thus, matter is not continuous. The theory that aims to describe relationships among gross phenomena, ignoring the structure of material on a smaller scale, is known as continuum theory. The continuum model views the crystal as

a continuous medium rather than a periodic array of atoms, see Fig. 3.5.

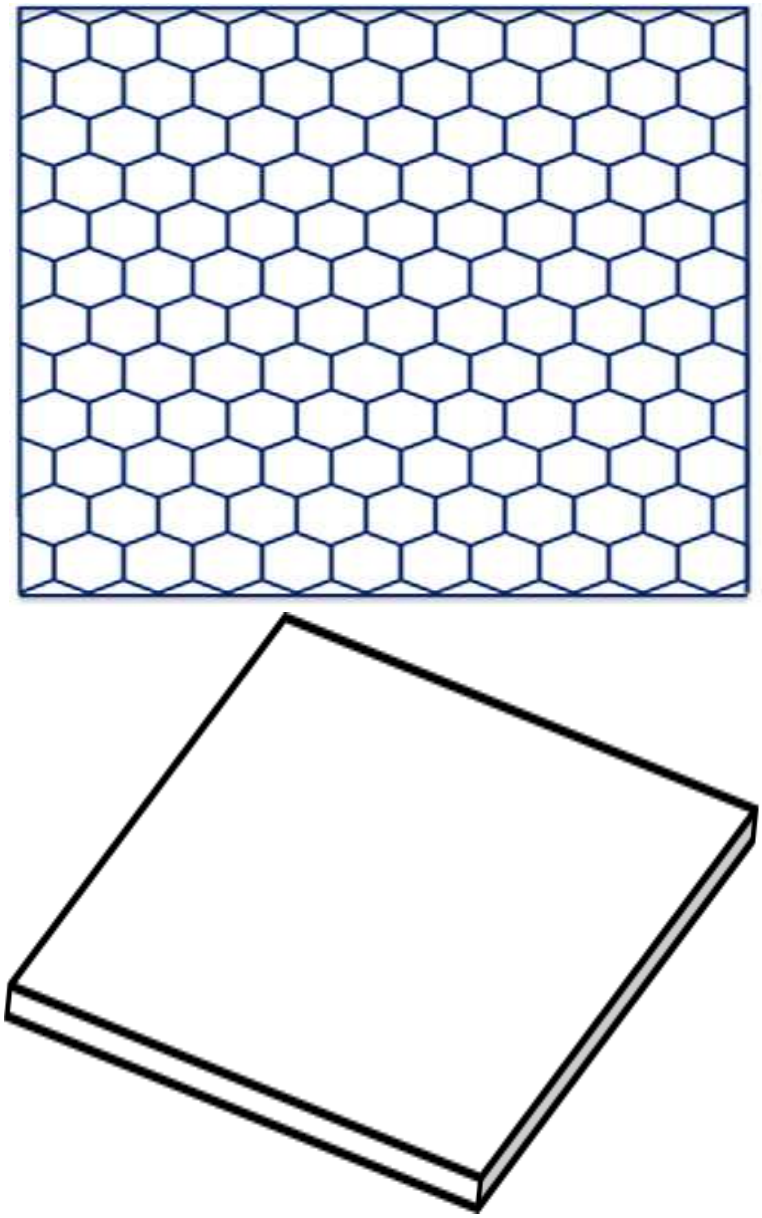

Figure 3.5: Theoretical idealization of monolayer layer graphene sheet. Discrete structure (upper panel) and its equivalent continuum structure (lower panel).

It neglects all the fine detail of atomic level structure and assumes that the discontinuous structure can be replaced by a hypothetical continuum medium.

There is the so-called semicontinuum model which is presented for materials possessing a platelike geometry consisting of layers with submicron thickness [21]. This model accounts for the discrete nature along the thickness direction. The modelling for the nanostructures is divided into three main categories. The models are atomistic, continuum, and hybrid atomistic-continuum model. Being computationally demanding, the atomistic model is limited to systems containing a small number of molecules and atoms. Continuum models are less expensive computationally than the former two approaches. Thus, it has been used by several authors to investigate the phonon dispersion relations for two-dimensional graphite and carbon nanostructures [22, 23, 24].

Anisotropy and dispersion are two distinct but interrlated concepts. While anisotropy is investigated for fixed wave vector and different propagation directions, the dispersion is studied for fixed direction and different wave vectors. The continuum model yields only acoustic branches and non-dispersive relationship between the phonon frequency and its wave vector.

Employing the continuum model in this thesis is based on the assumption that the thermal properties of low-dimensional materials can be described by applying certain boundary conditions to its bulk parameters.

3.2 Graphene and graphite phonon dispersion relations

Phonon dispersion relations for graphite have been investigated by Komatsu and Nagamiya [9] using the semicontinuum model. In this model, graphite crystal is treated as a medium of thin elastic plates spaced equally and connected by shear and elastic compression couplings. For the semicontinuum model employed in the present work, the graphite Brillouin zone is replaced by a circular cylinder with height $q_z^{max} = \pi/c$. For graphene, the Brillouin zone in the q_x–q_y plane could be replaced by a circle of equivalent area with Debye radius q_a determined from the relation $\pi(q_a^{max})^2 = (2\pi)^2/A_u$, where $q_a = (q_x^2 + q_y^2)^{1/2}$ varies over the range $0 - q_a^{max} = 4(\pi/3\sqrt{3})^{1/2}/a_{\mathrm{c-c}}$.

As discussed in section 3.1.2.2, the derivation of the phonon dispersion relations requires writing down the equation of motion for the vibrating atoms in the solid. In continuum theory, the derivation is based on the theory of elasticity. An elastic wave is a mechanical disturbance that propagate through a material causing oscillations of the particles of that material about their equilibrium positions. The general elastic wave equation is given as

$$\rho \frac{\partial^2 u_i}{\partial t^2} = C_{iklm} \frac{\partial^2 u_m}{\partial x_k \partial x_l}, \tag{3.4}$$

where ρ is the density, u_i are the components of the displacement vectors, C_{iklm} is the elastic modulus tensor. If the material is isotropic, then the components of the elasticity tensor must remain the same, regardless of how the rectangular basis is reflected and rotated.

Komatsu [25] has derived analytical expressions for the dispersion relations in

graphite. This derivation is beyond the scope of this thesis, and is presented in Appendix A. Later, Nihira and Iwata [10] have analytically expressed the phonon dispersion relations for graphite, based on the semicontinuum model proposed by Komatsu and Nagamiya [9] as follows:

$$\begin{aligned}
\omega_{\mathrm{LA}}^2 &= v_{\mathrm{LA}}^2(q_x^2+q_y^2)+\frac{4\zeta}{c^2}\sin^2(cq_z/2).\\
\omega_{\mathrm{TA}}^2 &= v_{\mathrm{TA}}^2(q_x^2+q_y^2)+\frac{4\zeta}{c^2}\sin^2(cq_z/2).\\
\omega_{\mathrm{ZA}}^2 &= b^2(q_x^2+q_y^2)^2+4\mu^2\sin^2(cq_z/2)+\zeta(q_x^2+q_y^2).
\end{aligned} \tag{3.5}$$

The subscripts LA and TA refer to vibrations polarised in the basal planes, the former to in-plane longitudinal mode and the latter to in-plane transverse mode, the subscript ZA refers to vibrations of atoms perpendicular to the layer planes (out-of-plane or flexural mode). In these equations, v_{LA} and v_{TA} are the wave velocities, c is the interlayer spacing in graphite, b is the bending elastic parameter which is a measure of the resistance of a graphene layer to bending, ζ, μ, v_{LA}, and v_{TA} are expressed in terms of the elastic constants C_{ij} as well as the volume density ρ as

$$\zeta = C_{44}/\rho; \quad \mu^2 = C_{33}/c^2\rho; \quad v_{\mathrm{LA}} = [C_{11}/\rho]^{1/2}; \quad v_{\mathrm{TA}} = \left[\frac{C_{11}-C_{12}}{2\rho}\right]^{1/2}. \tag{3.6}$$

For two-dimensional (2D) graphene, the phonon dispersion relations can be obtained by applying boundary conditions, $q_z = 0$ as there is no phonon propagation along the z-axis or c-axis. Also $\zeta = 0$ due to the fact that this parameter is describing the motion of graphene layers parallel to each other whereas in graphene there is no such type of movement. Thus, the phonon dispersion relations for graphene after applying theses boundary conditions ($q_z = \zeta = 0$) to Eqs.(3.5) become:

$$\begin{aligned}\omega_{\mathrm{LA}}^2 &= v_{\mathrm{LA}}^2(q_x^2+q_y^2).\\ \omega_{\mathrm{TA}}^2 &= v_{\mathrm{TA}}^2(q_x^2+q_y^2).\\ \omega_{\mathrm{ZA}}^2 &= b^2(q_x^2+q_y^2)^2.\end{aligned} \tag{3.7}$$

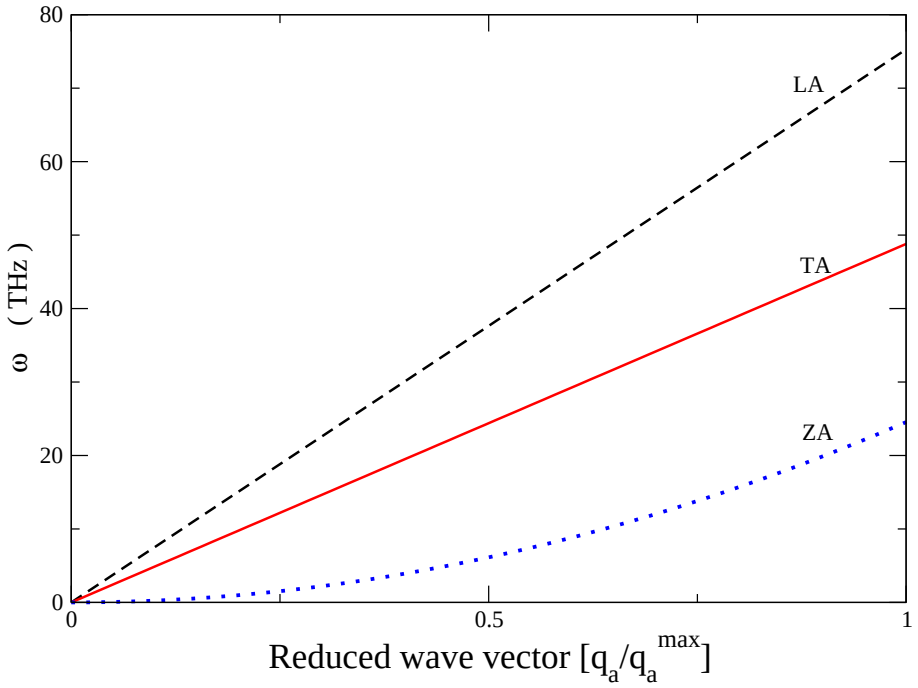

Figure 3.6: Acoustic phonon dispersion of graphene.

Figure 3.6 provides the dispersion curves for graphene, obtained from Eq. (3.7). The parameters related to phonon dispersion relations were taken from the work of Nihira and Iwata [38]. The Debye frequency for each polarisation, taken from Ref. [38] are : $\omega_{\mathrm{D,LA}} = 75.18$ THz, $\omega_{\mathrm{D,TA}} = 48.73$ THz, and $\omega_{\mathrm{D,ZA}} = 24.28$ THz. The quadratic dispersion of the ZA branch can be clearly noted. This is a characteristic property of the phonon dispersions of layered crystals [26].

Figure 3.7 shows the phonon velocity variations with frequency for different modes in graphene (derived from Eq.s (3.7)). The phonon velocity for the LA and TA phonons are constant while the velocity of the ZA phonons shows a non-linear characteristic, resulting from the nonlinear dispersion relation.

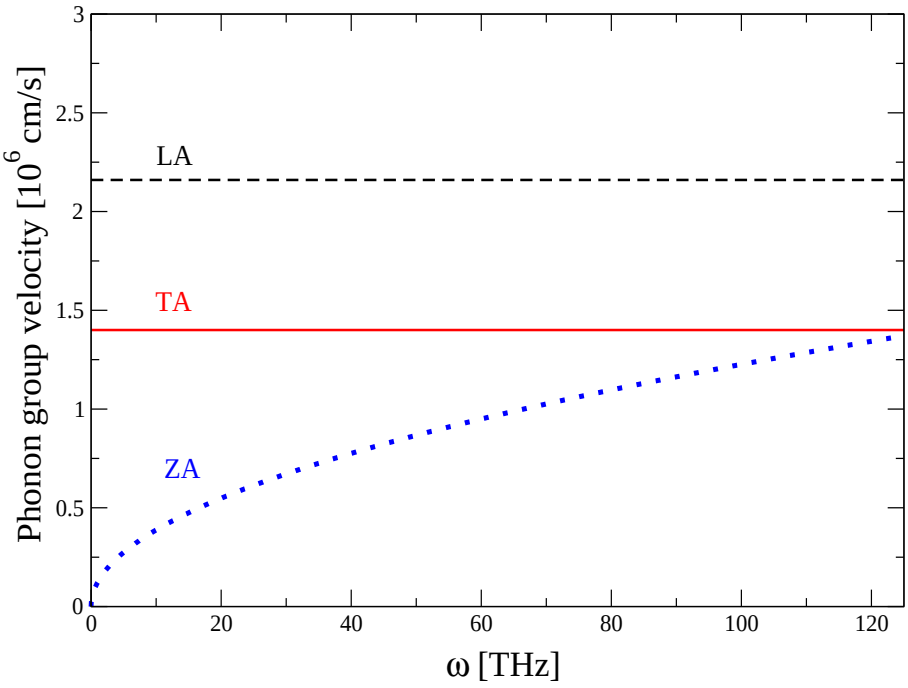

Figure 3.7: Phonon velocity for separate acoustic modes in graphene.

For graphite, there are some cases to be considered. Figure 3.8 shows the dispersion curves of the in-plane and out-of-plane modes along the q_z direction for $q_a = 0$. As can be seen from Eq.(3.5), the dispersion curves for each branch is sinusoidal, and the LA and TA branches are degenerate. It is worth noting that these curves have similar trend to those of one-dimensional dispersion relations, they possess low frequencies, in-plane modes are one order of magnitude lower than those along q_a in Fig. 3.6 for $q_z = 0$.

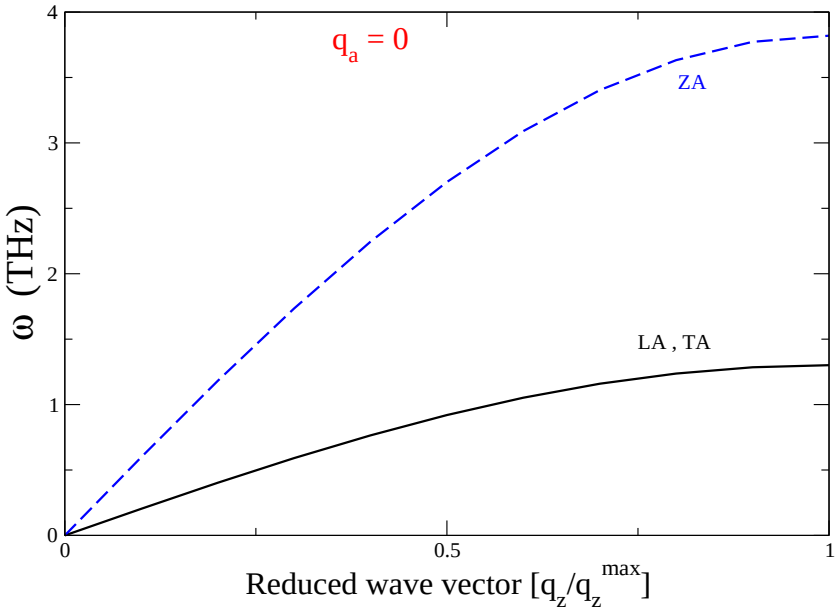

Figure 3.8: Phonon dispersion of the in-plane and out-of-plane acoustic modes for graphite along the q_z direction for $q_a = 0$.

Figure 3.9 represents the dispersion curves of the in-plane and out-of-plane modes along the q_a direction for $q_z = q_z^{max}$. The contribution from the in-plane and out-of-plane modes are relatively not affected comparing to those in Fig. 3.6 for graphene, but gained a non-zero value for $q_z = q_z^{max}$.

The dispersion curves of the in-plane modes for graphene and graphite along the q_a direction are similar. However, the out-of-plane mode is slightly differs, see Fig. 3.10, due to the small effect of ζ which is related to the shearing modulus in graphite. This also can be predicted by Eqs.(3.5) for ω_{ZA} when q_z is set to zero.

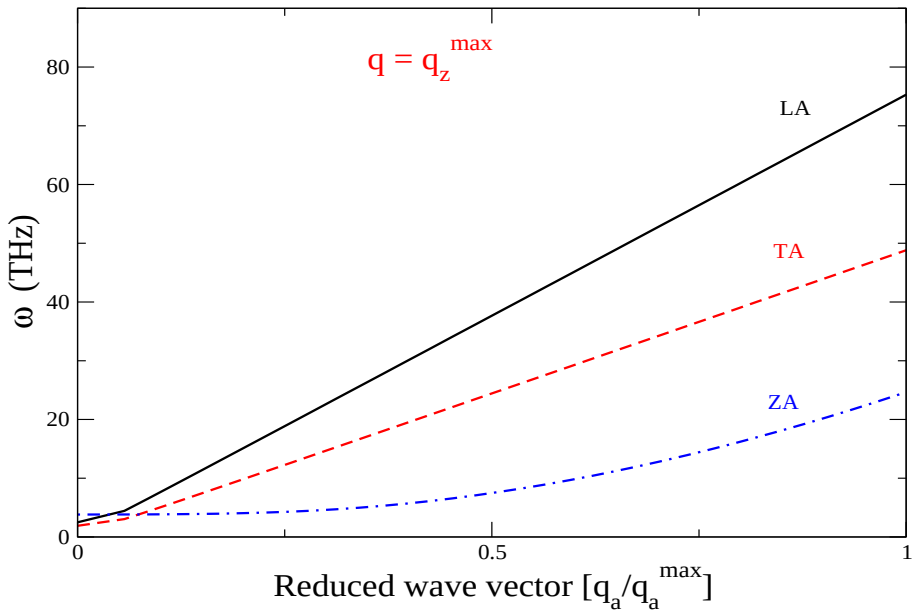

Figure 3.9: Phonon dispersion of the in-plane and out-of-plane acoustic modes along the q_a direction for $q_z = q_z^{max}$.

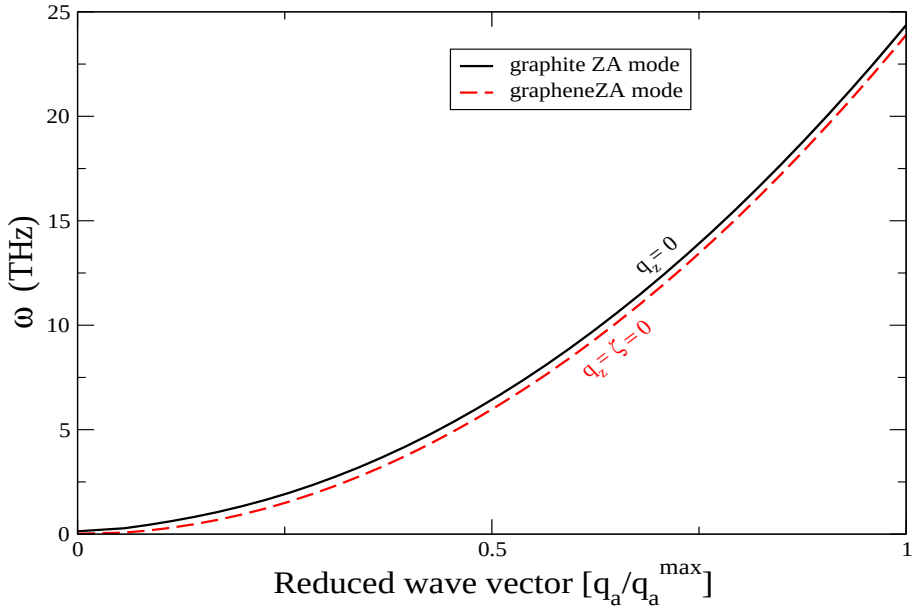

Figure 3.10: Phonon dispersion of the out-of-plane acoustic mode along the q_a direction for graphene and graphite.

3.3 Summary

In this chapter, the phonon dispersion relations for graphene and graphite have been calculated using Nihira and Iwata analytical expressions based on the semi-continuum model proposed by Komatsu and Nagamiya. The equations expressing the dispersion relations for graphite are divided into two independent modes (in-plane and out-of-plane modes) and from each mode there is a contribution parallel and perpendicular to the basal planes. The dispersion relation equations for graphite (3D) can be employed to calculate the phonon dispersion relations for graphene (2D) by applying boundary conditions to the graphite system. Graphene is a 2D system with three acoustic modes, two of them, LA and TA modes, have high velocities of 21.6 km/s and 14 km/s, respectively, and linear phonon dispersion relations . The third out-of-plane mode, ZA mode, possesses a parabolic phonon dispersion relation and a low velocity, which is about one order of magnitude lower than those of LA and TA modes, at low frequencies. The dispersion relations of the in-plane modes along the q_z in graphite are one order of magnitude lower than their contributions along q_a, and they follow similar trend found in a one-dimensional vibrating system. The same argument applies for the contribution from the out-of-plane modes along q_a. The contributions of the in-plane modes along basal planes (q_a) are similar for graphene and graphite. However, the out-of-plane modes contributions along that direction in graphite is very slightly higher than that in graphene. This is due to the presence of additional movement of the layers parallel to each other in graphite which results in a very low shift in the out-of-plane mode frequencies. In general, the acoustic phonon dispersion relations for graphene and graphite are almost similar.

Bibliography

[1] M. Kaviany, *Heat Transfer Physics* (Cambridge University Press, New York, 2008).

[2] N. Mounet and N. Marzari, Phys. Rev. B **71**, 205214 (2005).

[3] R. Nicklow, N. Wakabayashi, and H. G. Smith, Phys. Rev. B **5**, 4951 (1972).

[4] J. L. Wilkes, R. E. Palmer, and R. F. Willis, J. Electron Spectrosc. Relat. Phenom. **44**, 355 (1987).

[5] C. Oshima, T. Aizawa, R. Souda, Y. Ishizawa, and Y. Sumiyoshi, Solid State Commun. **65**, 1601 (1988).

[6] S. Siebentritt, R. Pues, K.-H. Rieder, and A. M. Shikin, Phys. Rev. B **55**, 7927 (1997).

[7] J. Maultzsch, S. Reich, C. Thomsen, H. Requardt, and P. Ordejón, Phys. Rev. Lett. **92**, 075501 (2004).

[8] D. L. Mafra, G. Samsonidze, L. M. Malard, D. C. Elias, J. C. Brant, F. Plentz, E. S. Alves, and M. A. Pimenta, Phys. Rev. B **76**, 233407 (2007).

[9] K. Komatsu and T. Nagamiya, J. Phys. Soc. Japan **6**, 438 (1951).

[10] T. Nihira and T. Iwata, Phys. Rev. B **68**, 134305 (2003).

[11] L. A. Falkovsky, Phys. Lett. A **372**, 5189 (2008).

[12] L. Wirtz and A. Rubio, Solid State Commun. **131**, 141 (2004).

[13] J-A. Yan, W. Y. Ruan, and M. Y. Chou, Phys. Rev. B **77**, 125401 (2003).

[14] O. Dubayand and G. Kresse, Phys. Rev. B **67**, 035401 (2003).

[15] H. Wang, Y. Wang, X. Cao, M. Fenga, and G. Lana, J. Raman. Spectrosc. **40**, 1796 (2009).

[16] M. Mohr, J. Maultzsch, E. Dobardžić, S. Reich, I. Milošević, A. Bosak, M. Krisch, and C. Thomsen, Phys. Rev. B **76**, 035439 (2007).

[17] V. Perebeinos and J. Tersoff, Phys. Rev. B **79**, 241409 (2009).

[18] N. Mounet and N. Marzari, Phys. Rev. B **71**, 205214 (2005).

[19] P. G. Klemens and D. F. Pedraza, Carbon, **32**, 735 (1994).

[20] D. L. Nika, E. P. Pokatilov, A. S. Askerov, and A. A. Balandin, Phys. Rev. B **79**, 155413 (2009).

[21] C. T. Sun and H. Zhang, J. Appl. Phys. **93**, 1212 (2003).

[22] L. Chico, R. P-Álvarez, and C. Cabrillo, Phys. Rev. B **73**, 075425 (2006).

[23] H. Suzuura and T. Ando, Phys. Rev. B **65**, 235412 (2002).

[24] S. V. Goupalov, Phys. Rev. B **71**, 085420 (2005).

[25] K. Komatsu, J. Phys. Soc. Japan **10**, 346 (1955).

[26] H. Zabel, J. Phys. CM **13**, 7679 (2001).

Chapter 4

Phonon Density of States and Specific Heat

4.1 Introduction

By the density of states of a system we usually mean the number of allowed energy levels of that system per unit energy interval. It plays a central role in most phenomena involving lattice vibrations, particularly specific heat and thermal conductivity. The reason for its importance is quite simple, when one investigates which states of a system are occupied, the energy of the states is the controlling factor. Thus, the total energy of that system can be derived from a knowledge of the density of states. The phonon density of states (PDOS) for graphite and graphene is the subject of this chapter. The PDOS equations for graphite were expressed by Komatsu and Nagamiya and then reproduced by Nihira and Iwata. We have employed the latter formulae in our calculations towards evaluating the PDOS and specific heat for graphene and graphite.

4.1.1 General concept of phonon density of states

The subject of phonon density of states is discussed in detail in many references (see, for example, Ref. [1] and Ref. [2]). The phonon density of states of a system is very sensitive to its physical dimensions.

4.1.1.1 Three-dimensional case

For three dimensional system, the density of states $D(\omega)$ can be obtained by the number of phonon frequencies in a frequency interval enclosed by two surfaces of constant phonon frequencies ω and $\omega + \mathrm{d}\omega$ in **q**-space. If we consider an area element $\mathrm{d}S_\omega$ on the ω = constant surface and with perpendicular distance $\mathrm{d}q_\perp$ between the surfaces of constant ω and constant $\omega + \mathrm{d}\omega$, then the volume of this shell bounded by these constant frequency surfaces is

$$\int_{\text{shell}} \mathrm{d}^3 q = \int \mathrm{d}S_\omega \mathrm{d}q_\perp. \tag{4.1}$$

Since the gradient $\nabla_{\mathbf{q}}\omega$ is normal to the frequency surface, then the difference in frequency $\mathrm{d}\omega$ between the two surfaces connected by $\mathrm{d}q_\perp$ is

$$\mid \nabla_{\mathbf{q}}\omega \mid \mathrm{d}q_\perp = \mathrm{d}\omega.$$

Thus the volume element in **q**-space is

$$\mathrm{d}S_\omega \mathrm{d}q_\perp = \mathrm{d}S_\omega \frac{\mathrm{d}\omega}{\mid \nabla_{\mathbf{q}}\omega \mid} = \mathrm{d}S_\omega \frac{\mathrm{d}\omega}{\mathbf{v}_g},$$

where $\mathbf{v}_g = \nabla_{\mathbf{q}}\omega$ is the phonon group velocity. A unit volume in **q**-space is $N_0\Omega/(2\pi)^3$, where N_0 is the number of unit cells and Ω is the unit cell volume. Since density of states is the number of **q**-values contained in volume of the system, then the density of states can be written as

$$D(\omega) = \frac{N_0\Omega}{8\pi^3} \int \frac{\mathrm{d}S_\omega}{\mid \mathbf{v}_g \mid}. \tag{4.2}$$

where the integration is carried over constant ω-surface. This can be generalised as

$$D(\omega) = \frac{N_0\Omega}{8\pi^3}\sum_p \int \frac{\mathrm{d}S_\omega}{\mid \nabla_{\mathbf{q}}\omega \mid}, \tag{4.3}$$

where p denotes phonon polarisation index. At some q points, the phonon group velocity equals zero ($\mathbf{v}_g = 0$). These points are singularity points or Van-Hove singularities contained in the density of phonon states curves.

4.1.1.2 Two-dimensional case

For a two-dimensional system, the phonon density of states is given by [1]

$$D(\omega) = \frac{A}{4\pi^2}\sum_p \int \frac{l_\omega}{\mid \nabla_{\mathbf{q}}\omega \mid}, \tag{4.4}$$

where A is the area of the unit cell and l_ω is a length of constant frequency in the two-dimensional system.

4.1.1.3 One-dimensional case

Considering a linear monatomic chain with length L containing N atoms, the phonon density of states is given by [1]

$$D(\omega) = \frac{L}{\pi}\frac{1}{\mid \nabla_{\mathbf{q}}\omega \mid} \tag{4.5}$$

$$= \frac{2N}{\pi}\frac{1}{\sqrt{\omega_{\max}^2 - \omega^2}}, \tag{4.6}$$

where $\omega_{\max}$ is the highest frequency.

4.1.2 Debye model

The Debye model is introduced by Peter Debye in 1912 as a method for evaluating the the specific heat of a solid. This model is based on the following assumptions:

(i) A solid is considered as an isotropic elastic continuum medium.

(ii) Only the mean phonon velocity is taken into account for all the three acoustical modes in the phonon spectrum and no distinction is made between phase and phonon group velocity.

(iii) A linear dispersion $\omega = vq$ is assumed for all modes lying within a sphere of radius q.

(iv) The thermal energy of a system is stored in acoustical modes.

(v) The atoms of a solid have $3N$ phonon modes in the range $0 \leq \omega \leq \omega_D$, where the maximum frequency ω_D is called the Debye frequency . This stems from the fact that phonons with half wave lengths less than the interatomic distance cannot be propagated through the crystal. These phonon modes are contained in a volume (sphere) in **q**-space with Debye radius q_D.

(vi) For each phonon frequency, a phonon density of states $D(\omega)$ is associated with it such that $D(\omega)\mathrm{d}\omega$ represents the number of vibrational modes between the frequency interval ω and $\omega + \mathrm{d}\omega$.

(vii) The vibrating atoms are treated as independent harmonic oscillators with energy ϵ given by quantum mechanics $\epsilon_n = (n + 1/2)\hbar\omega$ rather than by classical result $\langle\epsilon\rangle = k_B T$, where n is a positive integer or zero and k_B is Boltzmann's constant.

(viii) The total energy of the crystal from the acoustical modes of vibration is given by

$$E = \int_0^{\omega_D} \langle \epsilon(\omega) \rangle D(\omega) \mathrm{d}\omega \tag{4.7}$$

Using (ii) and (iii) assumptions, then $\mathrm{d}S_\omega = 4\pi q^2 \mathrm{d}q$. Substituting this into Eq.(4.3), we get

$$D(\omega) = \frac{V\omega^2}{2\pi^2} \sum_p \frac{1}{v_p^3}, \tag{4.8}$$

where $V = N_0\Omega$, is the volume of the crystal. If we define an average phonon velocity v by

$$\begin{aligned} \frac{1}{v^3} &= \left\langle \frac{1}{v_p^3} \right\rangle \\ &= \frac{1}{3}\left[\frac{1}{v_l^3} + \frac{2}{v_t^3}\right] \end{aligned} \tag{4.9}$$

then

$$\frac{3}{v^3} = \sum_p \frac{1}{v_p^3}$$

which yield

$$D(\omega) = \frac{3V\omega^2}{2\pi^2 v^3} \tag{4.10}$$

According to assumption (v), Debye frequency ω_D can be obtained by the following equation

$$3N = \int_0^{\omega_D} D(\omega)\, \mathrm{d}\omega \tag{4.11}$$

ω_D and q_D can be then obtained from Eq.(4.11) as follows

$$\omega_{\mathrm{D}} = \left(\frac{6\pi^2 N v^3}{V}\right)^{\frac{1}{3}} \tag{4.12}$$

$$q_{\mathrm{D}} = \frac{\omega_D}{v} = \left(\frac{6\pi^2 N}{V}\right)^{\frac{1}{3}} \tag{4.13}$$

For 2D and 1D systems, the PDOS are

$$D(\omega) = \frac{A\omega}{2\pi v^2}, \tag{4.14}$$

and

$$D(\omega) = \frac{2L}{a\pi\sqrt{w_D^2 - \omega^2}}, \tag{4.15}$$

respectively. According to Debye's model, $D(\omega) \propto \omega^{D-1}$ for D-dimensional system.

4.2 Phonon density of states for graphite and graphene

The phonon density of states functions per mole $D_p(\omega)$ for all branches are derived by Komatsu [3]. The reader is referred to Appendix B for more details. They are given by the following analytic expressions:

$$\mathrm{p} = \mathrm{LA}, \mathrm{TA} \text{ and } \omega \leq \omega_z : \quad D_p(\omega) = \frac{A_m \omega}{\pi^2 v_p^2} \sin^{-1}\left(\frac{\omega}{\omega_z}\right), \tag{4.16}$$

$$\mathrm{p} = \mathrm{LA}, \mathrm{TA} \text{ and } \omega \geq \omega_z : \quad D_p(\omega) = \frac{A_m \omega}{2\pi v_p^2}, \tag{4.17}$$

p = ZA and $\omega \leq \omega'_z$:

$$D_p(\omega) = \frac{A_m}{2\pi^2 b}\left(\frac{\omega}{\omega'_z}\right)\int_0^{\sin^{-1}\{[1+(\zeta^2/4b^2\omega^2)]^{-1/2}\}}\left[1-\left(\frac{\omega}{\omega'_z}\right)^2\left(1+\frac{\zeta^2}{4b^2\omega^2}\right)\sin^2\phi\right]^{-1/2}d\phi, \tag{4.18}$$

p = ZA and $\omega \geq \omega'_z$:

$$D_p(\omega) = \frac{A_m}{2\pi^2 b}\left(1+\frac{\zeta^2}{4b^2\omega^2}\right)^{-1/2}\int_0^{\pi/2}\left[1-\left(\frac{\omega'_z}{\omega}\right)^2\left(1+\frac{\zeta^2}{4b^2\omega^2}\right)^{-1}\sin^2\phi\right]^{-1/2}d\phi, \tag{4.19}$$

where ω_z and ω'_z are defined in Eq.(4.20) and Eq.(4.21) respectively. Here, there are Debye-like cut-offs frequencies (DLCFs) and Debye cut-offs frequencies (DCFs) for each mode (in-plane and out-of-plane modes). The DLCFs are assigned to the external modes (the motion of graphene layers parallel and perpendicular to each other), whereas the DCFs belong to the internal modes (the motion of atoms with respect to each other).

The motion of graphene layers generate very low frequencies: motions produce in-plane modes, where layers move parallel to each other (shearing mode), and out-of-plane mode where they move perpendicular to each other (compressional mode). The DLCFs for the in-plane and out-of-plane modes are $\omega_z = 1.30$ THz and $\omega'_z = 3.82$ THz, respectively. The DLCF for the out-of-plane mode is approximately three times the value of the in-plane modes. These DLCFs are expressed as

$$\omega_z = \frac{2\zeta^{1/2}}{c} = 2\left(\frac{C_{44}}{c^2\rho}\right)^{1/2}. \tag{4.20}$$

$$\omega'_z = 2\mu = 2\left(\frac{C_{33}}{c^2\rho}\right)^{1/2}. \tag{4.21}$$

Table 4.1 lists the physical constants of graphite used throughout this thesis.

Table 4.1: Physical constants of graphite as presented in the work of Nihira and Iwata (Ref.[4]).

C_{11}	106×10^{11}	$\mathrm{dyn/cm^2}$
C_{12}	18×10^{11}	$\mathrm{dyn/cm^2}$
C_{13}	1.5×10^{11}	$\mathrm{dyn/cm^2}$
C_{33}	3.65×10^{11}	$\mathrm{dyn/cm^2}$
C_{44}	0.425×10^{11}	$\mathrm{dyn/cm^2}$
b	3.13×10^{-3}	$\mathrm{cm^2/s}$
c	3.3544×10^{-8}	cm
ρ	2.26	$\mathrm{g/cm^3}$
V_m	5.30	$\mathrm{cm^3/mol}$
υ_l	2.16×10^{6}	$\mathrm{cm/s}$
υ_t	1.40×10^{6}	$\mathrm{cm/s}$
ζ	1.88×10^{10}	$\mathrm{cm^2/s^2}$
μ	1.20×10^{13}	$\mathrm{s^{-1}}$
ω_z	8.18×10^{12}	$\mathrm{rad/s}$
ω_z'	2.40×10^{13}	$\mathrm{rad/s}$

The DCFs for in-plane modes $\omega_{D,i}$ and out-of-plane modes $\omega_{D,c}$ are

$$\omega_{D,i} = \sqrt{\frac{4\pi v_i^2 N_A}{A_m} + \frac{\omega_z^2}{2}}, \tag{4.22}$$

$$\omega_{D,c} = \frac{4\pi b N_A}{A_m}, \tag{4.23}$$

where N_A is Avogadro's number, the index i could be used for LA or TA modes, and c indicates the out-of-plane mode. The values of these Debye cut-off frequencies are: $\omega_{\mathrm{D,LA}} = 75.18$ THz, $\omega_{\mathrm{D,TA}} = 48.73$ THz, and $\omega_{\mathrm{D,ZA}} = 24.28$ THz.

Figure 4.1 (upper panel) shows the phonon density of states for graphene and graphite computed from Eqs. (4.16) – (4.19). For graphene, the layer planes are uncoupled, which means $\mu = 0$, $\zeta = 0$, and then setting $q_z = 0$ will reflect the two-dimensional nature of the graphene crystal. It can be noticed clearly that the density of states of ZA phonons is larger than that of LA and TA phonons up to approximately 24 THz and also shows a constant behaviour. Figure 4.1 (lower panel) displays the phonon density of states for graphite, which obtained with values of μ and ζ listed in Table 4.1.

It can be observed that it only is the ZA mode in graphite which bears its finger print for its PDOS and distinguishes graphite from graphene. The peak for the ZA mode occurs at $\omega_z = 3.82$ THz. The PDOS for the in-plane modes in graphene as well as in graphite shows linear behaviour for low as well as high range of frequencies. This reflects the 2D nature of graphene. The PDOS for the ZA mode in graphene is constant with respect to ω over a whole range of frequencies. On the contrary, the PDOS for the ZA mode in graphite shows a nonlinear behaviour up to ω_z, this is due to the interaction force between the stacked graphene layers.

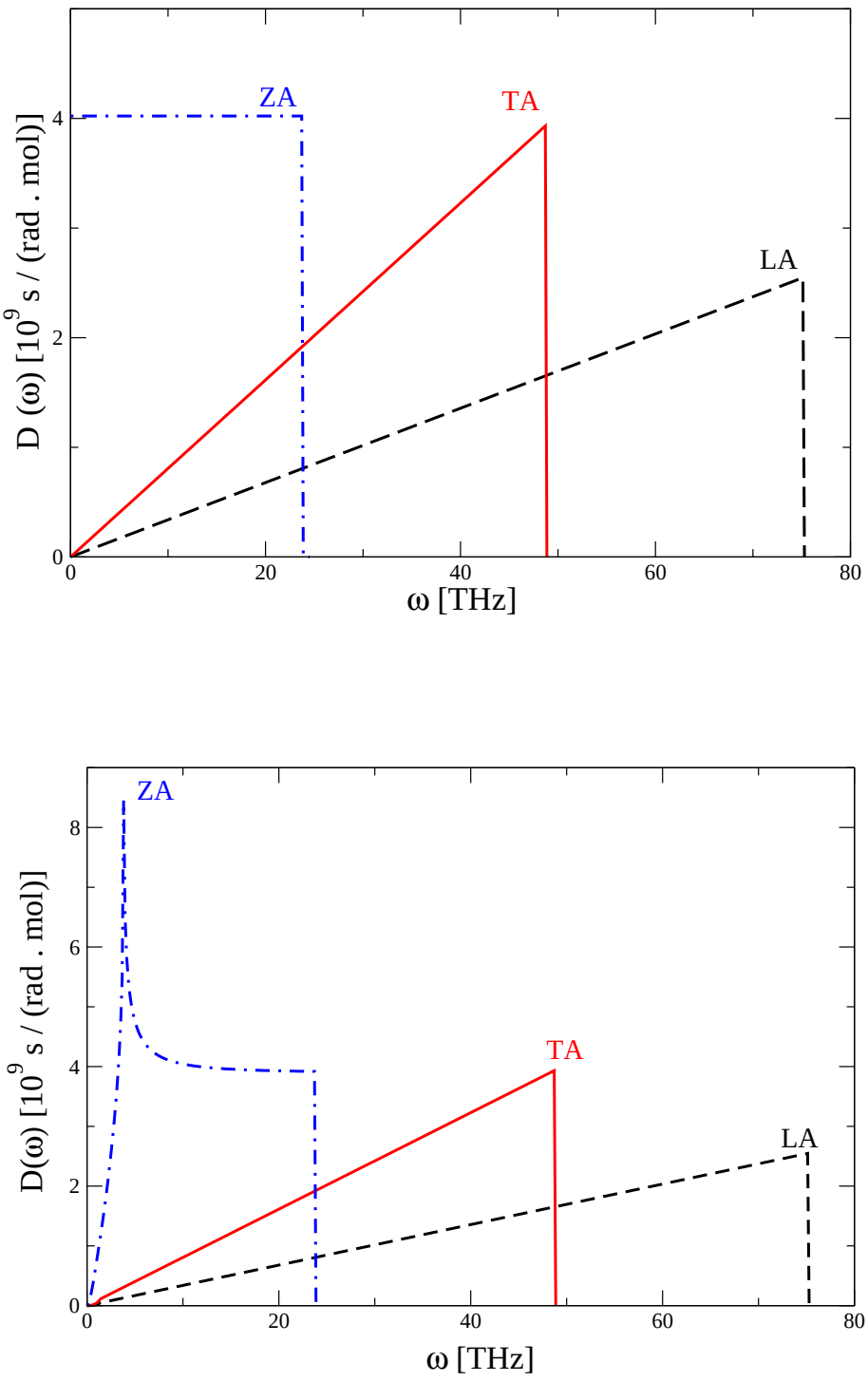

Figure 4.1: Phonon density of states, for separate branches for graphene (upper panel) and graphite (lower panel).

Figure 4.2 presents the total PDOS for both graphene and graphite. They share the same values of the PDOS for $\omega \geq 23.63$ THz. For graphite, the total PDOS approaches zero when ω approaches zero, but for graphene the total PDOS has a nonzero value as ω tends to zero.

At very low frequencies, the PDOS for the total in-plane modes (LA+TA) are illustrated in Fig.4.3. It shows the linear and nonlinear behaviour of the PDOS with respect to ω for graphene and graphite, respectively. For the in-plane modes in graphite, $D(\omega) \propto \omega^{2.5}$ whereas for graphene the PDOS still maintains its linearity behaviour ($D(\omega) \propto \omega$). The nonlinearity trend in graphite could be attributed to the shearing modes that result from the movement of the graphene layers parallel to each other.

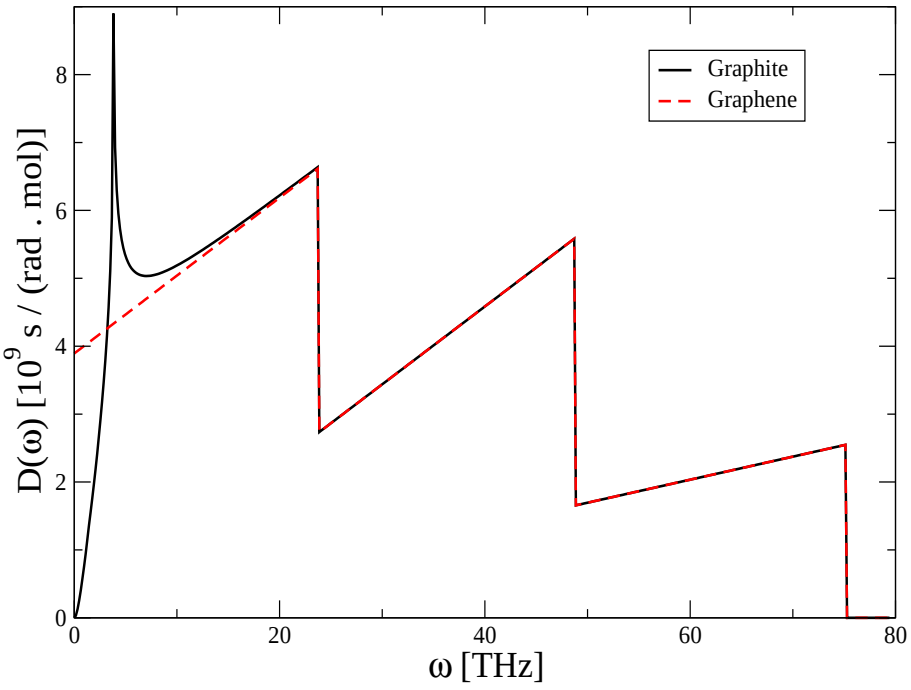

Figure 4.2: The total phonon density of states for graphene and graphite.

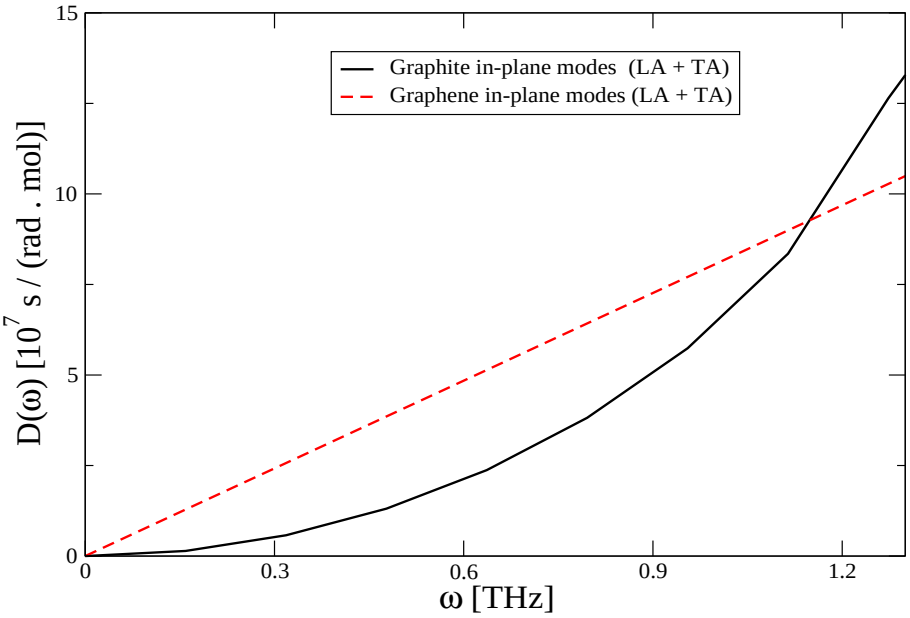

Figure 4.3: The total in-plane phonon density of states (LA+TA) for graphene and graphite.

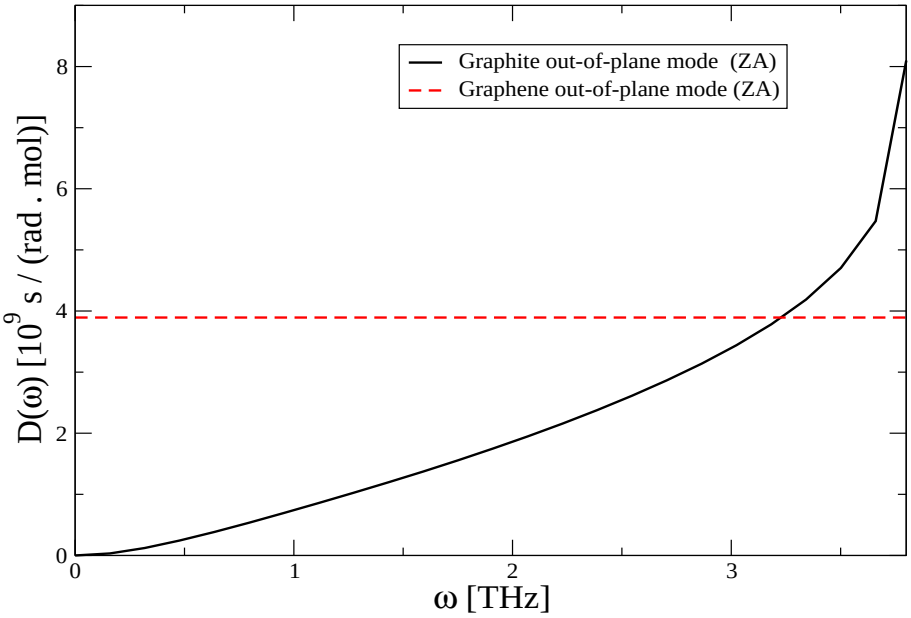

Figure 4.4: The out-of-plane phonon density of states (ZA) for graphene and graphite .

Figure 4.4 shows the PDOS of the ZA mode for graphene and graphite at very low frequencies. It is clear that in graphene or graphite the PDOS of ZA modes are two orders of magnitude higher than the PDOS of the in-plane modes. For the ZA modes in graphene, the PDOS keeps its constancy behaviour with respect to ω at this low range of frequencies. It can be deduced that the nonlinearity in the PDOS of the ZA modes in graphite is a consequence of the compressional motion that stems from the interacting graphene layers.

4.3 Phonon specific heat

The phonon specific heat measures how well the crystal can absorb or take up energy with increasing temperatures. There are two kinds of specific heat of a solid: specific heat at constant pressure $\mathrm{C_p}$ and specific heat at constant volume $\mathrm{C_v}$. In this section, we shall consider only the specific heat at constant volume due to its fundamental importance in the thermal properties of solids.

The specific heat has two contributions, one from the lattice vibrations i.e., phonon specific heat capacity and the other from the thermal motion of the electrons i.e., electron heat capacity. The contributions of electrons towards the specific heat of nonmetals can be neglected as it is much smaller than that of phonon specific heat capacity. Based on the classical theory, the average energy of each harmonic oscillator is $k_B T$. If there are N atoms in a solid, there will be $3N$ harmonic vibrations then the average energy can be given as $3Nk_B T$. The specific heat thus obtained is given as

$$\mathrm{C_v} = 3Nk_B \tag{4.24}$$

If N is substituted by N_A, then $\mathrm{C_v} = 24.94$ J/mol.K. It can be observed from this equation that the phonon specific heat capacity is independent of material prop-

erties and temperature. This is known as the *Dulong Petit law*. This holds well for higher temperatures, but for low temperatures $\mathrm{C_v}$ is no longer constant and decreases with temperature.

The specific heat is defined as

$$\mathrm{C_v} = \left(\frac{\partial E}{\partial T}\right)_{\mathrm{V}}, \tag{4.25}$$

where E is the thermal energy of the crystal with volume V at temperature T. Thus, one should calculate E in order to find $\mathrm{C_v}$.

4.4 Lattice thermal energy at finite temperatures

So far the mechanics of lattice vibrations has been considered in a completely classical way. To the extent that the normal modes are harmonic and independent, the transition to quantum mechanics is easily made by supposing that a lattice vibrational mode $\mathbf{q}p$ of frequency $\omega(\mathbf{q}p)$ will behave like a simple harmonic oscillator and will thus be restricted to energy values

$$E_{\mathbf{q}p} = \hbar\omega(\mathbf{q}p)(n_{\mathbf{q}p} + \frac{1}{2}) \tag{4.26}$$

Phonons are introduced as a convenient language to treat lattice vibrations and are dealt with as quasiparticles. Like photons, phonons are bosons and are not conserved; they can be created or removed when lattice vibrations interact with other fields (such as light) or particles (such as neutrons). Thus in Eq.(4.26), $n_{\mathbf{q}p}$ can take any value and can change with time. In most solids, the energy given to lattice vibrations is the dominant contribution to the heat capacity. We know that the coupling of atomic vibrations leads to a band of normal mode frequencies from zero up to maximum value. The number of phonons that are present in a given mode $\mathbf{q}p$ at temperature T can be determined by implementing the use

of partition function. The probability of occupancy of phonons $n_{\mathbf{q}p}$ of frequency $\omega(\mathbf{q}p)$ at temperature T can be written as

$$\mathcal{P}(n_{\mathbf{q}p}) = \mathcal{Z}\,\exp(-E_{\mathbf{q}p}/k_{\mathrm{B}}T), \tag{4.27}$$

where k_{B} is the Boltzmann's constant, $E_{\mathbf{q}p} = \hbar\omega(\mathbf{q}p)(n_{\mathbf{q}p} + \frac{1}{2})$, and $\mathcal{Z}$ is a normalisation factor (which is called the partition function) determined from

$$\sum_{n_{\mathbf{q}p}=0}^{\infty} \mathcal{P}(n_{\mathbf{q}p}) = \mathcal{Z} \sum_{n_{\mathbf{q}p}=0}^{\infty} \exp(-E_{\mathbf{q}s}/k_{\mathrm{B}}T) = 1, \tag{4.28}$$

So we have

$$\mathcal{Z} = \frac{1}{\sum_{n_{\mathbf{q}p}=0}^{\infty} \exp(-E_{\mathbf{q}p}/k_{\mathrm{B}}T)}. \tag{4.29}$$

So, the average energy can be written as

$$\begin{aligned} \bar{E}_{\mathbf{q}p} &= \sum_{n_{\mathbf{q}p}=0}^{\infty} E_{\mathbf{q}p}\mathcal{P}(n_{\mathbf{q}p}) = \frac{\sum_{n_{\mathbf{q}p}=0}^{\infty} E_{\mathbf{q}p}\exp(-E_{\mathbf{q}p}/k_{\mathrm{B}}T)}{\sum_{n_{\mathbf{q}p}=0}^{\infty} \exp(-E_{\mathbf{q}p}/k_{\mathrm{B}}T)} \\ &= \frac{\sum_{n_{\mathbf{q}p}=0}^{\infty} n_{\mathbf{q}p}\hbar\omega(\mathbf{q}p)\exp(-n_{\mathbf{q}p}\hbar\omega(\mathbf{q}p)/k_{\mathrm{B}}T)}{\sum_{n_{\mathbf{q}p}=0}^{\infty} \exp(-n_{\mathbf{q}p}\hbar\omega(\mathbf{q}p)/k_{\mathrm{B}}T)} + \frac{1}{2}\hbar\omega(\mathbf{q}p). \end{aligned} \tag{4.30}$$

By introducing the short hand variable $\mathcal{Y} = \exp(-\hbar\omega(\mathbf{q}p)/k_{\mathrm{B}}T)$ and using the following relations:

$$\begin{aligned} \sum_{n_{\mathbf{q}p}=0}^{\infty} \mathcal{Y}^{n_{\mathbf{q}p}} &= \frac{1}{1-\mathcal{Y}} \\ \sum_{n_{\mathbf{q}p}=0}^{\infty} n_{\mathbf{q}p}\mathcal{Y}^{n_{\mathbf{q}p}} &= \frac{\mathcal{Y}}{(1-\mathcal{Y})^2} \end{aligned} \tag{4.31}$$

the above equation can be rewritten as

$$\begin{aligned} \bar{E}_{\mathbf{q}p} &= \left(\frac{\sum_{n_{\mathbf{q}p}=0}^{\infty} n_{\mathbf{q}p}\mathcal{Y}^{n_{\mathbf{q}p}}}{\sum_{n_{\mathbf{q}p}=0}^{\infty} \mathcal{Y}^{n_{\mathbf{q}p}}} + \frac{1}{2}\right)\hbar\omega(\mathbf{q}p) \\ &= \left(\frac{\mathcal{Y}/(1-\mathcal{Y})^2}{1/(1-\mathcal{Y})} + \frac{1}{2}\right)\hbar\omega(\mathbf{q}p) \\ &= \left(\frac{\mathcal{Y}}{1-\mathcal{Y}} + \frac{1}{2}\right)\hbar\omega(\mathbf{q}p) \end{aligned}$$

$$= \left(\frac{\exp(-\hbar\omega(\mathbf{q}p)/k_{\mathrm{B}}T)}{1-\exp(-\hbar\omega(\mathbf{q}p)/k_{\mathrm{B}}T)} + \frac{1}{2}\right)\hbar\omega(\mathbf{q}p) \tag{4.32}$$

Since

$$\frac{\exp(-\hbar\omega(\mathbf{q}p)/k_{\mathrm{B}}T)}{1-\exp(-\hbar\omega(\mathbf{q}p)/k_{\mathrm{B}}T)} = \frac{1}{\exp(\hbar\omega(\mathbf{q}p)/k_{\mathrm{B}}T)-1} \tag{4.33}$$

then Eq.(4.32) can be expressed as

$$\bar{E}_{\mathbf{q}p} = \left(\frac{1}{\exp(\hbar\omega(\mathbf{q}p)/k_{\mathrm{B}}T)-1} + \frac{1}{2}\right)\hbar\omega(\mathbf{q}p) \tag{4.34}$$

The average energy per normal mode ($\mathbf{q}p$) can be defined as

$$\bar{E}_{\mathbf{q}p} = (\bar{n}_{\mathbf{q}p} + \frac{1}{2})\hbar\omega(\mathbf{q}p), \tag{4.35}$$

where $\bar{n}_{\mathbf{q}p}$ is the average value of $n_{\mathbf{q}p}$ at thermal equilibrium, at temperature T. Comparing Eq.(4.34) and Eq.(4.35), we get

$$\bar{n}_{\mathbf{q}p}(\omega, T) = \frac{1}{\exp(\frac{\hbar\omega(\mathbf{q}p)}{k_{\mathrm{B}}T})-1}. \tag{4.36}$$

This function is called *Bose-Einstein distribution function* which gives the probability of occupancy of phonons at thermal equilibrium. It can be seen that at absolute zero there are no phonons in the crystal. At low temperatures $\hbar\omega >> k_{\mathrm{B}}T$, there is an exponentially small probability for a phonon to be present, which means $\bar{n} \simeq \exp(-\frac{\hbar\omega(\mathbf{q}p)}{k_{\mathrm{B}}T})$. At higher temperatures, the number of phonons $\bar{n}_{\mathbf{q}p} \simeq k_{\mathrm{B}}T/\hbar\omega$ increases linearly with temperature.

The internal thermal energy of a vibrating crystal is

$$E = \sum_{\mathbf{q}}\sum_{p} \hbar\omega_p(\mathbf{q})\bar{n}_{\mathbf{q}p}(\omega, T), \tag{4.37}$$

where the summation is over all wave vectors $\mathbf{q}$ and all polarisations p. Equation (4.37) can be written as

$$E = \sum_{p} \int D_p(\omega)\hbar\omega_p(\mathbf{q})\bar{n}_{\mathbf{q}p}(\omega, T)\mathrm{d}\omega \tag{4.38}$$

where the summation over $\mathbf{q}$-values has been replaced by $\int \mathrm{d}\mathbf{q} = \int D(\omega)\mathrm{d}\omega$, the density of phonon states.

4.5 Specific heat of graphene and graphite

According to the definitions of the specific heat and energy expressed in Eq. (4.25) and Eq. (4.38), respectively, then the lattice specific heat at constant volume $\mathrm{C_v}$ is calculated by using the following equation

$$\mathrm{C_v} = \frac{\partial}{\partial T} \sum_p \int D_p(\omega) \hbar \omega_p(\mathbf{q}) \bar{n}_{\mathbf{q}p}(\omega, T) \mathrm{d}\omega, \tag{4.39}$$

where the evaluation of $\partial \bar{n}_{\mathbf{q}p}(\omega, T)/\partial T$ is provided in Appendix C. The specific heat can be finally written as

$$\mathrm{C_v} = k_B \sum_p \int_{\omega_{\mathrm{p,min}}}^{\omega_{\mathrm{p,max}}} \left(\frac{\hbar\omega}{k_B T} \right)^2 \bar{n}(\bar{n}+1) D_p(\omega) d\omega, \tag{4.40}$$

where $\omega_{\mathrm{p,min}}$ and $\omega_{\mathrm{p,max}}$ are the lower and upper cut-offs frequencies for each polarisation and $D_p(\omega)$ is the density of states as expressed in Eqs. (4.16 - 4.19).

By setting $x = (\hbar\omega)/(k_B T)$, the specific heat for the in-plane and out-of-plane modes for graphite can be written as

in-plane modes:

(i) $\omega \leq \omega_z$

$$\{\mathrm{C_v}\}_{\mathrm{LA}} = \frac{k_B^3 T^2}{\hbar^2} . \frac{A_m}{\pi^2 v_{\mathrm{LA}}^2} \int_0^{\frac{\hbar\omega_z}{k_B T}} x^3 \frac{e^x}{(e^x-1)^2} \sin^{-1}\left(\frac{x k_B T}{\hbar \omega_z} \right) \mathrm{d}x. \tag{4.41}$$

$$\{\mathrm{C_v}\}_{\mathrm{TA}} = \frac{k_B^3 T^2}{\hbar^2} . \frac{A_m}{\pi^2 v_{\mathrm{TA}}^2} \int_0^{\frac{\hbar\omega_z}{k_B T}} x^3 \frac{e^x}{(e^x-1)^2} \sin^{-1}\left(\frac{x k_B T}{\hbar \omega_z} \right) \mathrm{d}x. \tag{4.42}$$

(ii) $\omega \geq \omega_z$

$$\{\mathrm{C_v}\}_{\mathrm{LA}} = \frac{k_B^3 T^2}{\hbar^2} . \frac{A_m}{2\pi v_{\mathrm{LA}}^2} \int_{\frac{\hbar\omega_z}{k_B T}}^{\frac{\hbar}{k_B T}\sqrt{\frac{4\pi v_{\mathrm{LA}}^2 N_A}{A_m} + \frac{\omega_z^2}{2}}} x^3 \frac{e^x}{(e^x-1)^2} \mathrm{d}x. \tag{4.43}$$

$$\{\mathrm{C_v}\}_{\mathrm{TA}} = \frac{k_B^3 T^2}{\hbar^2} . \frac{A_m}{2\pi v_{\mathrm{TA}}^2} \int_{\frac{\hbar\omega_z}{k_B T}}^{\frac{\hbar}{k_B T}\sqrt{\frac{4\pi v_{\mathrm{TA}}^2 N_A}{A_m} + \frac{\omega_z^2}{2}}} x^3 \frac{e^x}{(e^x-1)^2} \mathrm{d}x. \tag{4.44}$$

out-of-plane modes:

(iii) $\omega \leq \omega_z'$

$$\{\mathrm{C_v}\}_{\mathrm{ZA}} = \frac{A_m k_B^3 T^2}{2\pi^2 \hbar^2 b \omega_z'} \int_0^{\frac{\hbar\omega_z'}{k_B T}} \left\{ x^3 \frac{e^x}{(e^x-1)^2} \right. \\ \left. \left[\int_0^{\sin^{-1}\{[1+(\zeta^2\hbar^2/4b^2k_B^2T^2x^2)]^{-1/2}\}} \left[1 - \left(\frac{x^2 k_B^2 T^2}{\hbar^2 \omega_z'^2} + \frac{\zeta^2}{4b^2\omega_z'^2} \right) \sin^2\phi \right]^{-1/2} \mathrm{d}\phi \right] \mathrm{d}x \right\} \tag{4.45}$$

(iv) $\omega \geq \omega_z'$

$$\{\mathrm{C_v}\}_{\mathrm{ZA}} \\ = \frac{A_m k_B^2 T}{2\pi^2 \hbar b} \int_{\frac{\hbar\omega_z'}{k_B T}}^{\frac{\hbar}{k_B T}\frac{4\hbar\pi b N_A}{A_m k_B T}} \left\{ x^2 \frac{e^x}{(e^x-1)^2} \right. \\ \left. \frac{1}{\sqrt{1+\frac{\hbar^2\zeta^2}{4b^2x^2k_B^2T^2}}} \left[\int_0^{\pi/2} \left[1 - \left(\frac{\hbar^2\omega_z'^2}{x^2 k_B^2 T^2} \right) \left(1 + \frac{\hbar^2\zeta^2}{4b^2x^2k_B^2T^2} \right)^{-1} \sin^2\phi \right]^{-1/2} \mathrm{d}\phi \right] \mathrm{d}x \right\} \tag{4.46}$$

For graphene:

$$\{\mathrm{C_v}\}_{\mathrm{LA}} = \frac{k_B^3 T^2}{\hbar^2} . \frac{A_m}{2\pi v_{\mathrm{LA}}^2} \int_0^{\frac{\hbar}{k_B T}\sqrt{\frac{4\pi v_{\mathrm{LA}}^2 N_A}{A_m}}} x^3 \frac{e^x}{(e^x-1)^2} \mathrm{d}x. \tag{4.47}$$

$$\{\mathrm{C_v}\}_{\mathrm{TA}} = \frac{k_B^3 T^2}{\hbar^2} . \frac{A_m}{2\pi v_{\mathrm{TA}}^2} \int_0^{\frac{\hbar}{k_B T}\sqrt{\frac{4\pi v_{\mathrm{TA}}^2 N_A}{A_m}}} x^3 \frac{e^x}{(e^x-1)^2} \mathrm{d}x. \tag{4.48}$$

$$\{\mathrm{C_v}\}_{\mathrm{ZA}} = \frac{A_m k_B^2 T}{2\pi^2 \hbar b} \int_0^{\frac{\hbar}{k_B T}\frac{4\hbar\pi b N_A}{A_m k_B T}} x^2 \frac{e^x}{(e^x-1)^2} \int_0^{\pi/2} \mathrm{d}\phi \, \mathrm{d}x \tag{4.49}$$

According to Debye model, the specific heat can be well determined by using a parameter called Debye temperature $\Theta = \hbar\omega_D/k_B$. It is related to the Debye frequency ω_D for each phonon polarization. The Debye temperatures for each mode in graphite are: $3608.85\ \mathrm{K},\ 2339.18\ \mathrm{K},$ and $1143.71\ \mathrm{K}$ for LA, TA, and ZA respectively [4]. It is clear that the Debye temperature of the ZA mode is about three times lower than the Debye temperature of LA mode and two times lower than that of TA mode. This is due to the softness of the ZA mode compared to the in-plane modes. This is why the Debye temperature can be a measure of the stiffness of solids.

The specific heat of graphene and graphite are presented in Fig. 4.5: they are almost similar at a wide range of temperature. At low temperatures, the variation of specific heat with temperature is quite different between graphene and graphite as shown in Fig. 4.6. For graphite, $\mathrm{C_v} \propto T^{2.5}$ whereas $\mathrm{C_v} \propto T^{1.1}$ for graphene in the temperature range $T \leq 40\ \mathrm{K}$. A considerable mount of experimental work has been carried out on the specific heat of graphite; the results of these experiments have shown significant differences due to several reasons: type, impurity, stacking faults, and/or the crystallite size of the specimen. In addition, graphite is an excellent adsorbent of other chemicals and this would introduce systematic errors in the specific heat determinations [5].

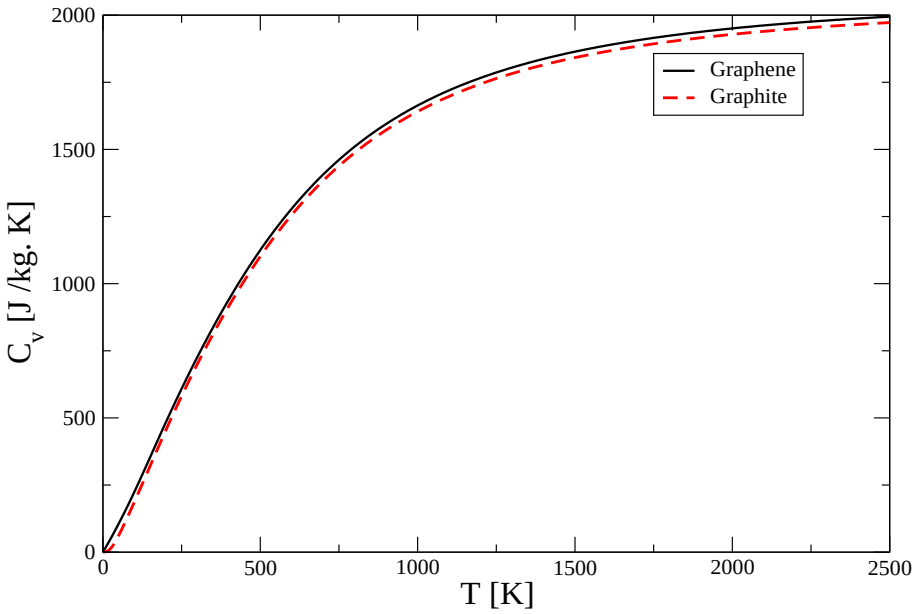

Figure 4.5: Specific heat for graphene and graphite .

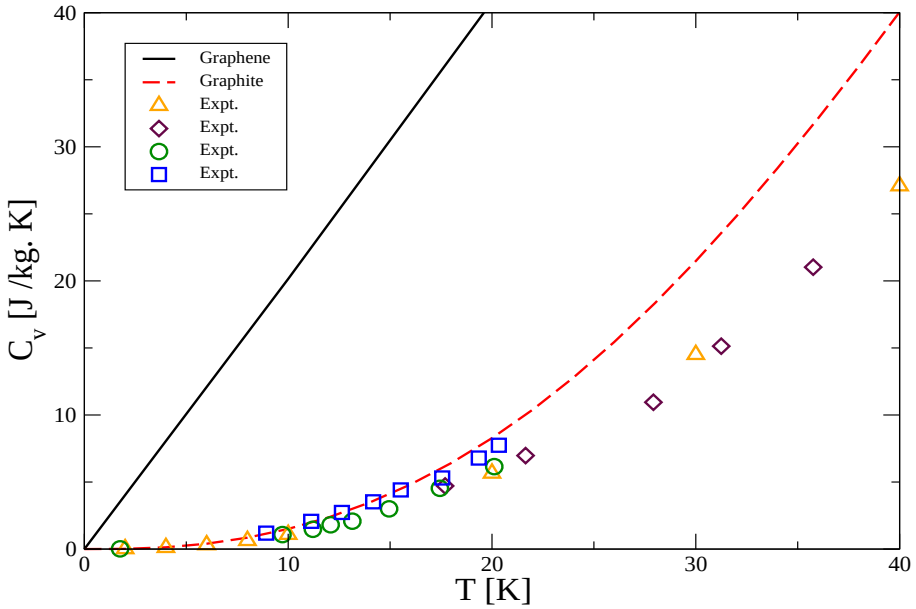

Figure 4.6: Specific heat for graphene (solid line) and graphite (dashed line) at low temperatures. The symbols represents the experimental measurements for graphite C_P: (up triangles) from Ref. [4]; (diamonds) from Ref. [6]; (circles) and (squares) from Ref [7].

Contributions from different acoustic branches to the specific heat of graphene and graphite are shown in Fig. 4.7, where we clearly notice that the contribution from the ZA branch is larger than either LA or TA branch at all temperatures up to 2500 K. The three polarisation do not begin to contribute equally, *i.e.* the Dulong-Petit limit is not reached, until above 2500 K. In graphene and graphite, LA and TA phonons contribute equally to the specific heat. The contribution of the ZA phonons in graphene is larger than those of graphite.

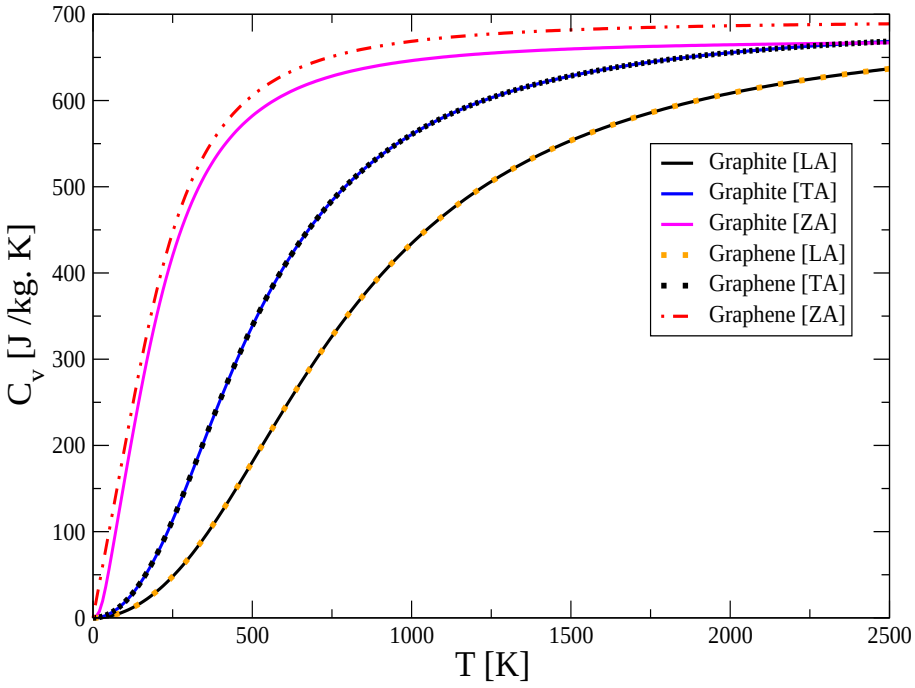

Figure 4.7: Graphene and graphite specific heat from separate acoustic modes.

For graphene, at 300 K, the contribution from the ZA phonons is approximately 3.1 and 7.2 times larger than the contribution from the TA and LA phonons, respectively. The specific heat curve for the ZA branch saturates before LA and TA modes due to its low Debye cut-off frequency. At low temperatures (up to 100 K) the specific heat is proportional to T^2 for the contributions from the LA and TA

branches, but proportional to T for the contribution from the ZA branch. This is due to the quadratic dispersion of the ZA phonons. The overall variation in this low temperature range is found to be $\mathrm{C_v} \propto T^{1.1}$.

The standard correlation between the dimensionality of the system and the phonon dispersion spectrum, the phonon density of states, and the specific heat is given in Table 4.2. The correlation obtained in this work is presented in Table 4.3

Table 4.2: Low-temperature behavior of the specific heat [8].

Dimensionality	Phonon dispersion	Phonon density of states	Specific heat
1D	$\omega \propto q^2$	$D(\omega) \propto 1/\sqrt{\omega}$	$\mathrm{C_v} \propto \sqrt{T}$
	$\omega \propto q$	$D(\omega) = \mathrm{const}$	$\mathrm{C_v} \propto T$
2D	$\omega \propto q^2$	$D(\omega) = \mathrm{const}$	$\mathrm{C_v} \propto T$
	$\omega \propto q$	$D(\omega) \propto \omega$	$\mathrm{C_v} \propto T^2$
3D	$\omega \propto q$	$D(\omega) \propto \omega^2$	$\mathrm{C_v} \propto T^3$

Table 4.3: Low-temperature behavior obtained in this work.

Dimensionality	Acoustic branch	Phonon dispersion	Phonon density of states	Specific heat
Graphite	LA, TA	$\omega \propto q$	$D(\omega) \propto \omega$	$\mathrm{C_v} \propto T^{2.6}$
	ZA	$\omega \propto q^{1.85}$	$D(\omega) \propto \omega^{1.44}$	$\mathrm{C_v} \propto T^2$
Graphene	LA, TA	$\omega \propto q$	$D(\omega) \propto \omega$	$\mathrm{C_v} \propto T^2$
	ZA	$\omega \propto q^2$	$D(\omega) = \mathrm{const}$	$\mathrm{C_v} \propto T$

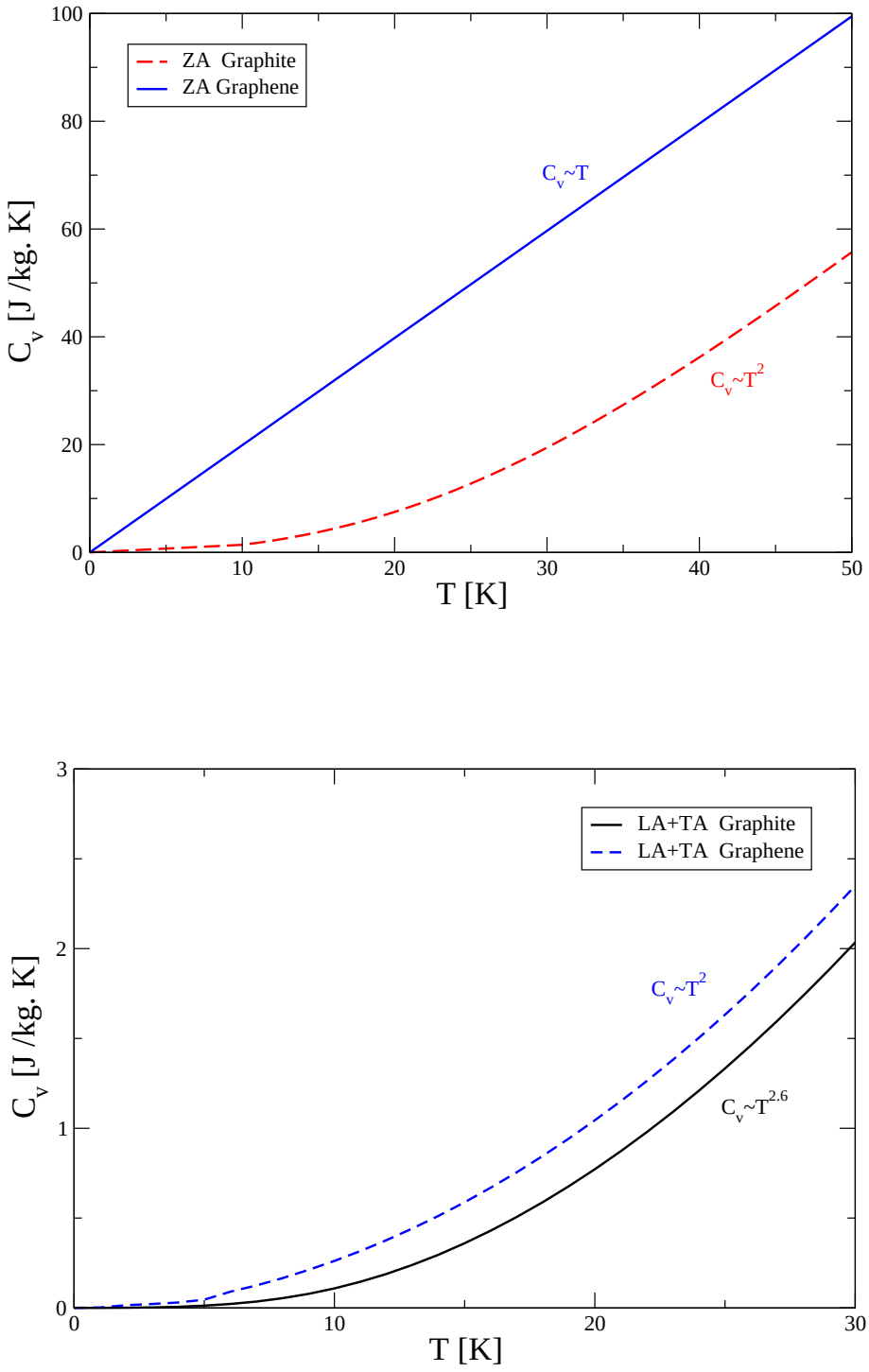

Figure 4.8: Specific heat behaviour at low temperatures for graphene and graphite: ZA modes (upper panel), and LA+TA modes (lower panel).

4.6 Summary

It is obvious in the light of the semicontinuum model that the phonon density of states differs from those deduced from the Debye model. Each mode is found to have its own velocity and is not an average for all branches or modes. There is a characteristic Debye cut-off frequency for each mode, and also there is a Debye-like cut-off frequency for very low shearing and compressional modes. Graphene and graphite phonon density of states are similar for the in-plane modes. Only the out-of-plane modes distinguish graphene from graphite by the occurrence of a sharp peak in the phonon density of states in graphite whereas the phonon density of states in graphene is constant. The distinction between the phonon density of states of graphene and graphite is clearly observed at low frequencies. The phonon density of states of the in-plane modes at low frequencies shows a linear behaviour in graphene and a nonlinear one in graphite. The phonon density of states of the out-of-plane modes is frequency independent in graphene, but it shows a non linear dependence on frequencies in graphite. At low frequencies, the phonon density of states of the out-of-plane modes are two orders of magnitude higher than the phonon density of states of the in-plane modes in graphene or graphite. The specific heat of graphene and graphite are almost identical except at very low temperatures.

Bibliography

[1] G. P. Srivastava, *The Physics of Phonons* (Adam Hilger, Bristol, 1990).

[2] C. Kittel, *Introduction to Solid State Physics* 7^{th} Edan (John Wiley & Sons, New York, 1996).

[3] K. Komatsu, J. Phys. Soc. Japan **10**, 346 (1955).

[4] T. Nihira and T. Iwata, Phys. Rev. B **68**, 134305 (2003).

[5] P. H. Keesom and N. Pearlman, Phys. Rev. **99**, 1119 (1955).

[6] W. Desorbo, J. Am. Chem. Soc. **77**, 4713 (1955).

[7] W. Desorbo and G. E. Nichols, J. Phys. Chem. Solids **6**, 352 (1958).

[8] J. Zimmerman, P. Paving, and G. Guilbert, Phys. Rev. B. **78**, 045410 (2008).

Chapter 5

Theory of Phonon Scattering and Heat Transport in Graphene

5.1 Introduction

During propagation of phonons through a medium they engage in anharmonic interactions with one another (phonon-phonon scattering), and with electrons, impurities, and geometric boundaries. While some forms of scattering do not necessarily restore thermodynamic equilibrium, phonon-phonon scattering helps restore thermodynamic equilibrium. If the characteristic geometrical size of the medium is much larger than the mean free path of the phonons, the number of scattering events is large and the thermodynamic equilibrium is restored. Under these conditions, a temperature gradient is established within the medium and the overall heat transport process is diffusion-like regime. This regime can be described accurately using the Fourier's law of heat conduction.

The Boltzmann Transport Equation (BTE) is the most suitable candidate for describing phonon transport or phonon conductivity in non-metallic crystalline solids. It is an equation which specifies the change of the distribution function with time

when a non-equilibrium state occurs by allowing thermal current to flow. The BTE is a statement of conservation of the phonon distribution function, in the limit when the perturbation vanishes, the non-equilibrium distribution function must approach the appropriate equilibrium distribution. This BTE employs the particle like nature of phonons to model heat transfer at small scales. A calculation of phonon conductivity calls for solving BTE. However, the BTE is extremely difficult to solve analytically or even numerically using deterministic approaches, simply because the number of independent variables is too large. For the sake of simplification, analytical thermal conductivity models used have been based on the single mode relaxation time (smrt) approximation in the BTE.

Among these models is Callaway's model [1] which is a successful and widely accepted model of lattice thermal conductivity. Holland [2] extended the work of Callaway by taking into account different considerations which will be addressed later in this chapter. Callaway provided the most widely used formulation for thermal conductivity that enables using adjustable parameters for data fitting for a variety of solids. In this chapter, different types of phonon scattering mechanisms dealt with in this project will be discussed. Also, phonon relaxation times for each type of phonon scattering are introduced. We apply Callaway's theory in its full form to evaluate the phonon conductivity in graphene. Our calculations employ the analytical expressions for the phonon dispersion relations and the vibrational density of states based on the work by Nihira and Iwata [3] within Debye's isotropic continuum model.

5.1.1 Phonon scatterings and relaxation times

Phonon scattering processes can be induced by: (i) extrinsic mechanisms (geometrical size of the crystals, isotopic defects, structural disorders, etc.) or by (ii)

intrinsic ones (anharmonic phonon-phonon scattering). The important time parameters that govern the microscopic heat transport are : thermalisation time (the time needed for the electrons and phonons to reach equilibrium); diffusion time (the time taken by the heat to travel through the sample); relaxation time (the time associated with the velocity at which a thermal disturbance propagates through the sample); heating time (the time during which an external source heats the sample). In this work, only the phonon relaxation times will be considered.

Different phonon scattering mechanisms may dominate at different temperatures. The major challenge in the calculation of thermal conductivity is determining the relaxation times τ from various types of phonon-scattering processes. The phonon relaxation time can be used to describe the recovery of the perturbed phonons distribution from the influence of the temperature gradient. It is a collective parameter governed by various scattering processes. These scattering processes are assumed to be independent of one another and thus follow Matthiessen's rule (see Ref. [4]). This rule proposes that the resistivity of a system with distinct scattering mechanisms is the sum of the individual resistivities. As resistivity is governed by the phonon relaxation rate τ^{-1}, we can express

$$\tau^{-1} = \sum_i \tau_i^{-1}, \tag{5.1}$$

where τ_i^{-1} is the contribution from the i^{th} scattering process. We will address the widely considered phonon scattering mechanisms: boundary scattering, imperfection scattering, and three-phonon scattering (Umklapp (U) and Normal (N) scattering). In this work, the phonon scattering processes are represented by frequency and temperature dependent relaxation times functions.

5.1.2 Boundary scattering

It is important to consider the effect of the geometrical shape and size on the magnitude of the heat current. At low temperatures, phonons acquire long wavelengths comparable to crystal dimensions which prevent them from being scattered within the crystal and the only scattering (dominant scattering) which restricts the flow of heat is that taking place at the external boundaries of the crystal. This is called the boundary scattering process. The dependence of boundary scattering relaxation time on sample size has been discussed originally by Casimir [5] followed by Berman *et al.* [6, 7], Carruthers [8], and Ziman [9]. A simple conclusion from theses studies is that the phonon relaxation rate τ_{bs}^{-1} due to boundary scattering is expressed as

$$\tau_{bs}^{-1} = \frac{v_p}{L}, \tag{5.2}$$

where v_p is the speed of phonons in polarisation branch p, and L represents an effective length determined from the geometry of the sample and is assumed to be the same for all phonon modes.

5.1.3 Imperfection scatterings

As temperature increases and approaches the range where thermal conductivity takes its maximum value, the dominant phonon wavelength decreases and becomes comparable to the size of crystal defects. In this temperature range, defects and isotopes strongly control the mean-free path of phonons and thus the thermal conductivity of the material. Fluctuations in mass distribution in a crystal account for thermal resistance, this was first pointed out by Pomeranchuk in 1942 [10]. Also, he commented that the presence of isotopes in a crystal will disrupt the periodicity of the crystal and thus cause thermal resistance. Gener-

ally, the phonon scattering rate $\tau_{\rm pd}^{-1}$ on point defects affects the phonon transport through mass-difference, and is given as [11, 12]

$$\tau_{\rm pd}^{-1} \propto \Omega \left(\frac{\omega^{\iota}}{v_p^{\xi}}\right) \Gamma_{\rm md}, \tag{5.3}$$

where Ω is the volume per atom in the crystal, and $\iota = 3(4)$ and $\xi = 2(3)$ for a 2D(3D) system, respectively, and $\Gamma_{\rm md}$ is the measure of the strength of the mass-difference scattering or the mass-fluctuation phonon-scattering parameter, given as

$$\Gamma_{\rm md} = \sum_i f_i \left(1 - \frac{M_i}{\bar{M}}\right)^2 = \sum_i f_i \left(\frac{\Delta M_i}{\bar{M}}\right)^2, \tag{5.4}$$

where f_i is the fractional concentration of the impurity atoms of mass M_i, and $\bar{M} = \sum_i f_i M_i$ is the average atomic mass.

In the present two-dimensional model, we adopted the expression that has been used by Klemens and Pedraza [12] in their calculations for the thermal conductivity of the two-dimensional graphite basal planes. The phonon relaxation rate for each polarization p from such scatterings is expressed as

$$\tau_{\rm pd}^{-1} = \frac{2\pi c_d\, \omega^3}{\omega_{p,\max}^2} \left(\frac{\Delta M}{M}\right)^2, \tag{5.5}$$

where c_d is the point defect concentration and $\Delta M/M$ is the fractional atomic mass change. Using a simple scheme, based on the application of the virial theorem and shared links, Ratsifaritana and Klemens [13] argued that the presence of a vacancy in a three-dimensional crystal would lead to $\Delta M/M = 3$. In this work, we used this value which has been also used by Klemens and Pedraza. Naturally-occurring carbon materials consist of two stable isotopes ^{12}C and ^{13}C with abundancy of $\sim 99\%$ and $\sim 1\%$ respectively [14, 15]. The phonon relaxation rate due

to isotopic scattering can be expressed as

$$\tau_I^{-1} = \frac{2\pi\omega^3}{\omega_{p,\max}^2}\left[f_1\left(\frac{\Delta M_1}{\bar{M}}\right)^2 + f_2\left(\frac{\Delta M_2}{\bar{M}}\right)^2\right], \tag{5.6}$$

where τ_I^{-1} is the isotope scattering relaxation time, M_1 and M_2 are the atomic masses for ^{13}C and ^{12}C respectively, f_1 and f_2 are the fractions of unit cells having masses M_1 and M_2, respectively.

5.1.4 Three-phonon scattering (Umklapp and Normal processes)

The interactions of phonons among themselves take place even in a perfect crystal and these interactions give rise to thermal resistance. The occurrence of cubic terms in the Hamiltonian, which describes the elastic potential energy of a displaced ion in the crystal, gives rise to three-phonon interactions while the quartic terms gives rise to four-phonon interactions. The strength of the latter processes are two to three orders of magnitude weaker than the former one [16]. Thus, we will be considering only three-phonon scattering processes in this work.

A three-phonon process or scattering can be classified into two classes and there are two selection rules governing the allowed three-phonon scattering. The first selection rule is based on the momentum conservation principle in which wave vectors of the interacting phonons must satisfy [4] the equations.

$$\begin{aligned} \hbar\mathbf{q} + \hbar\mathbf{q}' &= \hbar\mathbf{q}'' + \hbar\mathbf{G} \quad (\text{class } 1) \\ \hbar\mathbf{q} + \hbar\mathbf{G} &= \hbar\mathbf{q}' + \hbar\mathbf{q}'' \quad (\text{class } 2), \end{aligned} \tag{5.7}$$

where $\mathbf{G}$ is a reciprocal lattice vector. The second selection rule arises from the conservation law of energy is

$$\hbar\omega(\mathbf{q}p) + \hbar\omega(\mathbf{q}'p') = \hbar\omega(\mathbf{q}''p'') \quad (\text{class } 1)$$
$$\hbar\omega(\mathbf{q}p) = \hbar\omega(\mathbf{q}'p') + \hbar\omega(\mathbf{q}''p'') \quad (\text{class } 2). \tag{5.8}$$

In class 1, a phonon ($\mathbf{q}p$) interacts with another phonon ($\mathbf{q}'p'$), annihilate each other, and a third phonon ($\mathbf{q}''p''$) is created. In class 2, annihilation of phonon ($\mathbf{q}p$) results in producing two other phonons ($\mathbf{q}'p'$ and $\mathbf{q}''p''$). During both processes, the resultant wave vector can be either inside the Brillouin zone (N-process), or it can be outside the Brillouin zone (U-process), then with the help of an appropriate lattice reciprocal vector $\mathbf{G}$ it can be flipped back into the Brillouin zone. N-processes are momentum conserving processes while U-processes are not. Once a thermal gradient is established in a crystal, the heat would continue to flow even in the absence of a thermal gradient, if only normal processes were available to scatter phonons. This condition means zero thermal resistance or infinite thermal conductivity. On the other hand, Umklapp processes will lead to a total change in the phonon wave vector and thus causing thermal resistance. The universal behaviour of thermal conductivity of almost all non-metallic crystals as a function of temperature can be seen in Fig 5.1. It summarizes various phonon scattering mechanisms and their regime of dominance. Also, it can be noticed that the influence of Normal phonon-phonon scattering process is dominant over a wider range of temperatures.

While the influence of all phonon scattering processes on thermal conductivity at different temperatures has been well analysed, the three-phonon N-processes have been ignored in most of the calculations. The reason for ignoring normal processes is the premise that these processes conserve phonon momentum and hence do not contribute to thermal resistance. While this is partially true, N-processes can participate in redistributing phonons which in turn undergo U-

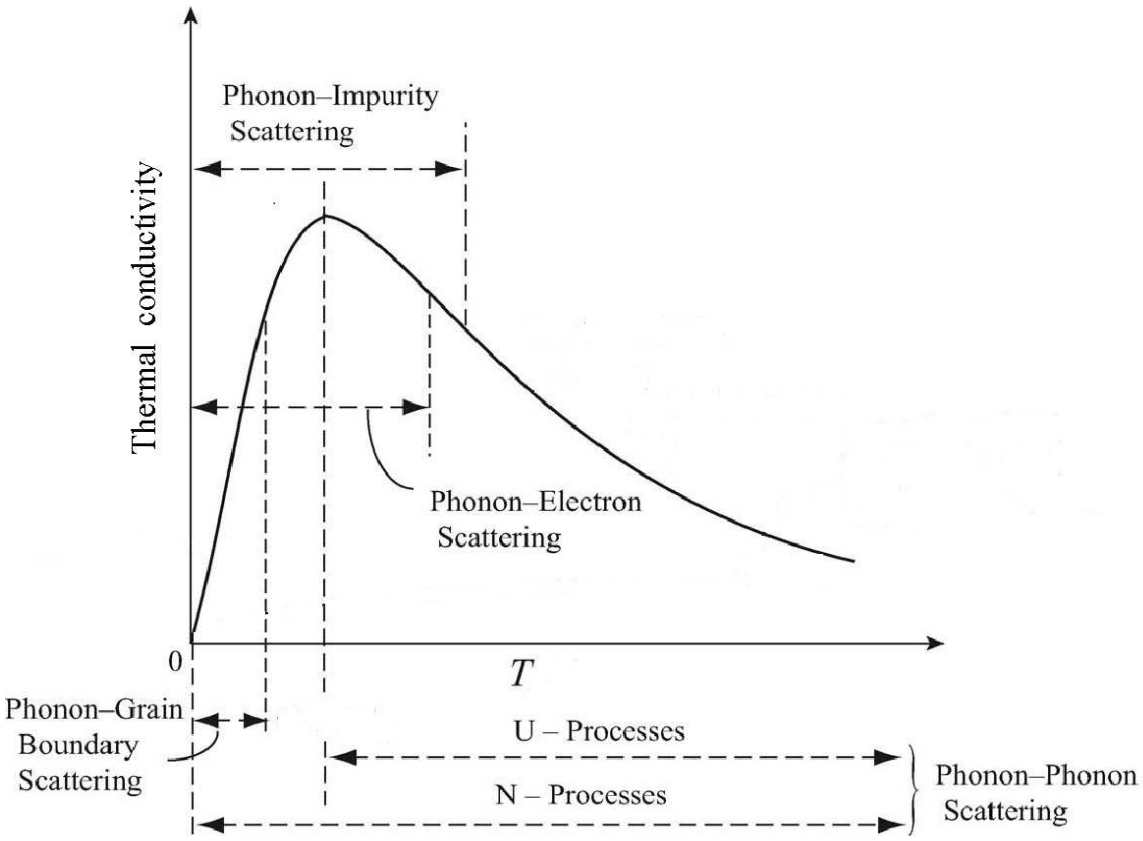

Figure 5.1: Phonon scattering mechanisms and their regimes of dominance in variation of thermal conductivity with respect to temperature. Reproduced from Ref. [17].

processes thereby contributing indirectly to the overall thermal conductivity. For 3D materials, neglecting N-processes still provides remarkable agreement with the experiments, this can be attributed to the high number of phonons that participate in U-processes are compared to that of N-processes phonons. But, in case of low dimensional (2D) systems such as graphene, the accumulation of phonons in large wave vector is very small and neglecting N-processes will result in an incorrect evaluation of thermal conductivity as will be seen in section 5.3.

Expressions for anharmonic relaxation times of phonons can be derived by applying first-order time-dependent perturbation theory [4, 18]. Such an attempt

requires knowledge of cubic anharmonic term in the crystal potential and a careful consideration of the allowed combination of phonon modes for Normal (N) and Umklapp (U) processes within the momentum and energy selection rules. Such a task is usually very demanding, and becomes even more so for graphene which is characterised by the nonlinear dispersion behaviour of the ZA branch. We will review some widely used mathematical expressions for the anharmonic phonon-phonon scattering rates.

Herring [19], in 1954, established that the relaxation time of longitudinal phonons involved in three phonon scattering processes depends on wave vector, temperature, and crystal symmetry (s). This symmetry can be represented by an integer and can be written as

$$\tau_{anh}^{-1}(q) = q^s T^{5-s}. \tag{5.9}$$

Since then, the frequency and temperature dependencies of three-phonon relaxation times have been discussed by many authors (for example, Klemens 1958 [20], Callaway 1959 [1], Ziman 1960 [18], Holland 1963 [2], Slack and Galginaitis 1964 [21], Guthrie 1966 [22]). Almost every author has taken the form of the relaxation rate as $\tau_{anh}^{-1} = B\omega^n T^m$. The parameter B assigned either temperature dependent or independent values, the exponent n for different polarisation modes is adjusted in the light of the experiments, and m is approximated at low and high temperatures.

Callaway was the first who pointed out that the momentum-conserving nature of Normal processes is an essential part of lattice thermal conduction process and its contribution should be added to the Umklapp processes. Thus, the anharmonic

scattering rate is considered to be a contribution of both as follows

$$\tau_{\text{anh}}^{-1} = \tau_N^{-1} + \tau_U^{-1}, \tag{5.10}$$

where τ_N^{-1} and τ_U^{-1} are the relaxation rates for Normal and Umklapp phonon-phonon scattering, respectively. These relaxation rates are expressed mathematically as

$$\tau_N^{-1} = B_N \omega^2 T^3, \tag{5.11}$$

$$\tau_U^{-1} = B'_U \omega^2 T^3, \tag{5.12}$$

where B_N and B'_U are parameters for the three-phonon Normal and Umklapp processes, respectively. Only B'_U contains the exponential temperature factor $\exp(-\Theta/\alpha T)$, where Θ is the Debye temperature and α is a constant characteristic of the vibrational spectrum of the material. Consequently, the contribution of the Umklapp processes to the thermal resistivity decreases very rapidly with decreasing temperature. In addition, no distinction is made between longitudinal and transverse polarisations in Callaway's expression for anharmonic scattering.

Holland [2] extended the Callaway model by considering the separate contributions of longitudinal acoustic and transverse acoustic phonons, including some dispersion, and using different expressions for the anharmonic relaxation times. These expressions have been further refined by several authors [23, 24, 25, 26, 27, 28] to evaluate the lattice thermal conductivity of several samples by including further detail on the phonon dispersion and relaxation times. However, this led to more fitted parameters and one could argue that the better correlations against the experimental data are due to this increase in the number of fitting parameters rather than due to an improvement of Callaway's model. Table 5.1 summarised

some of the mathematical expressions used by different authors to describe the anharmonic three-phonon scattering.

In this work we assume that the Normal and Umklapp processes have the same frequency dependence and we employ the low-temperature form of anharmonic relaxation rate using a simple parametrized expression [1]

$$\begin{aligned} \tau_{\rm anh}^{-1} &= [B_N + B'_U]\omega^2 T^3 \\ &= [B_N + B_U \exp(-\bar{\Theta}/\alpha T)]\omega^2 T^3, \end{aligned} \tag{5.13}$$

where B_U is a parameter for three-phonon Umklapp processes, $\bar{\Theta}$ is the the average Debye temperature for all acoustic branches, and α is a constant. The presence of the exponential factor in the expression for τ_U^{-1} is consistent with the well-founded assumption that Umklapp processes get frozen out at much lower temperatures. Following discussions in previous works (see, e.g., Refs. [29, 30, 31]), we set $\alpha = 3$ as a good choice. We expect the temperature dependence in the relaxation-rate expression in Eq. (5.13) to be valid in the range $T \leq \bar{\Theta} \simeq 1000$ K for graphene. We also remark that the anharmonic relaxation rate in the form $\omega^2 T$ used by Klemens and Pedraza [12], and subsequently by Nika *et al.* [32] is more suitable at higher temperatures (i.e., above $\bar{\Theta}$).

In this work, for pristine undoped graphene, the total phonon relaxation rate is a sum of the contributions from the scattering of phonons from the finite size of sample, point defects, and anharmonicity as

$$\begin{aligned} \tau^{-1} &= \tau_{\rm bs}^{-1} + \tau_{\rm pd}^{-1} + \tau_{\rm anh}^{-1} \\ &= \frac{v_p}{L} + \frac{2\pi c_d\, \omega^3}{\omega_{p,\max}^2} \left(\frac{\Delta M}{M}\right)^2 + [B_N + B_U \exp(-\bar{\Theta}/\alpha T)]\omega^2 T^3. \end{aligned} \tag{5.14}$$

In Eq.(5.14) , the single-mode relaxation time is known and one can evaluate the thermal conductivity within the framework of the BTE.

Table 5.1: Different models of three-phonon anharmonic scattering.

Three phonon-phonon scattering	Scattering rate
Normal processes	
Herring [19]	$\tau_{\mathrm{LA},N}^{-1} = B_{\mathrm{LA}}\omega^2 T^3$, low T
	$\tau_{\mathrm{TA},N}^{-1} = B_{\mathrm{TA}}\omega T^4$, low T
	$\tau_{\mathrm{LA},N}^{-1} = B'_{\mathrm{LA}}\omega^2 T$, high T
	$\tau_{\mathrm{TA},N}^{-1} = B'_{\mathrm{TA}}\omega T$, high T
Callaway [1]	$\tau_N^{-1} = B_N\omega^2 T^3$
Umklapp processes	
Klemens [33]	$\tau_U^{-1} = B_U\omega^2 T^3 \exp(-\frac{\theta}{\alpha T})$, low T
Klemens [20]	$\tau_U^{-1} = B_U\omega T^3 \exp(-\frac{\theta}{\alpha T})$, low T
	$\tau_U^{-1} = B'_U\omega^2 T$,high T
Callaway [1]	$\tau_U^{-1} = B_U\omega^2 T^3$
Holland [2]	$\tau_{\mathrm{TA},U}^{-1} = \frac{B_{\mathrm{TA},U}\omega^2}{\sinh(x)}$, $\omega_1 \leq \omega \leq \omega_2$, $x = \hbar\omega/k_B T$
	$= 0$, $\omega < \omega_1$
Asen-Palmer *et al.* [28]	$\tau_{\mathrm{TA},U}^{-1} = B'_{\mathrm{TA},U}\omega^2 T \exp(-\frac{C_T}{T})$
	$\tau_{\mathrm{LA},U}^{-1} = B'_{\mathrm{LA},U}\omega^2 T \exp(-\frac{C_L}{T})$

5.2 Lattice thermal conductivity

The thermal conductivity, K, is a measure of a material's ability to transfer thermal energy by conduction. It is introduced through Fourier's law which states that the magnitude of the induced heat flux $\boldsymbol{Q}$ will be proportional to the temperature gradient $\boldsymbol{\nabla} T$, and defines thermal conductivity as the property of the solid that relates the two as follows

$$\boldsymbol{Q} = -K\boldsymbol{\nabla} T, \tag{5.15}$$

In this expression, K is constant for extremely small temperature variations. However, over a wide temperature range, it becomes a function of temperature and crystal orientations in anisotropic materials. In 1929, Peierls [34] used the single-mode-relaxation-time (*smrt*) approach for thermal conductivity analysis, attributing the conductivity to Umklapp processes. Ziman [18], in 1960, redeveloped the theory of thermal conductivity based on various variational models, and obtained the well known expression for the thermal conductivity

$$K(T) = \frac{1}{3}\mathrm{C_v}(T)\bar{v}_g\Lambda(T), \tag{5.16}$$

where $\mathrm{C_v}$ is the specific heat, $\bar{v}_g$ is the phonon average velocity, and $\Lambda(T)$ is the phonon mean free path.

Within the Debye spectrum for phonons, Callaway pointed out that an additional or correction term to the (*smrt*) thermal conductivity is required to determine an effective relaxation time of phonons. This term emerged due to phonon-phonon Normal scattering processes. Thus, the resulting conductivity expression includes an extra term over and above the Debye term, and is known as the N-drift term. It has been shown [35] that the N-drift contribution can be quite large for pure crystals. It is, thus, expected that this contribution will be quite large for

a pure graphene sheet.

5.2.1 The phonon Boltzmann equation

The phonon Boltzmann equation is 7-D in general: 3-D spatial ($\mathbf{r}$), 3-D momentum ($\mathbf{q}$), and time (t) dependence. Let the distribution function $n_{\mathbf{q},p}(\mathbf{r},t)$ representing the probability of a phonon ($\mathbf{q},p$) occupying position ($\mathbf{r}$) with momentum ($\mathbf{q}$) and polarisation (p) at time t. Phonons change their states by two mechanisms: Diffusion and scattering. *diffusion* is a spatial distribution of temperature ($T = T(\mathbf{r})$) involved when a temperature gradient $\boldsymbol{\nabla} T$ is applied. This causes $n_{\mathbf{q},p}(\mathbf{r},t)$ to diffuse or, in other words, the number of phonons depends on the temperature gradient and tends to flow down the gradient and thus, varies from one point to another at the rate

$$\left.\frac{\partial n_{\mathbf{q}p}}{\partial t}\right|_{diff} = -\mathbf{v}_p(\mathbf{q}) \cdot \boldsymbol{\nabla} T \frac{\partial n_{\mathbf{q}p}}{\partial T}, \tag{5.17}$$

where $\mathbf{v}_p$ is the phonon group velocity in polarisation p. The second mechanism is *scattering*, where phonons collide with each other and with imperfections. The rate of change $\frac{\partial n_{\mathbf{q}p}}{\partial t}|_{scatt}$ has contributions from various scattering processes. In the case of steady state flow of heat through the solid, the total rate of $n_{\mathbf{q},p}$ must vanish as the scattering processes tend to restore the distribution of phonons to its equilibrium state at a rate proportional to the departure of the distribution from equilibrium. Hence

$$-\mathbf{v}_p(\mathbf{q}) \cdot \boldsymbol{\nabla} T \frac{\partial n_{\mathbf{q}p}}{\partial T} + \left.\frac{\partial n_{\mathbf{q}p}}{\partial t}\right|_{scatt} = 0. \tag{5.18}$$

This is a general form of the Boltzmann transport equation for phonons. As mentioned previously in this chapter, the solution of this equation is required in the

calculation of phonon conductivity. The solution is very complicated because it requires the knowledge of the distribution function $n_{\mathbf{q}'p'}$ for all possible phonon states together with the probability of their transitions rates from $\mathbf{q}'p'$ to $\mathbf{q}p$. Fortunately, an approximation (linearisation) of this equation is possible based on the single-mode relaxation-time (*smrt*) approach.

5.2.2 Single-mode-relaxation-time (*smrt*) approximation

The *smrt* method offers a very simple picture of phonon interaction processes. This approach is based on the assumptions that in calculating the relaxation rate (τ_{qp}^{-1}) for phonons in the mode $\mathbf{q}p$, which have been driven out of their equilibrium distribution, all other phonons in all other modes are assumed to be in thermal equilibrium. In equilibrium, the phonon distribution function does not change with time (*i. e.* $\frac{\partial \bar{n}_{\mathbf{q}p}}{\partial t} = 0$). Therefor, $n_{\mathbf{q}p}$ in the second term of Eq. (5.18) can be replaced with the linear term $[(\bar{n}_{\mathbf{q}p} - n_{\mathbf{q}p})/\tau_{\mathbf{q}p}]$ in a Taylor expansion of $n_{\mathbf{q}p}$ about the equilibrium distribution $\bar{n}_{\mathbf{q}p}$. The linearised Boltzmann equation can be then expressed as

$$-\mathbf{v}_p(\mathbf{q}) \cdot \boldsymbol{\nabla} T \frac{\partial n_{\mathbf{q}p}}{\partial T} = \frac{n_{\mathbf{q}p} - \bar{n}_{\mathbf{q}p}}{\tau_{\mathbf{q}p}}, \tag{5.19}$$

where $\tau_{\mathbf{q}p}$ is the phonon scattering relaxation time. Equation (5.19) says that the scattering processes tend to retrieve a phonon distribution $n_{\mathbf{q}p}$ to its equilibrium state $\bar{n}_{\mathbf{q}p}$ at a rate proportional to the departure of the distribution from equilibrium.

The next step now is to calculate the total heat flux $\mathbf{Q}$ carried by all phonon modes which can be written as

$$\mathbf{Q} = \frac{1}{V_m} \sum_{\mathbf{q}p} \hbar\omega(\mathbf{q}p) n_{\mathbf{q}p} \mathbf{v}_p(\mathbf{q}), \tag{5.20}$$

where V_m is the molar volume of the solid.

Expressing

$$\begin{aligned} n_{\mathbf{q}p} &= [\exp(\hbar\omega(\mathbf{q}p)/k_{\mathrm{B}}T - \psi_{\mathbf{q}p}) - 1]^{-1} \\ &\simeq \bar{n}_{\mathbf{q}p} - \psi_{\mathbf{q}p}\frac{\partial \bar{n}_{\mathbf{q}p}}{\partial(\hbar\omega(\mathbf{q}p)/k_B T)} \\ &= \bar{n}_{\mathbf{q}p} + \psi_{\mathbf{q}p}\bar{n}_{\mathbf{q}p}(\bar{n}_{\mathbf{q}p} + 1), \end{aligned} \tag{5.21}$$

where $\psi_{\mathbf{q}p}$ is the deviation of the distribution function $n_{\mathbf{q}p}$ from equilibrium $\bar{n}_{\mathbf{q}p}$. From Eq. (5.20), the contribution to the heat current can be expressed as

$$\mathbf{Q} = \frac{1}{V_m}\sum_{\mathbf{q}p}\hbar\omega(\mathbf{q}p)\psi_{\mathbf{q}p}\bar{n}_{\mathbf{q}p}(\bar{n}_{\mathbf{q}p} + 1)\mathbf{v}_p(\mathbf{q}). \tag{5.22}$$

Recalling Eq.(5.15), it can be shown that

$$K = -\frac{\mathbf{Q}\cdot\boldsymbol{\nabla}T}{|\boldsymbol{\nabla}T|^2}. \tag{5.23}$$

Substituting Eq.(5.22) into Eq.(5.23) we get

$$K = -\frac{1}{V_m|\boldsymbol{\nabla}T|^2}\sum_{\mathbf{q}p}\hbar\omega(\mathbf{q}p)\psi_{\mathbf{q}p}\bar{n}_{\mathbf{q}p}(\bar{n}_{\mathbf{q}p} + 1)\mathbf{v}(\mathbf{q}p)\cdot\boldsymbol{\nabla}T. \tag{5.24}$$

We need to find an alternative expression for $\psi_{\mathbf{q}p}$ other than that in Eq.(5.21), this expression can be easily deduced from Eq.(5.19), Eq.(5.21), and Eq.(C.4)(see Appendix C). It can be shown that

$$\psi_{\mathbf{q}p} = -\mathbf{v}_p(\mathbf{q})\cdot\boldsymbol{\nabla}T\tau_{\mathbf{q}p}\frac{\hbar\omega(\mathbf{q}p)}{k_{\mathrm{B}}T^2}. \tag{5.25}$$

Substituting Eq. (5.25) into Eq. (5.24) we find

$$K = \frac{1}{V_m k_{\mathrm{B}}T^2}\sum_{\mathbf{q}p}\frac{(\mathbf{v}_p(\mathbf{q})\cdot\boldsymbol{\nabla}T)^2}{|\nabla T|^2}\hbar^2\omega^2(\mathbf{q}p)\bar{n}_{\mathbf{q}p}(\bar{n}_{\mathbf{q}p} + 1)\tau_{\mathbf{q}p}$$

$$= \frac{\hbar^2}{V_m k_{\rm B} T^2} \sum_{\mathbf{q}p} \omega^2(\mathbf{q}p) v_p^2 \tau_{\mathbf{q}p} \bar{n}_{\mathbf{q}p}(\bar{n}_{\mathbf{q}p}+1)\cos^2\theta, \tag{5.26}$$

where $\cos\theta = (\hat{\mathbf{v}}_p(\mathbf{q}) \cdot \hat{\boldsymbol{\nabla}} T)$. For isotropic three dimensional systems $\cos^2\theta = \frac{1}{3}$, and hence the thermal conductivity in the *smrt* approach becomes

$$K_{smrt} = \frac{\hbar^2}{3V_m k_{\rm B} T^2} \sum_{\mathbf{q}p} \omega^2(\mathbf{q}p) v_p^2(\mathbf{q}) \tau_{\mathbf{q}p} \bar{n}_{\mathbf{q}p}(\bar{n}_{\mathbf{q}p}+1). \tag{5.27}$$

Here, approximations based on Debye's theory should be used: The summation $\sum_{\mathbf{q}}$ can be replaced by the integral $\int \mathrm{d}q \equiv \int D(\omega)\mathrm{d}\omega$, thus the thermal conductivity can be expressed as

$$K_{smrt} = \frac{\hbar^2}{3V_m k_{\rm B} T^2} \sum_{p} v_p^2 \int_{\omega_{\rm p,min}}^{\omega_{\rm p,max}} D_p(\omega) \omega^2(\mathbf{q}p) \tau_{\mathbf{q}p} \bar{n}_{\mathbf{q}p}(\bar{n}_{\mathbf{q}p}+1)\, \mathrm{d}\omega. \tag{5.28}$$

Equation 5.28 is also known as Debye equation for thermal conductivity (*i.e.* $K_{smrt} \equiv K_{\rm D}$). Recalling Eq.(4.40), the above result can be written as the well known formula derived from the kinetic theory of gases

$$K_D = \frac{1}{3} \sum_{\mathbf{q}p} \mathrm{C}_v(\mathbf{q}p) v_p^2(\mathbf{q}) \tau_{\mathbf{q}p}. \tag{5.29}$$

5.2.3 Effective *smrt* theory (Callaway theory)

The *smrt* approximation is successful at low temperatures but slightly fails near the conductivity maximum. Callaway improved it by assuming that N-processes tend to restore a non equilibrium phonon distribution to a displaced (*drifted*) phonon distribution of the form

$$n_{\mathbf{q}p}(\mathbf{u}) = \left\{ \exp\left(\frac{\hbar\omega(\mathbf{q}p) - \mathbf{q}\cdot\mathbf{u}}{k_{\rm B}T} \right) - 1 \right\}^{-1} = \bar{n}_{\mathbf{q}p} + \frac{\mathbf{q}\cdot\mathbf{u}}{k_B T} \frac{e^{(\hbar\omega/k_B T)}}{[e^{(\hbar\omega/k_B T)}-1]^2}, \tag{5.30}$$

where $\mathbf{u}$ is a constant vector parallel to the temperature gradient. The fundamental assumption of Callaway's approach is that the rate of change of the phonon distribution function $n_{\mathbf{q}s}$ due to Normal (N) processes can be written as

$$\left.\frac{\partial n_{\mathbf{q}p}}{\partial t}\right|_N = \frac{\mathbf{q}\cdot\mathbf{u} - \psi_{\mathbf{q}p}}{\tau_N}\bar{n}_{\mathbf{q}p}(\bar{n}_{\mathbf{q}p}+1), \tag{5.31}$$

where τ_N is the relaxation time for the N-processes. If $\psi_{\mathbf{q}p} = \mathbf{q}\cdot\mathbf{u}$, then collisions which conserve total crystal momentum can have no effect on the phonon distribution. The second step is to calculate the magnitude of $\mathbf{u}$ based on the fact that the rate of change of the total crystal momentum due to N-processes must equal to zero. For further mathematical treatment, see Appendix D. It can be concluded that Callaway's equation for the thermal conductivity is

$$K_{\mathrm{C}} = K_{\mathrm{D}} + K_{\mathrm{N-drift}}, \tag{5.32}$$

where

$$K_{\mathrm{D}} = \frac{\hbar^2}{3V_m k_B T^2}\sum_p \int \mathrm{d}\omega \omega_p^2(q) v_p^2(q)\tau\bar{n}(\bar{n}+1)D_p(\omega), \tag{5.33}$$

$$K_{\mathrm{N-drift}} = \frac{\hbar^2}{3V_m k_B T^2}\sum_p \frac{\left[\int \mathrm{d}\omega D_p(\omega)\omega^2 v_p^2 \tau\tau_N^{-1}\bar{n}(\bar{n}+1)\right]^2}{\int \mathrm{d}\omega D_p(\omega)\omega^2 v_p^2\tau_N^{-1}(1-\tau\tau_N^{-1})\bar{n}(\bar{n}+1)}. \tag{5.34}$$

5.3 Phonon conductivity in graphene: Results and analysis

Before viewing the results, within Callaway's formalism, we express the lattice thermal for all polarisations p as follows

$$K_{\mathrm{C}} = \sum_p K_{\mathrm{C,p}}, \tag{5.35}$$

where

$$K_{\mathrm{C,p}} = K_{\mathrm{D,p}} + K_{\mathrm{N-drift,p}}. \tag{5.36}$$

Using the expressions for $D_p(\omega)$ from section 4.2, the thermal conductivity for the in-plane and out-of-plane modes in graphite can be written as

in-plane modes:

(i) $\omega \leq \omega_z$

$$\begin{aligned} K_{\mathrm{C,LA}}^{\mathrm{graphite}} &= \frac{1}{2}\frac{k_B^3 T^2}{\pi^2 c v_{\mathrm{LA}}^2 \hbar^2}\Bigg[\int_0^{\frac{\hbar\omega_z}{k_B T}} x^3 \frac{e^x}{(e^x-1)^2}\sin^{-1}\left(\frac{x k_B T}{\hbar\omega_z}\right)\tau v_{\mathrm{LA}}^2 \mathrm{d}x \\ &+ \frac{\left\{v_{\mathrm{LA}}^2 \int_0^{\frac{\hbar\omega_z}{k_B T}} x^3 \frac{e^x}{(e^x-1)^2}\sin^{-1}\left(\frac{x k_B T}{\hbar\omega_z}\right)\tau\tau_N^{-1}\mathrm{d}x\right\}^2}{\int_0^{\frac{\hbar\omega_z}{k_B T}} x^3 \frac{e^x}{(e^x-1)^2}\sin^{-1}\left(\frac{x k_B T}{\hbar\omega_z}\right)\tau_N^{-1}(1-\tau\tau_N^{-1})\mathrm{d}x}\Bigg]. \end{aligned} \tag{5.37}$$

$$\begin{aligned} K_{\mathrm{C,TA}}^{\mathrm{graphite}} &= \frac{1}{2}\frac{k_B^3 T^2}{\pi^2 c v_{\mathrm{TA}}^2 \hbar^2}\Bigg[\int_0^{\frac{\hbar\omega_z}{k_B T}} x^3 \frac{e^x}{(e^x-1)^2}\sin^{-1}\left(\frac{x k_B T}{\hbar\omega_z}\right)\tau v_{\mathrm{TA}}^2 \mathrm{d}x \\ &+ \frac{\left\{v_{\mathrm{TA}}^2 \int_0^{\frac{\hbar\omega_z}{k_B T}} x^3 \frac{e^x}{(e^x-1)^2}\sin^{-1}\left(\frac{x k_B T}{\hbar\omega_z}\right)\tau\tau_N^{-1}\mathrm{d}x\right\}^2}{\int_0^{\frac{\hbar\omega_z}{k_B T}} x^3 \frac{e^x}{(e^x-1)^2}\sin^{-1}\left(\frac{x k_B T}{\hbar\omega_z}\right)\tau_N^{-1}(1-\tau\tau_N^{-1})\mathrm{d}x}\Bigg]. \end{aligned} \tag{5.38}$$

(ii) $\omega \geq \omega_z$

$$\begin{aligned} K_{\mathrm{C,LA}}^{\mathrm{graphite}} &= \frac{1}{2}\frac{k_B^3 T^2}{2\pi^2 c v_{\mathrm{LA}}^2 \hbar^2}\Bigg[\int_{\frac{\hbar\omega_z}{k_B T}}^{\frac{\hbar}{k_B T}\sqrt{\frac{4\pi v_{\mathrm{LA}}^2 N_A}{A_m}+\frac{\omega_z^2}{2}}} x^3 \frac{e^x}{(e^x-1)^2}\tau v_{\mathrm{LA}}^2 \mathrm{d}x \\ &+ \frac{\left\{v_{\mathrm{LA}}^2 \int_{\frac{\hbar\omega_z}{k_B T}}^{\frac{\hbar}{k_B T}\sqrt{\frac{4\pi v_{\mathrm{LA}}^2 N_A}{A_m}+\frac{\omega_z^2}{2}}} x^3 \frac{e^x}{(e^x-1)^2}\tau\tau_N^{-1}\mathrm{d}x\right\}^2}{\int_{\frac{\hbar\omega_z}{k_B T}}^{\frac{\hbar}{k_B T}\sqrt{\frac{4\pi v_{\mathrm{LA}}^2 N_A}{A_m}+\frac{\omega_z^2}{2}}} x^3 \frac{e^x}{(e^x-1)^2}\tau_N^{-1}(1-\tau\tau_N^{-1})\mathrm{d}x}\Bigg]. \end{aligned} \tag{5.39}$$

$$K_{\mathrm{C,TA}}^{\mathrm{graphite}} = \frac{1}{2}\frac{k_B^3 T^2}{2\pi^2 c v_{\mathrm{TA}}^2 \hbar^2}\Bigg[\int_{\frac{\hbar\omega_z}{k_B T}}^{\sqrt{\frac{4\pi v_{\mathrm{TA}}^2 N_A}{A_m}+\frac{\omega_z^2}{2}}} x^3 \frac{e^x}{(e^x-1)^2}\tau v_{\mathrm{TA}}^2 \mathrm{d}x$$

$$+\frac{\left\{v_{\mathrm{TA}}^2\int_{\frac{\hbar\omega_z}{k_BT}}^{\sqrt{\frac{4\pi v_{\mathrm{TA}}^2 N_A}{A_m}+\frac{\omega_z^2}{2}}} x^3\frac{e^x}{(e^x-1)^2}\tau\tau_N^{-1}\mathrm{d}x\right\}^2}{\int_{\frac{\hbar\omega_z}{k_BT}}^{\sqrt{\frac{4\pi v_{\mathrm{TA}}^2 N_A}{A_m}+\frac{\omega_z^2}{2}}} x^3\frac{e^x}{(e^x-1)^2}\tau_N^{-1}(1-\tau\tau_N^{-1})\mathrm{d}x}\Bigg]. \tag{5.40}$$

out-of-plane modes:

(iii) $\omega \leq \omega_z'$

$$K_{\mathrm{C,ZA}}^{\mathrm{graphite}} = \frac{1}{2}\frac{k_B^3T^2}{2\pi^2cb\omega_z'\hbar^2}\Bigg[\int_0^{\frac{\hbar\omega_z'}{k_BT}}\Upsilon\, x^3\frac{e^x}{(e^x-1)^2}\tau v_{\mathrm{ZA}}^2\mathrm{d}x + \frac{\left\{v_{\mathrm{ZA}}^2\int_0^{\frac{\hbar\omega_z'}{k_BT}}\Upsilon\, x^3\frac{e^x}{(e^x-1)^2}\tau\tau_N^{-1}\mathrm{d}x\right\}^2}{\int_0^{\frac{\hbar\omega_z'}{k_BT}}\Upsilon\, x^3\frac{e^x}{(e^x-1)^2}\tau_N^{-1}(1-\tau\tau_N^{-1})\mathrm{d}x}\Bigg], \tag{5.41}$$

where $\Upsilon = \left[\int_0^{\sin^{-1}\{[1+(\zeta^2\hbar^2/4b^2k_B^2T^2x^2)]^{-1/2}\}}\left[1-\left(\frac{x^2k_B^2T^2}{\hbar^2\omega_z'^2}+\frac{\zeta^2}{4b^2\omega_z'^2}\right)\sin^2\phi\right]^{-1/2}\mathrm{d}\phi\right]$

(iv) $\omega \geq \omega_z'$

$$K_{\mathrm{C,ZA}}^{\mathrm{graphite}} = \frac{1}{2}\frac{k_B^2T}{2\pi^2cb\hbar}\Bigg[\int_{\frac{\hbar\omega_z'}{k_BT}}^{\frac{4\hbar\pi bN_A}{A_mk_BT}}\left(\sqrt{1+\frac{\hbar^2\zeta^2}{4b^2x^2k_B^2T^2}}\right)^{-1}\Pi\, x^2\frac{e^x}{(e^x-1)^2}\tau v_{\mathrm{ZA}}^2\mathrm{d}x + \frac{\left\{v_{\mathrm{ZA}}^2\int_{\frac{\hbar\omega_z'}{k_BT}}^{\frac{4\hbar\pi bN_A}{A_mk_BT}}\left(\sqrt{1+\frac{\hbar^2\zeta^2}{4b^2x^2k_B^2T^2}}\right)^{-1}\Pi\, x^2\frac{e^x}{(e^x-1)^2}\tau\tau_N^{-1}\mathrm{d}x\right\}^2}{\int_{\frac{\hbar\omega_z'}{k_BT}}^{\frac{\hbar}{k_BT}\frac{4\hbar\pi bN_A}{A_mk_BT}}\left(\sqrt{1+\frac{\hbar^2\zeta^2}{4b^2x^2k_B^2T^2}}\right)^{-1}\Pi\, x^2\frac{e^x}{(e^x-1)^2}\tau_N^{-1}(1-\tau\tau_N^{-1})\mathrm{d}x}\Bigg], \tag{5.42}$$

where $\Pi = \left[\int_0^{\pi/2}\left[1-\left(\frac{\hbar^2\omega_z'^2}{x^2k_B^2T^2}\right)\left(1+\frac{\hbar^2\zeta^2}{4b^2x^2k_B^2T^2}\right)^{-1}\sin^2\phi\right]^{-1/2}\mathrm{d}\phi\right]$.

Due to the absence of layer interactions in a monolayer graphene, ω_z and ω_z' must be set to zero. Thus, only Eq.(5.39), Eq.(5.40), and Eq.(5.42) can be considered for evaluating graphene thermal conductivity. These equations can be re-written as follows

$$K_{\mathrm{C,LA}}^{\mathrm{graphene}} = \frac{1}{2}\frac{k_B^3T^2}{2\pi^2 c v_{\mathrm{LA}}^2\hbar^2}\left[\int_0^{\frac{\hbar}{k_BT}\sqrt{\frac{4\pi v_{\mathrm{LA}}^2 N_A}{A_m}}} x^3\frac{e^x}{(e^x-1)^2}\tau v_{\mathrm{LA}}^2\mathrm{d}x + \frac{\left\{v_{\mathrm{LA}}^2\int_0^{\frac{\hbar}{k_BT}\sqrt{\frac{4\pi v_{\mathrm{LA}}^2 N_A}{A_m}}} x^3\frac{e^x}{(e^x-1)^2}\tau\tau_N^{-1}\mathrm{d}x\right\}^2}{\int_0^{\frac{\hbar}{k_BT}\sqrt{\frac{4\pi v_{\mathrm{LA}}^2 N_A}{A_m}}} x^3\frac{e^x}{(e^x-1)^2}\tau_N^{-1}(1-\tau\tau_N^{-1})\mathrm{d}x}\right]. \quad (5.43)$$

$$K_{\mathrm{C,TA}}^{\mathrm{graphene}} = \frac{1}{2}\frac{k_B^3T^2}{2\pi^2 c v_{\mathrm{TA}}^2\hbar^2}\left[\int_0^{\frac{\hbar}{k_BT}\sqrt{\frac{4\pi v_{\mathrm{TA}}^2 N_A}{A_m}}} x^3\frac{e^x}{(e^x-1)^2}\tau v_{\mathrm{TA}}^2\mathrm{d}x + \frac{\left\{v_{\mathrm{TA}}^2\int_0^{\frac{\hbar}{k_BT}\sqrt{\frac{4\pi v_{\mathrm{TA}}^2 N_A}{A_m}}} x^3\frac{e^x}{(e^x-1)^2}\tau\tau_N^{-1}\mathrm{d}x\right\}^2}{\int_0^{\frac{\hbar}{k_BT}\sqrt{\frac{4\pi v_{\mathrm{TA}}^2 N_A}{A_m}}} x^3\frac{e^x}{(e^x-1)^2}\tau_N^{-1}(1-\tau\tau_N^{-1})\mathrm{d}x}\right]. \quad (5.44)$$

$$K_{\mathrm{C,ZA}}^{\mathrm{graphene}} = \frac{1}{2}\frac{k_B^2T}{2\pi^2 cb\hbar}\left[\int_0^{\frac{4\hbar\pi bN_A}{A_m k_B T}} \Pi(\phi)\, x^2\frac{e^x}{(e^x-1)^2}\tau v_{\mathrm{ZA}}^2\mathrm{d}x + \frac{\left\{v_{\mathrm{ZA}}^2\int_0^{\frac{4\hbar\pi bN_A}{A_m k_B T}} \Pi(\phi)\, x^2\frac{e^x}{(e^x-1)^2}\tau\tau_N^{-1}\mathrm{d}x\right\}^2}{\int_0^{\frac{\hbar}{k_BT}\frac{4\hbar\pi bN_A}{A_m k_B T}} \Pi(\phi)\, x^2\frac{e^x}{(e^x-1)^2}\tau_N^{-1}(1-\tau\tau_N^{-1})\mathrm{d}x}\right], \quad (5.45)$$

where $\Pi = \int_0^{\pi/2}\mathrm{d}\phi$. In all thermal conductivity expressions for graphene and graphite, the factor $(\frac{1}{2})$ at the beginning of each equation reflects the nature of the two-dimensional characteristics of the system.

The results of phonon conductivity calculations, with a suspended sample of grapene of length $L = 2.9\ \mu\mathrm{m}$ and consideration of vacancy concentration $c_d = 1.0\times10^{-6}$ are shown in Fig. 5.2. It is evident that the full Callaway theory (K_{C}, using both terms in Eqs.(5.43–5.45)) produces much higher conductivity values than does the single-mode relaxation time theory (K_{D}, using only the first terms in Eqs.(5.43–5.45)). This is particularly the case in the temperature range 150K -

600K. We estimate the Normal-drift contribution ($K_{\mathrm{N-drift}}$) to be twice as big of K_{D} at 300K. In this temperature range, in addition to presenting a much higher magnitude, K_{C} also shows a different temperature variation than K_{D}.

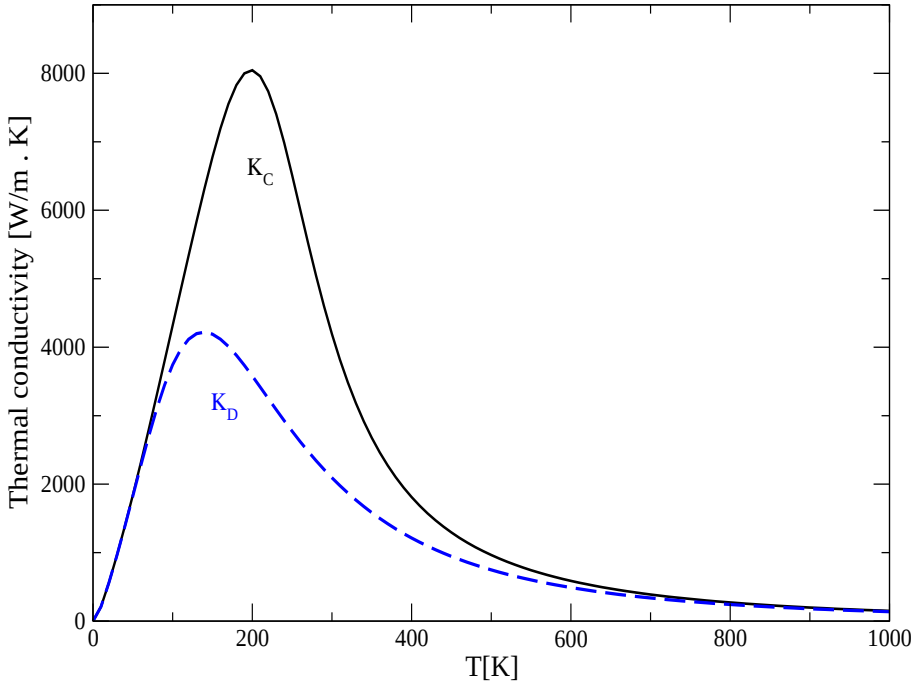

Figure 5.2: The contributions K_{C} (full Callaway theory) and K_{D} (Debye term) to the thermal conductivity of a graphene sample of length $L = 2.9\mu\mathrm{m}$ with an assumed vacancy concentration $c_d = 1.0 \times 10^{-6}$.

In Fig. 5.3, we have presented separate contributions from the three phonon branches. We find that at room temperature the contribution to the full thermal conductivity K_{C} from the ZA phonons is approximately 2.1 times larger than that from the LA phonons and approximately 1.8 times that from the TA phonons. The significantly large contribution from the ZA phonons can be attributed to two factors. First, as pointed out earlier, the specific heat contribution from the ZA phonons is larger than that of the LA and TA phonons. Second, the relaxation

time of the ZA phonons is much larger than that of the LA and TA phonons. The low-temperature dependence of the thermal conductivity is almost the same as that of the specific heat.

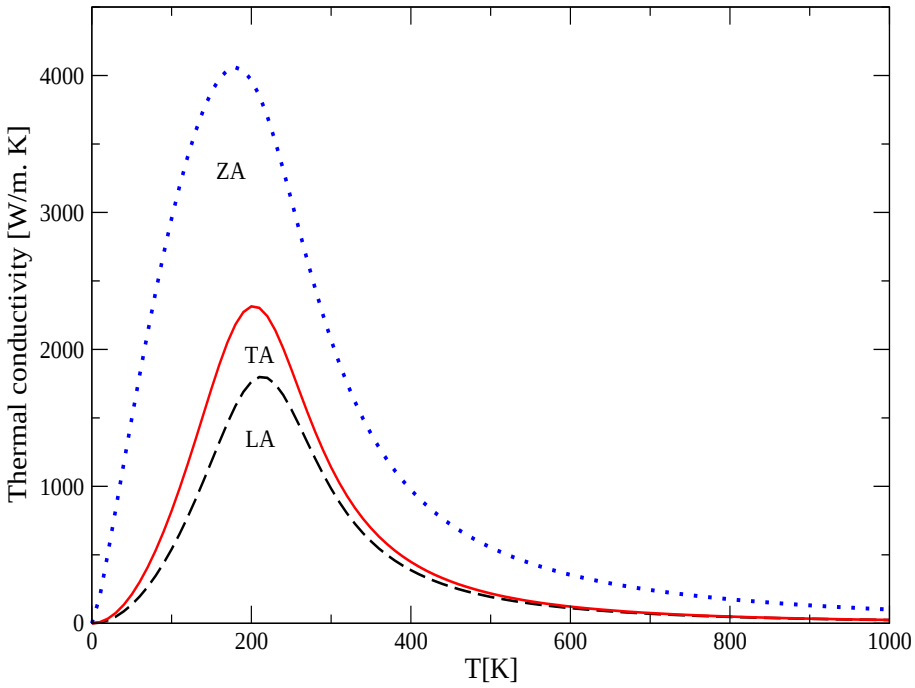

Figure 5.3: $K_{\mathrm{C,ZA}}$ for CVD-grown graphene with 2.9μm length is dominant over $K_{\mathrm{C,LA}}$ and $K_{\mathrm{C,TA}}$.

Figure 5.4 compares our theoretical K_{C} results with the experimental results for suspended graphene presented in Refs. [36, 37]. There is a wide range of thermal conductivity values for graphene due to different preparation methods and various measurement techniques [38]. Therefore, before discussing the comparison, we provide a brief reminder on the sample preparation and the conductivity measurement technique employed by the various experimental groups. The experiment carried out by Chen *et.al*. [37] used a sample of a monolayer graphene grown by the chemical vapor deposition (CVD) on copper and then suspended

over holes with different diameters ranging from 2.9 to 9.7μm. The thermal conductivity was measured by the micro-Raman spectroscopy. The experiment conducted by Cai *et.al*. [36] used a sample of a monolayer graphene grown by CVD on copper and then suspended over a hole with a sample length of 3.8 μm, and the thermal conductivity was measured using the micro-Raman spectroscopy.

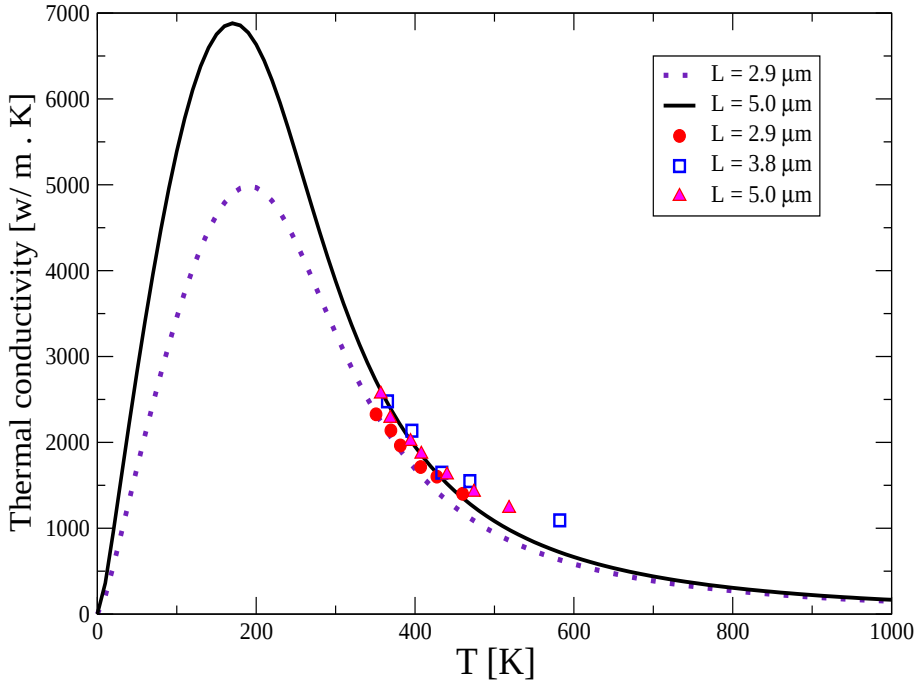

Figure 5.4: Calculated thermal conductivity (lines), using the Callaway theory, compared with experimental measurements (symbols) in Refs.[36, 37] for suspended graphene with different sample lengths L.

In order to fit theory with the experimental data we used the following parameters: $c_d = 1.0 \times 10^{-5}$, $B_U = 7.7 \times 10^{-25}$ s.K^{-3}, and $B_N = 3.85 \times 10^{-25}$ s.K^{-3}. Following the discussion presented by Chen *et al.* [37], it is clear that there is a large error margin in 'extracting' thermal conductivity values from optical measurements, Lee *et al.* [39] found that their values of the thermal conductivity are

lower than those reported for the CVD graphene and they accounted this for a significant difference in the estimate of the absorbtance and transmittance of light incident on the sample. Moreover, there is always some uncertainty about the type and concentration of point defects in a given graphene sample. Keeping these points in mind, we should consider the comparison between theory and the experimental results in Refs. [36, 37] as quite good. Based on an attempt to fit the experimental data, our theoretical work suggests that the maximum value of the thermal conductivity of a typical graphene sample of these qualities should lie in the range 5000 - 7000 W m^{-1} K^{-1} and in the temperature range 150 - 250 K. Our work also suggests that the room temperature conductivity of graphene should range between 3000 and 3800 W m^{-1} K^{-1}. This estimate is lower than the first experimental measurement of around 5300 W m^{-1} K^{-1} in Ref. [38], but higher than the in-plane conductivity of graphite of around 1950 W m^{-1} K^{-1} [40].

5.3.1 Sample size (micron range) dependence of conductivity

The low-temperature mean-free path of phonons is expected to be heavily controlled by the boundary scattering. The meaning of 'low temperature regime' may depend on the numerical value of the effective boundary scattering length, which in turn is determined by the shape and size of the system under consideration. Figure 5.5 shows the variation of the thermal conductivity of graphene as a function of sample size (in micron range) at different temperatures. Without being specific about the geometry of graphene, we consider L to represent an effective sample boundary length for phonon scattering. The sample could be a square sheet, a rectangular sheet, or a nano ribbon, with the effective boundary length L. Our results can be expressed with the help of the following empirical relationship between the thermal conductivity K_C and the effective boundary length:

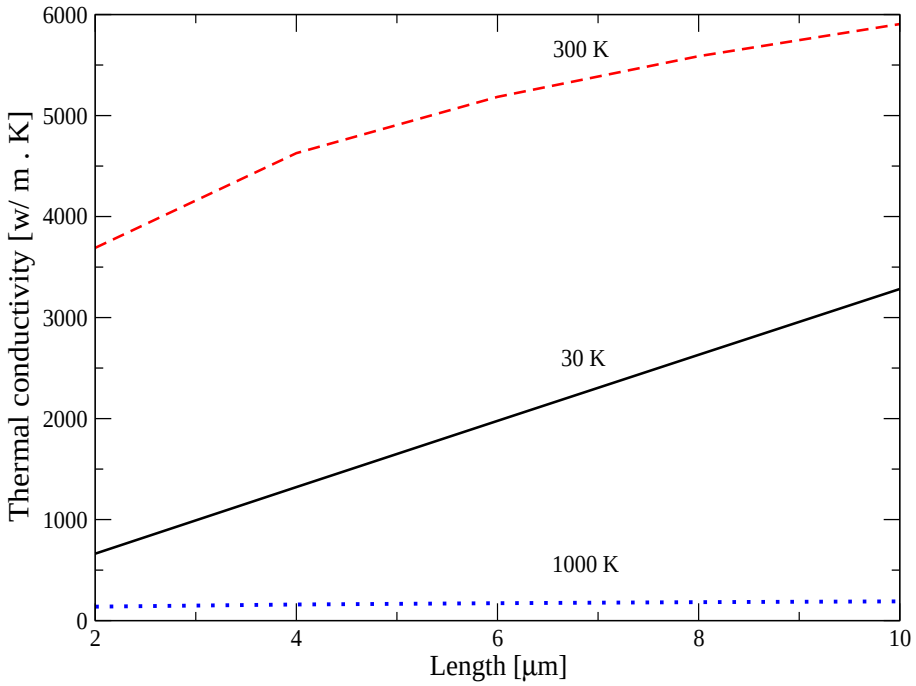

Figure 5.5: Thermal conductivity as a function of length, L on micron scale.

$$K_{\mathrm{C}} = R_T L^{\beta_T} \tag{5.46}$$

where R_T and β_T are constants in the range of very low temperature T. Our results suggest the following fits

$$\begin{aligned} R_{30} &= 328.89, \qquad \beta_{30} = 1 \\ R_{300} &= 3056.80, \qquad \beta_{300} = 0.29 \\ R_{1000} &= 120.50, \qquad \beta_{1000} = 0.2 \end{aligned} \tag{5.47}$$

These results indicate that the conductivity varies linearly with length up to 30 K. This, in turn, indicates that the boundary scattering regime for the sample under study is up to 30 K. This is contradicted by the investigation of Wei *et al.* [41] who have shown that the thermal conductivity of a single layer of graphene sheet

increases almost linearly with the length at room temperature. Our results for the length dependence of the conductivity at room temperature, *viz.* $K_{\rm C} \propto L^{0.29}$, is totally consistent with the trend obtained in the theoretical study by Lindsay *et al.* [42]. As expected, there is virtually no strong length dependence of the conductivity at high temperatures, such as 1000 K.

5.3.2 Room temperature results for graphene nanoribbons

The results for $K_{\rm C}$ with L on the nanometer scale have been presented in Fig. 5.6. There is seen to be a reduction to phonon conductivity as length decreases. Also, the peak in the conductivity shifts towards higher temperature as the boundary scattering length decreases. When the boundary scattering length reduces to values around the mean free path of dominant phonon modes, the temperature dependence of the conductivity is essentially that of the specific heat. This can be clearly seen from the bottom curve in Fig. 5.6, which shows there is almost no peak in the $K_{\rm C}$ *vs.* T curve for the nanoribbon of $L = 10$ nm. We find that, in contrast to the micron range, there is a slightly different variation of the conductivity of GNRs with length as seen in Fig. 5.7. In the range $L = 100 - 500$ nm, we find the room-temperature conductivity to vary approximately as $K_{\rm C} \approx 24\ L^{0.68}$.

5.3.3 Effect of polymeric residue on phonon conductivity

Pettes *et.al*. [43] have prepared a suspended bilayer graphene and made measurements of the phonon conductivity. In their work, bilayer graphene sheets were located via optical microscopy of graphitic crystals exfoliated mechanically from natural graphite flakes onto poly(methyl methacrylate) (PMMA) film coated onto a silicon substrate. The PMMA was then dissolved by placing the sample in acetone at ~ 60 °C. It was found that the room-temperature thermal conductivity of this sample is close to the conductivity values in the region of 600 K for the

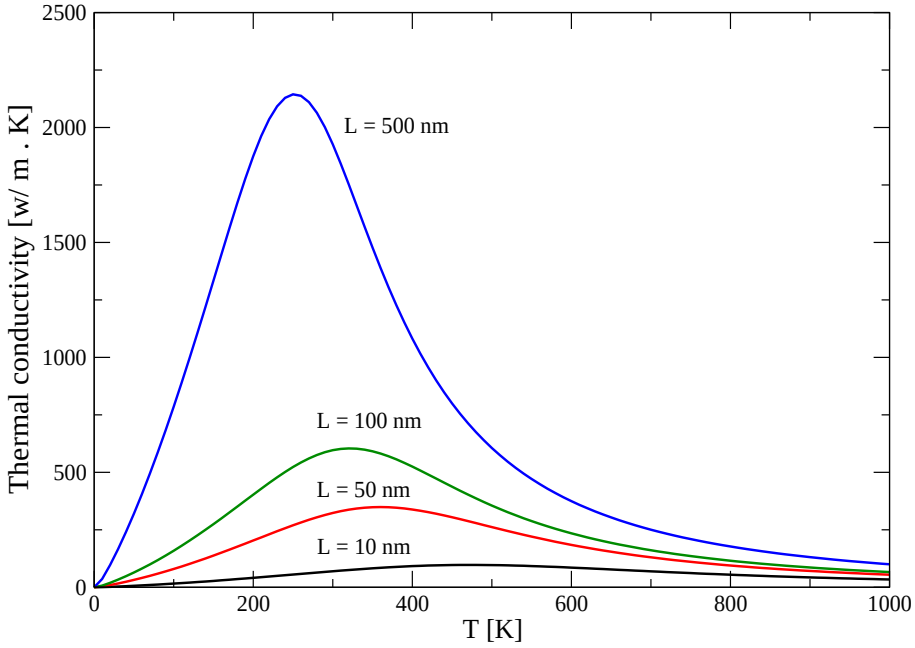

Figure 5.6: Thermal conductivity of GNRs for different lengths.

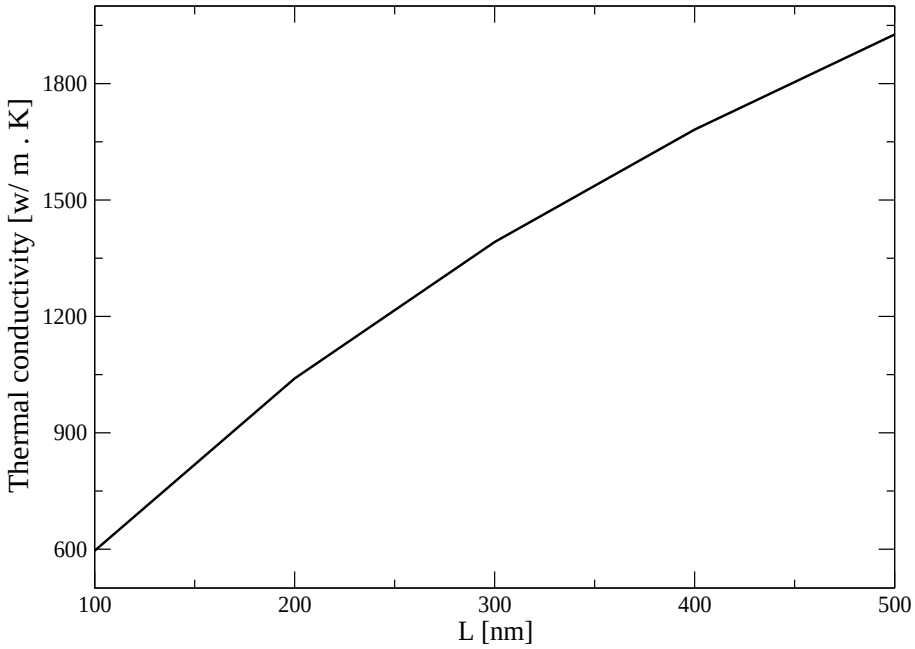

Figure 5.7: Thermal conductivity of GNRs as a function of length L at $T = 300$ K.

samples reported in Fig. 5.4. This reduction has been attributed to defect-like scattering of phonons by a residual polymeric layer that acts as a support layer for the graphene sample. The experimental results have been successfully reproduced in Fig. 5.8 by considering $L = 0.25$ μm and $c_d^{\text{PMMA defect}} = 17.0 \times 10^{-6}$ for the additional defect-like scattering of phonons due to the residual polymeric

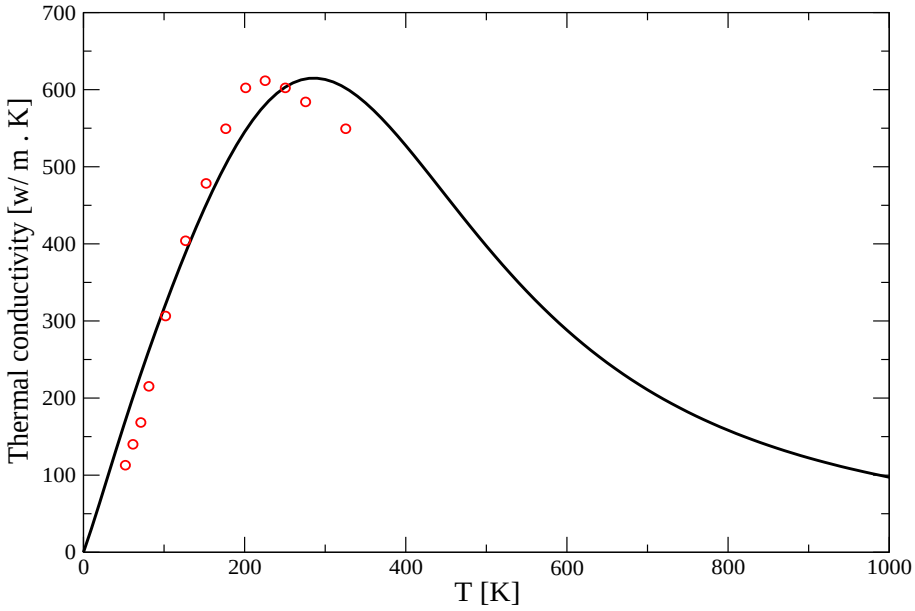

Figure 5.8: The calculated K_{C} (solid line) and experimental results (symbols) for the bilayer graphene sample prepared by Pettes *et al.* [43].

content. As seen in Fig. 5.9, for graphene with this level of point defects, the difference between K_{C} and K_{D} becomes less pronounced: at room temperature $K_{\text{N-drift}}$ is only 18% of K_{D}. This vindicates our assertion that for pure graphene (i.e. graphene with a reasonably small amount of defects), the full Callaway formulation must be employed to obtain quantitatively accurate thermal conductivity results.

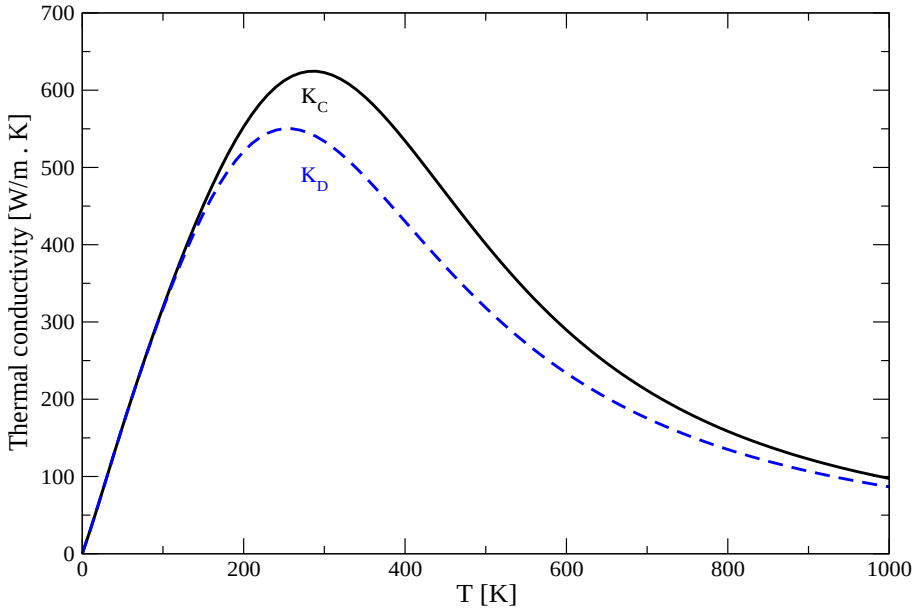

Figure 5.9: Comparison between K_{C} and K_{D} for the graphene sample prepared by Pettes *et al.* [43].

5.4 Summary

In this chapter, the concept of thermal conductivity has been discussed. The theories of single-mode-relaxation time and effective single-mode-relaxation time have been introduced within the frame of Boltzmann transport equation. Phonon-boundary scattering, phonon-defects scattering, and phonon-phonon scattering have been discussed. The importance of N-processes within Callaway theory for the thermal conductivity has been addressed. We have employed a semi-continuum theory for phonon dispersion relations and Callaway's formalism in full to study the thermal conductivity in graphene and its nanoribbons. We have concluded that a reasonable estimate of the thermal conductivity of graphene can be made by employing Callaway's effective relaxation time method, provided that the size and purity of the sample is known. We have shown that the N-drift term in the Callaway theory must be included for obtaining the correct magni-

tude and temperature variation of the conductivity of graphene. The present theory successfully explains the experimental measurements of the conductivity of graphene, and of bilayer graphene containing residual PMMA contents. The theory shows that the boundary regime for the conductivity of suspended graphene extends up to $T = 30$ K. Our results show different length dependencies of the thermal conductivity for different ranges of sample size. For micron-sized samples, around room temperature, the variation of the conductivity is proportional to $L^{0.29}$. In contrast, the conductivity of nanoribbons (nano-sized samples) shows a much stronger length dependence, which has been estimated to be proportional to $L^{0.68}$.

Bibliography

[1] J. Callaway, Phys. Rev. **113**, 1046 (1959).

[2] M. G. Holland, Phys. Rev. **132**, 2461 (1963).

[3] T. Nihira and T. Iwata, Phys. Rev. B **68**, 134305 (2003).

[4] G. P. Srivastava, *The Physics of Phonons* (Adam Hilger, Bristol, 1990).

[5] H. B. Casimir, Physica **5**, 495 (1938).

[6] R. Berman, F. E. Simon, and J. M. Ziman, Proc. Roy. Soc. A **220**, 171 (1953).

[7] R. Berman, E. L. Foster, and J. M. Ziman, Proc. Roy. Soc. A **231**, 130 (1955).

[8] P. Carruthers, Rev. Mod. Phys. **33**, 92 (1961).

[9] J. M. Ziman, *Electrons and Phonons*, (Oxford University Press, Clarendon, 1967).

[10] I. Pomeranchuk, J. Phys. U.S.S.R. **5**, 237 (1942).

[11] P. G. Klemens, J. Wide Bandgap Mater. **7**, 332 (2000).

[12] P. G. Klemens and D. F. Pedraza, Carbon, **32**, 735 (1994).

[13] C. A. Ratsifaritana and P. G. Klemens, Int. J. Thermophys. **8**, 737 (1987).

[14] S. Chen, Q. Wu, C. Mishra, J. Kang, H. Zhang, K. Cho, W. Cai, A. A. Balandin, and R. S. Ruoff, Nature (London) **11**, 203 (2012).

[15] V. Adamyan and V. Zavalniuk, J. Phys.: Condens. Matter **23**, 1 (2011).

[16] G. P. Srivastava, High Thermal Conductivity Materials, Ch. 1, (Springer Science:Business Media, New Nork, 2006).

[17] M. Kaviany, *Heat Transfer Physics* (Cambridge University Press, New York, 2008).

[18] J. M. Ziman, *Electrons and Phonons* (Clarendon, Oxford, 1960).

[19] C. Herring, Phys. Rev. **95**, 954 (1954).

[20] P. G. Klemens, *Solid State Physics*, **7**, ed F. Seitz and D. Turnbull (New York: Academic, 1958) p 1.

[21] G. A. Slack and S. Galginaitis, Phys. Rev. **133**, A253 (1964).

[22] G. L. Guthrie, Phys. Rev. **152**, 801 (1966).

[23] M. G. Holland, Phys. Rev. **134**, A471 (1964).

[24] P. G. Klemens, Proc. R. Soc. (London) **A 68**, 1113 (1965).

[25] P. C. Sharma, K. S. Dubey, and G. S. Verma, Phys. Rev. B **3**, 1985 (1971).

[26] M. D. Tiwari and K. B. Agrawal, Phys. Rev. B **4**, 3527 (1971).

[27] K. C. Sood and M. K. Roy, J. Phys.: Condens. Matter **5**, 301 (1993).

[28] M. Asen-Palmer, K. Bartkowski, E. Gmelin, M. Cardona, A. P. Zhernov, A. V. Inyushkin, A. Taldenkov, V. I. Ozhogin, K. M. Itoh, and E. E. Haller, Phys. Rev. B **56**, 9431 (1997).

[29] G. A. Slack and S. Galginaitis, Phys. Rev. **133**, 253 (1964).

[30] L.E. Fried and W. M. Howard, Phys. Rev. B **61**, 8734 (2000).

[31] R. G. Steg, and P. G. Klemens, Phys. Rev. Lett. **24**, 381 (1970).

[32] D. L. Nika, S. Ghosh, E. P. Pokatilov, and A. A. Balandin, Appl. Phys. Lett. **94**, 203103 (2009).

[33] P. G. Klemens, Proc. Roy. Soc. (London) **A208**, 108 (1951).

[34] R. E. Peierls, Ann. Physik **3**, 1055 (1929).

[35] G. P. Srivastava, J. Phys. Chem. Solids **41**, 357 (1980).

[36] W. Cai, A. L. Moore, Y. Zhu, X. Li, S. Chen, L. Shi, and R. S. Ruoff, Nano Lett. **10**, 1645 (2010).

[37] S. Chen, A. L. Moore, W. Cai, J. W. Suk, J. An, C. Mishra, C. Amos. C. W. Magnuson, J. Kang, L. Shi, and R. S. Ruff, ACS Nano **5**, 321 (2011).

[38] A. A. Balandin, S. Ghosh, W. Bao, I. Calizo, D. Teweldebrhan, F. Miao, and C. N. Lau, Nano Lett. **8**, 902 (2008).

[39] J.-U. Lee, D. Yoon, H. Kim, S. W. Lee, and H. Cheong, Phys. Rev. B **83**, 081419(R) (2011).

[40] G. A. Slack, Phys. Rev. **127**, 694 (1962).

[41] Z. Wei, Z. Ni, K. Bi, M. Chen, and Y. Chen, Carbon, **49**, 2653 (2011).

[42] L. Lindsay, D. A. Broido, and N. Mingo, Phys. Rev. B **82**, 115427 (2011).

[43] M. T. Pettes, I. Jo, Z. Yao, and L. Shi, Nano Lett. **11**, 1195 (2008).

Chapter 6

Tuning Thermal Properties of Graphene and Graphite

6.1 Introduction

Growing challenges in thermal management arise as the size of the electronic devices enters the nanometer regime. Facing these challenges requires the search for ways to control the performance and the thermal efficiency of theses devices by modifying their thermal properties. Generally, thermal properties of materials, including graphene ribbons, can be 'phonon engineered' in several ways. Boundary edge roughness, defect and isotope concentration, mechanical strain, atomic planes, and grain boundaries are considered to be among the tuning factors. Only the first two factors will be discussed in detail in this chapter.

As mentioned previously, in defect-free and perfect single crystals of non-metallic materials, phonon scattering, at low temperatures, occurs mostly at the crystal boundaries. Thus, the thermal conductivity is independent of the crystal but depends upon its dimensions. This size-effect was observed experimentally by de Haas and Biermasz [1], and a theoretical investigation of boundary scattering of

phonons was addressed by Casimir [2] more than 70 years ago. Later on, Berman, Simon, and Ziman [3] have extended the Casimir theory (hereafter referred to as BSZ) to modify the Casimir length by a factor containing a momentum-dependent specularity parameter which is a function of edge roughness and temperature. The specularity parameter is considered to be a measure of the diffuseness of phonon scattering and its value lies in the range between one for perfectly diffuse scattering and zero for perfectly specular reflection. A temperature dependence of this parameter occurs because with decreasing temperature the average phonon wavelength increases and a boundary of given roughness appears smoother. Since lateral thermal conduction in thin films is significantly affected by boundary scattering, a graphene monolayer is supposed to be affected accordingly. Theoretically, it has been found that scattering from the rough edges of graphene ribbons causes the thermal conductivity to decrease with increasing edge roughness and decreasing width [4, 5, 6].

Investigation of dynamical properties of solids at high pressures is important. Applying stress or strain on a solid provides a mechanism to alter its properties (mechanical, electrical, optical, and thermal). Due to the anisotropy of graphite crystal structure, its compressibility is also anisotropic. Young's modulus is about 1020 GPa for the in-plane and it is only 37 GPa for the out-of-plane or (c-axis) direction at atmospheric pressure [7]. In 1924, Bridgman [8] studied the thermal conductivity and compressibility of several rocks under high pressures, thus it has been long perceived that hydrostatic pressure influences heat transport in solids. In 1984, a review study by Ross *et al.* [9] on the thermal conductivity of a wide variety of solids and liquids under pressure is presented. They concluded that the thermal conductivity of semiconductors increases with compressive strain. Recently, interest in the theory of the variation of thermal conductivity of low dimensional solids with applied strain is growing fast among several au-

thors. Li *et al.* [10] studied the strain/stress effects on the thermal conductivity of low- dimensional silicon and carbon materials by using equilibrium molecular dynamics (MED) simulation. They reported that tensile strains induce an increase of thermal conductivity of nanostructures, while compressive strains lead to the opposite effect. Also they investigated the changes in specific heat and phonon group velocity of both bulk silicon and diamond by calculating the dispersion relations under compressive uniaxially strains. They observed that the phonon dispersion curves shift upward which in turn results in the increase of both phonon group velocity and specific heat. Picu *et al.* [11] investigated the role of strain on heat transport nanostructures by molecular dynamics simulations of a model Lennard-Jones solid. They observed an increase and decrease of thermal conductivity due to compressive and tensile strains, respectively. By using a none-equilibrium molecular dynamics method (NEMD), Jianwei *et al.* [12], concluded that the thermal conductivity of monolayer graphene nanoribbons (GNRs) can be decreased $20\% \sim 30\%$ by applying tensile strain in the range $9\% \sim 15\%$. First principle calculations based on density functional theory (DF) was employed by Ma *et al.* [13] to study the phonon spectrum, the specific heat, and the thermal conductivity of graphene under uniaxial tensile strain. They reported that the heat capacity increases while thermal conductivity declines due to the strengthening of Umklapp scattering. By contrast, Zhai *et al.* [14], implemented a combination of the non-equilibrium Greens function model with the elastic theory to investigate the ballistic thermal transport in GNRs under homogeneous uniaxial stretching. They reported an extraordinary enhancement of graphene thermal conductance up to 36% under homogeneous uniaxial strain.

Experimentally, modifications in phonon dispersion relations and elastic properties of graphite at normal pressure can be investigated by Raman scattering, infrared reflectance, inelastic neutron scattering, and elastic constant measurements

(see Ref. [15]). Experimental investigations have been performed by Ivanon *et al.* [16] to study the lattice dynamics of graphite at high pressures by neutron inelastic scattering using anvils technique. They have shown that under the application of compressive pressure, the interlayer distances contract and give rise to a hardening of the measured frequencies in the phonon dispersion relations. Also, they concluded that the elastic constants C_{33} and C_{44} are enlarged significantly (five times larger than their original values) under compressive strain while other constants related to the interlayer atomic distances are much less responsive and sensitive.

The strong anisotropy of the bonding in graphite is reflected in its elastic and vibrational properties. As a result of this anisotropy, there are two principal thermal conductivities to be evaluated. The conductivity measured in any direction parallel to the basal planes is denoted by K_a and that parallel to the hexagonal axis is K_c, thus the components of the conductivity tensor are $K_{xx} = K_{yy} = K_a$, and K_{zz} = K_c. The thermal conductivity along the c-axis in graphite is found to be two orders of magnitude smaller than graphene thermal conductivity, making it promising for devices with improved thermoelectric figure of merit.

In this chapter, the thermal conductivity tensor elements are computed. In order to do that, we will re-express Eq.(5.33) and Eq.(5.34) as tensor elements, incorporating analytically derived expressions for velocity components. The conductivity of graphene is predicted to be higher than the in-plane conductivity of graphite for all temperatures. The effects of edge roughness, ^{13}C isotope, and tensile strain on the conductivity of graphene are studied. Also, the effect of compressive strain along graphite c-axis on the thermal conductivity of graphite is investigated.

6.2 Theory

6.2.1 Thermal conductivity tensor

The theory of the thermal vibrations of the carbon atoms in the graphite crystal has been addressed by a number of authors [17, 18, 19]. In this thesis, calculations for thermal conductivity of graphene and graphite are all carried out using the theoretical method described in section 5.3 but with the explicit inclusion of the velocity components required for tensor elements ($K_{xx} = K_{yy} = K_a$, and $K_{zz} = K_c$). Within the semicontinuum model, the elements $K_{\alpha\beta}$ of the thermal conductivity tensor is given as [17]

$$K_{\alpha\beta} = \sum_{\boldsymbol{q},p} k_B \left[\frac{\hbar\omega_p(\boldsymbol{q})}{k_B T}\right]^2 \tau_p(\boldsymbol{q}) \frac{\exp\ [\hbar\omega_p(\boldsymbol{q})/k_B T]}{\{\exp\ [\hbar\omega_p(\boldsymbol{q})/k_B T] - 1\}^2} \{v_p(\boldsymbol{q})\}_\alpha \{v_p(\boldsymbol{q})\}_\beta. \quad (6.1)$$

Here, $\{v_p(\boldsymbol{q})\}_\alpha, v_p\{(\boldsymbol{q})\}_\beta$ are the components of the phonon velocity: in direction α, and β ($\alpha, \beta = x, y\ or\ z$). Within Callaway's formalism, we express the lattice thermal conductivity tensor as

$$\{K_{\alpha\beta}\}_{\mathrm{C}} = \{K_{\alpha\beta}\}_{\mathrm{D}} + \{K_{\alpha\beta}\}_{\mathrm{N-drift}}. \quad (6.2)$$

For the sake of clarity and simplicity, the phonon dispersion relation for the three acoustic modes in graphite are re-expressed as follows

$$\begin{aligned} \omega_1^2 &= v_{\mathrm{LA}}^2(q_x^2 + q_y^2) + \frac{4\zeta}{c^2}\sin^2(cq_z/2), \\ \omega_2^2 &= v_{\mathrm{TA}}^2(q_x^2 + q_y^2) + \frac{4\zeta}{c^2}\sin^2(cq_z/2), \\ \omega_3^2 &= b^2(q_x^2 + q_y^2)^2 + 4\mu^2\sin^2(cq_z/2) + \zeta(q_x^2 + q_y^2), \end{aligned} \quad (6.3)$$

The subscripts 1 and 2 refer to the LA and TA modes, respectively, while the subscript 3 refers to the ZA mode. The phonon propagation velocities in crystals are

derived from the phonon dispersion relation. In Eq.(6.1), the velocities $\{v_p(\mathbf{q})\}_{\alpha,\beta}$ are generally assumed to be the group velocities of each vibrational mode given by:

$$\{v_p(\mathbf{q})\}_x = \frac{\partial\omega_p(\mathbf{q})}{\partial\mathbf{q_x}} \quad , \quad \{v_p(\mathbf{q})\}_z = \frac{\partial\omega_p(\mathbf{q})}{\partial\mathbf{q_z}}. \tag{6.4}$$

The phonon group velocities in graphite derived from Eq. (6.3) are

$$(v_1)_x = \frac{v_{\mathrm{LA}}^2 q_x}{\sqrt{v_{\mathrm{LA}}^2 q_a^2 + (4\zeta/c^2)\sin^2(cq_z/2)}}, \tag{6.5a}$$

$$(v_2)_x = \frac{v_{\mathrm{TA}}^2 q_x}{\sqrt{v_{\mathrm{TA}}^2 q_a^2 + (4\zeta/c^2)\sin^2(cq_z/2)}}, \tag{6.5b}$$

$$(v_1)_z = \frac{\zeta\sin(cq_z)}{c\sqrt{v_{\mathrm{LA}}^2 q_a^2 + (4\zeta/c^2)\sin^2(cq_z/2)}}, \tag{6.5c}$$

$$(v_2)_z = \frac{\zeta\sin(cq_z)}{c\sqrt{v_{\mathrm{TA}}^2 q_a^2 + (4\zeta/c^2)\sin^2(cq_z/2)}}, \tag{6.5d}$$

$$(v_3)_x = \frac{2b^2 q_a^3 + \zeta q_a}{\sqrt{b^2 q_a^4 + 4\mu^2\sin^2(cq_z/2) + \zeta q_a^2}}, \tag{6.5e}$$

$$(v_3)_z = \frac{\mu^2 c\sin(cq_z)}{\sqrt{b^2 q_a^4 + 4\mu^2\sin^2(cq_z/2) + \zeta q_a^2}}, \tag{6.5f}$$

where $(v_1)_x$ and $(v_2)_x$ are the velocity components from LA and TA phonons respectively along the basal plane, $(v_1)_z$ and $(v_2)_z$ are the velocity components from LA and TA phonons respectively along the normal to the plane, and $(v_3)_x$ and $(v_3)_z$ are the velocity components of the ZA phonons along and normal to the

basal plane respectively.

For computing the thermal conductivity in graphene, Eq.(5.43), Eq.(5.44), and Eq.(5.45) are applied. Since in graphene the layer planes are uncoupled: this is ensured by setting $\mu = 0, \zeta = 0$, and $q_z = 0$, and the phonon group velocity components reduce to

$$\begin{aligned} (v_1)_x &= v_{\mathrm{LA}}, \\ (v_2)_x &= v_{\mathrm{TA}}, \\ (v_3)_a &= 2bq_a = 2\sqrt{b\,\omega_3}. \end{aligned} \tag{6.6}$$

These also apply for graphite basal plane vibrations parallel to q_a and Eqs. (5.37)–(5.42) are used. For graphite basal plane vibrations parallel to q_z only, it can be assumed that $q_a = 0$. From Eq.(6.5), the following phonon group velocity components should be substituted in Eq.(5.37), Eq.(5.38), and Eq.5.41

$$\begin{aligned} (v_1)_z &= \sqrt{\zeta}\cos(cq_z/2), \\ (v_2)_z &= \sqrt{\zeta}\cos(cq_z/2), \\ (v_3)_z &= c\mu\cos(cq_z/2). \end{aligned} \tag{6.7}$$

6.2.2 Boundary scattering

It is assumed that there are boundaries parallel and perpendicular to the hexagonal axis defining scattering lengths L_c and L_a respectively. A particular phonon may be scattered by either type of boundary and the relaxation time of a phonon is thus given by

$$\tau_{bs} = \frac{L_a}{\{v_p\}_a}; \quad \tau_{bs} = \frac{L_c}{\{v_p\}_z}. \tag{6.8}$$

The boundary perpendicular to the hexagonal axis dominates the scattering of phonons for which $L_a/\{v_p\}_a \gg L_c/\{v_p\}_z$ while that parallel to the hexagonal axis dominates the scattering of phonons for which $L_c/\{v_p\}_z \gg L_a/\{v_p\}_a$. Clearly, the boundary scattering rate depends upon the phonon mode involved.

6.2.3 Effect of boundary edge roughness in graphene ribbon

The relaxation time of a phonon with wave vector $\mathbf{q}$ and polarisation p due to the interaction with rough edges is then given as follows [20]

$$\tau_{er,p}(\mathbf{q}) = \left[\frac{1+R}{1-R}\right] \frac{W}{v_{p,\perp}(\mathbf{q})}, \tag{6.9}$$

where R is the specular parameter ($0 \leq R \leq 1$), W is the width of the graphene ribbon, and $v_{p,\perp}$ is the perpendicular component of the phonon velocity of particular polarisation p to the idealized smooth edge of the ribbon. The specular parameter is related to the phonon momentum through the following expression [5]

$$R(q) = \exp\left[-(2q\eta\cos\Theta_B)^2\right], \tag{6.10}$$

where Θ_B is the angle of incidence of the phonon of wave number q, as seen in Fig 6.1, and η is the asperity parameter which is the root mean square (rms) deviation of the height of the sample surface from a smooth, ideal shape (edge roughness). Since the temperature gradient is parallel to the length of the sample, then $\Theta_B = \frac{\pi}{2} - \varrho$, where ϱ is the angle between the temperature gradient direction and the phonon wave vector. If we make use of the relation $q \equiv q(\omega_p)$ for different phonon modes in graphene, then we get

$$R(\omega_p) = \exp\left[-(2q(\omega_p)\eta\sin\varrho)^2\right]. \tag{6.11}$$

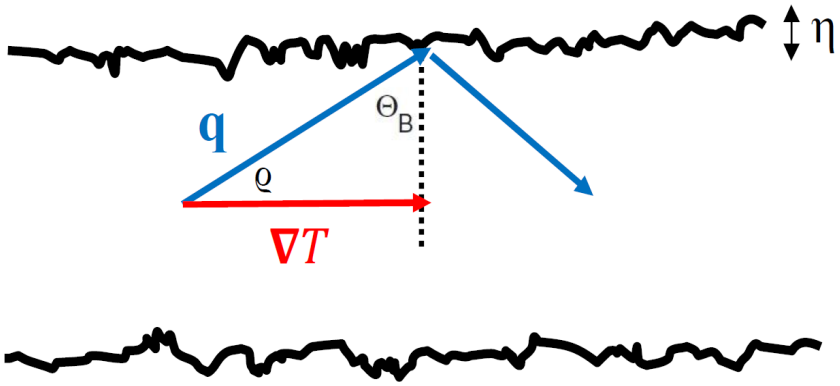

Figure 6.1: Schematic of graphene ribbon of width W, showing a phonon scattering from the rough edges. Θ_B is the angle between the normal to the surface and the wave vector of the incident phonon, ϱ is the angle between the temperature gradient direction and the phonon wave vector, and η is the edge roughness.

rms-thesis For in-plane (p = LA,TA) phonons in graphene, ω_p are frequency independent and given as follows

$$q(\omega_p) = \frac{\omega}{v_p}. \tag{6.12}$$

by substituting Eq.(6.12) into Eq.(6.11), we obtain

$$R(\omega_p) = \exp\left[-(2\omega_p \eta \sin \varrho/v_p)^2\right]. \tag{6.13}$$

and the relaxation time in Eq.(6.9) can be re-written as

$$\tau_{er,p}(\omega, \varrho) = \frac{W}{v_p} \frac{\exp\left(4\eta^2 \sin^2 \varrho/v_p^2\right) + 1}{\exp\left(4\eta^2 \sin^2 \varrho/v_p^2\right) - 1}. \tag{6.14}$$

The phonon relaxation time can be incorporated in the thermal conductivity calculation by integrating the variable ϱ and setting $x = \hbar\omega/k_B T$ as follows [21]

$$\tau_{er,p}(x, \varrho) = \int_0^{\pi} \mathrm{d}\varrho \, \frac{W}{v_p} \frac{\exp\left(g x^2 T^2 \sin^2 \varrho/v_p^2\right) + 1}{\exp\left(g x^2 T^2 \sin^2 \varrho/v_p^2\right) - 1} \times 2\cos^2 \varrho \sin \varrho, \tag{6.15}$$

where $g = 4\eta^2 k_B^2/\hbar^2$. If we put $y = \cos\varrho$, define $Z_p(y) = gx^2T^2(1-y^2)/2v_p^2$, and use the trigonometric identity, $\coth(x) = \frac{e^{2x}+1}{e^{2x}-1}$, then we can write

$$\tau_{er,p}(x) = 2\int_0^1 \mathrm{d}y\; y^2 \coth\, Z_p(y). \tag{6.16}$$

From Eq.(6.14) and Eq.(6.15), it is clear that the relaxation time is quite sensitive to the edge roughness and the temperature of the sample. The total phonon relaxation rate contributed from scattering of phonons for calculating the effect of edge roughness on thermal conductivity will be

$$\tau^{-1} = \tau_{\mathrm{er}}^{-1} + \tau_{\mathrm{pd}}^{-1} + \tau_{\mathrm{anh}}^{-1} \tag{6.17}$$

6.2.4 Effect of strain on phonon dispersion relations for graphene

The presence of strain, applied intentionally or unintentionally, can affect the thermal properties of graphene. Stress related change in the thermal conductivity of graphene can largely be related to changes in the phonon dispersion relation, velocity, and density of states. For studying strain-dependent thermal conductivity, the Boltzmann transport equation needs to include strain-dependent phonon dispersion relations which could be a daunting job. Alternatively, since mechanical strain is translated into modifications of crystal elastic constants, we will incorporate these modified values into the mathematical equations of phonon dispersion relations, density of states, and thermal conductivity to investigate the effect of tensile strain on the thermal properties of graphene and graphite.

Strain arises when a crystal is compressed or stretched out of equilibrium. Theoretically, the effect of strain could be studied by using the continuum theory of elasticity. Experimental measurements [22] indicate a linear relationship between applied pressure P up to 300 kbar and the in-plane lattice constant a for

graphite. From the results presented in Ref. [22], we have expressed $a = a_0 + r\ P$, with $a_0 = 2.462$ Å as the unstrained lattice constant of graphene and $r = 1.625 \times 10^{-4}$ Å/kbar for both positive and negative values of P. The strain ϵ is then defined as $\epsilon = (a - a_0)/a_0$. Within the elastic limit, we consider both positive and negative values of ϵ corresponding to positive and negative values of pressure P. Using the standard theory of free-standing membranes, de Andres *et al.* [23] studied the effect of strain on the dispersion curve for the flexural ZA modes in graphene (see Appendix E for details). For an isotropic strain, ϵ, the dispersion relation becomes

$$\omega_3^2 = b^2 q_a^4 + \frac{2}{\rho_{2\mathrm{D}}}(\lambda + \bar{\mu})\epsilon q^2, \tag{6.18}$$

where $\rho_{2\mathrm{D}}$ is the two-dimensional mass density, λ and $\bar{\mu}$ are the two-dimensional elastic Lamé coefficients for graphene. Following Refs. [23, 24], we have taken $\lambda = 2\,\mathrm{eV\AA}^{-2}$ and $\bar{\mu} = 10\,\mathrm{eV\AA}^{-2}$. Ignoring in-plane tension, the dispersion relation for the ZA branch becomes $\omega_3^2 = b^2(q_x^2 + q_y^2)^2 = b^2 q_a^4$ and this indeed is the first term in Eq. (6.3).

Under hydrostatic pressure, the elastic constants of graphite undergo a change in their stiffness values. This change will significantly affect the phonon propagation velocities. From the experimental results presented in Ref. [25], the relationship between pressure and elastic constants have been mathematically formulated polynomially as follows

$$\begin{aligned} C_{11} &= 1.06152 \times 10^{13} + 3.25738 \times 10^{10} P, \\ C_{12} &= 1.79782 \times 10^{12} + 9.95408 \times 10^{9} P, \\ C_{33} &= 3.65 \times 10^{11} + 1.11363 \times 10^{10} P, \\ C_{44} &= 4.25 \times 10^{10} + 1.22584 \times 10^{9} P, \end{aligned} \tag{6.19}$$

where C_{ij} are in units of $\mathrm{dyn/cm}^2$ and P in kbar.

As can be noticed in Eq.(3.6), the phonons velocity depends on the elastic constants of graphite and thus affected under pressure. The change in interlayer separation c in graphite with respect to pressure has been introduced in Ref. [26] and we have expressed an empirical formula as follows

$$\begin{aligned} c &= c_0 - 0.00217354P + 1.72863 \times 10^{-5}P^2 - 9.56297 \times 10^{-8}P^3 \\ &\quad +2.20551 \times^{-10} P^4, \end{aligned} \tag{6.20}$$

where c is in unit of cm and $c_0 = 3.3544 \times 10^{-8}\mathrm{cm}$ is the interlayer distance between graphite layers at atmospheric pressure. Based on the dependency of the elastic constants on the applied tensile strain/stress, the physical constants which in turn depend on these elastic constants will be become pressure-dependent accordingly and can be re-written as

$$v_{\mathrm{LA}}(P) = [C_{11}(P)/\rho]^{1/2}. \tag{6.21}$$

$$v_{\mathrm{TA}}(P) = \left[\frac{C_{11}(P) - C_{12}(P)}{2\rho}\right]^{1/2}. \tag{6.22}$$

$$\zeta(P) = \frac{C_{44}(P)}{\rho}. \tag{6.23}$$

$$\mu(P) = \sqrt{\frac{C_{33}(P)}{\rho c^2(P)}}. \tag{6.24}$$

$$\omega_z(P) = 2\left(\frac{C_{44}(P)}{\rho c^2(P)}\right)^{1/2}. \tag{6.25}$$

$$\omega_z'(P) = 2\left(\frac{C_{33}(P)}{\rho c^2(P)}\right)^{1/2}. \tag{6.26}$$

$$\{\omega_D\}_{\mathrm{LA,TA}}(P) = \sqrt{\frac{4\pi v_{\mathrm{LA,TA}}^2 N_A}{A_m} + \frac{\omega_z^2(P)}{2}}. \tag{6.27}$$

$$\omega_{D,\mathrm{ZA}}(P) = \frac{4\pi b N_A}{A_m}. \tag{6.28}$$

All the above equations are incorporated into the equations of phonon dispersion relations, density of states, specific heat, and thermal conductivity to investigate the changes in the thermal properties of graphene and graphite under mechanical stretching and compression.

6.3 Results and analysis

6.3.1 Phonon dispersion curves, velocity, and density of states

The application of compression is to increase the in-plane frequencies $\omega(\mathrm{LA})$ and $\omega(\mathrm{TA})$ but decrease the out-of-plane frequency $\omega(\mathrm{ZA})$. It was found that $\omega(\mathrm{ZA})$ becomes imaginary with increased compression, see Fig. 6.2, indicating instability of the system.

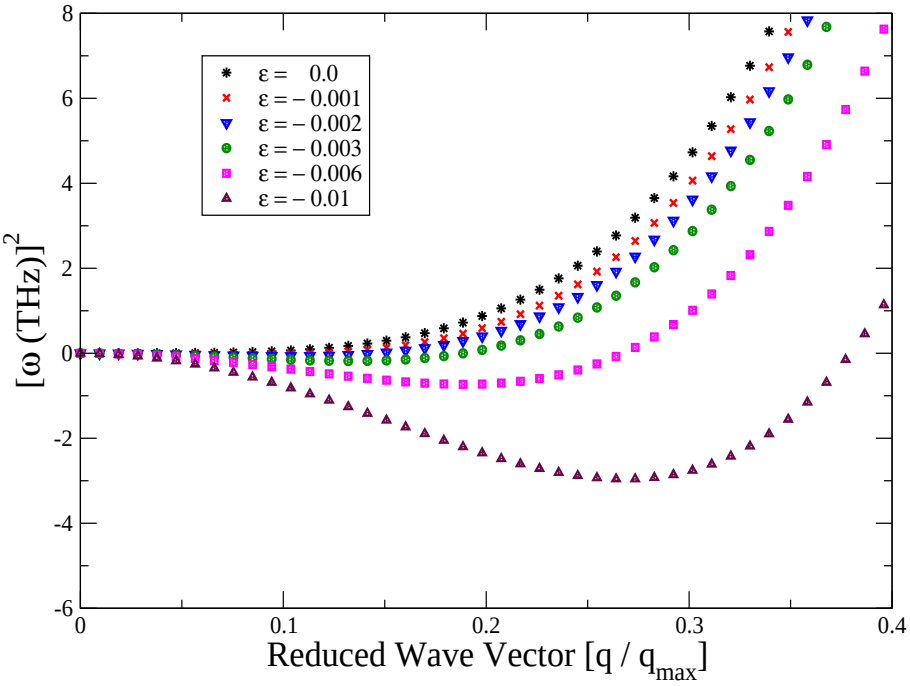

Figure 6.2: Dispersion relation for the out-of-plane phonon modes in graphene under compressive strain.

Under tensile strain $\omega(\mathrm{LA})$ and $\omega(\mathrm{TA})$ decrease but $\omega(\mathrm{ZA})$ increases, as seen in Fig. 6.3. These can be easily understood. Stretching makes the C-C bonds weaker and the in-plane modes softer, and the "dangling bonds" stronger and the out-of-plane mode harder. The change computed for $\omega(\mathrm{LA})$ and $\omega(\mathrm{TA})$ is larger than that for $\omega(\mathrm{ZA})$. The velocities of the LA and TA modes decrease as the strain

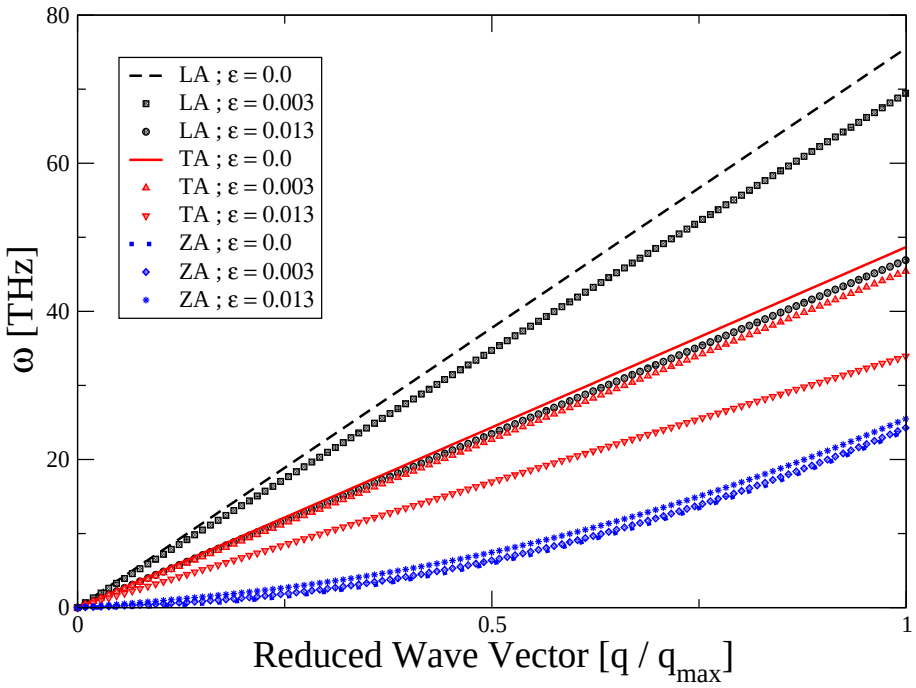

Figure 6.3: Dispersion relations for graphene under tensile strain.

increases. As can be seen in Fig. 6.4, we find that the velocity of the LA mode becomes smaller than that of the TA mode for ϵ larger than 0.019. This is consistent with Eq.(6.19), Eq.(6.21), and Eq.(6.22).

The velocities of the ZA modes of frequencies higher than approximately 2.5 THz also decrease with increase in tension. However, the velocities of this mode for frequencies smaller than 2.5 THz show a reverse trend, and of larger magnitude, as shown in Fig. 6.5. We note that for $\epsilon = 0.013$ the velocity changes are 38%, 31% and 8% for the LA, TA, and high-frequency ZA modes, respectively.

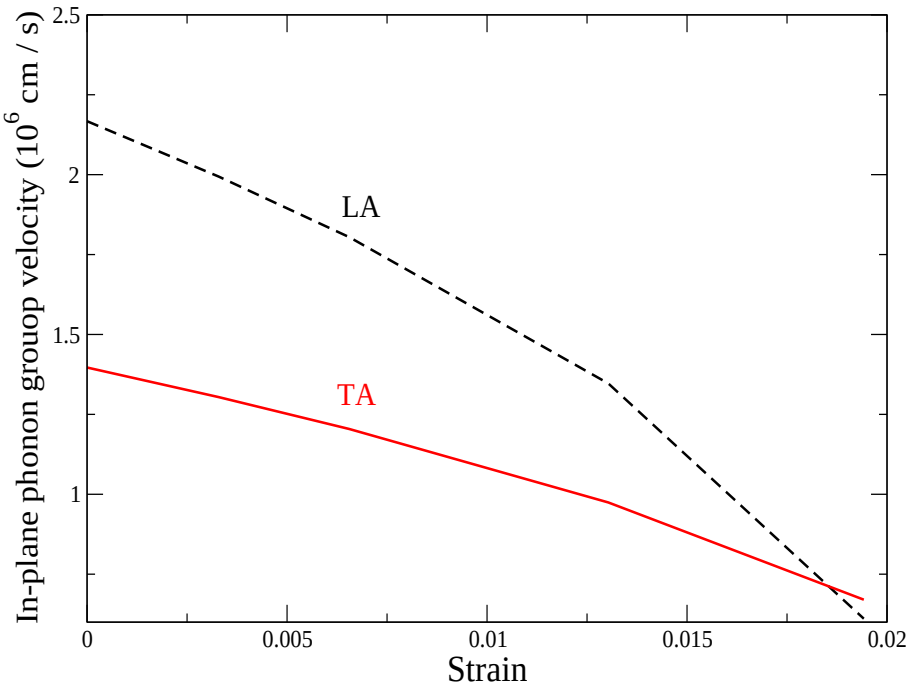

Figure 6.4: Velocity changes for the in-plane phonon modes under strain.

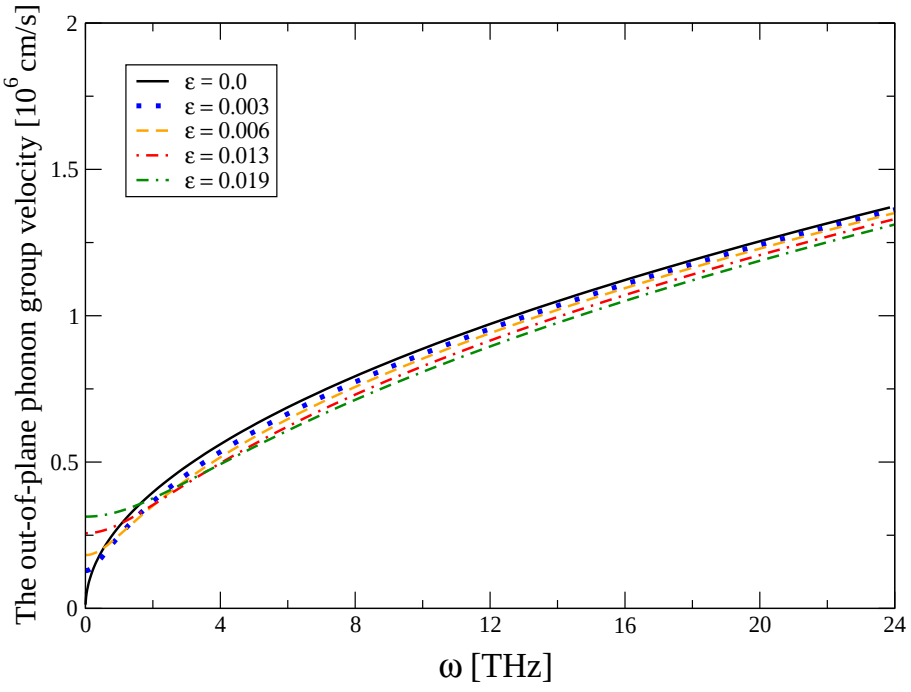

Figure 6.5: Velocity changes for the out-of-plane phonon modes under strain.

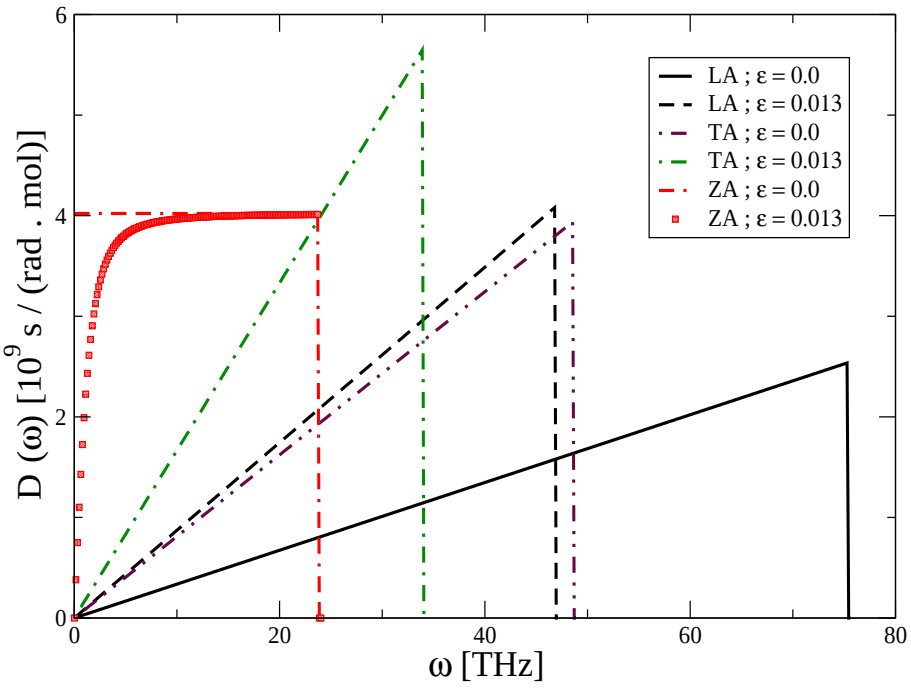

Figure 6.6: Graphene density of states under tensile strain.

From Fig. 6.6, we notice that under tensile strain the density of states of the in-plane modes (LA and TA) increases, while it decreases for the out-of-plane modes (ZA). The change in the density of states for LA and TA phonons under tensile strain is contributed by two factors: reduction in their spectral range and reduction in their group velocity. In contrast, the vibrational spectrum of the ZA phonons increases very slightly (see Fig.6.3) and only a slight decrease in its group velocity (see Fig.6.5). Actually, the density of states for the ZA branch acquires a dispersive behavior at low frequencies: starting from zero for zero frequency, it rapidly reaches the maximum value obtained for the unstrained case above about 15 THz. Below about 5 THz the density of states for the ZA modes is heavily quenched.

6.3.2 Specific heat

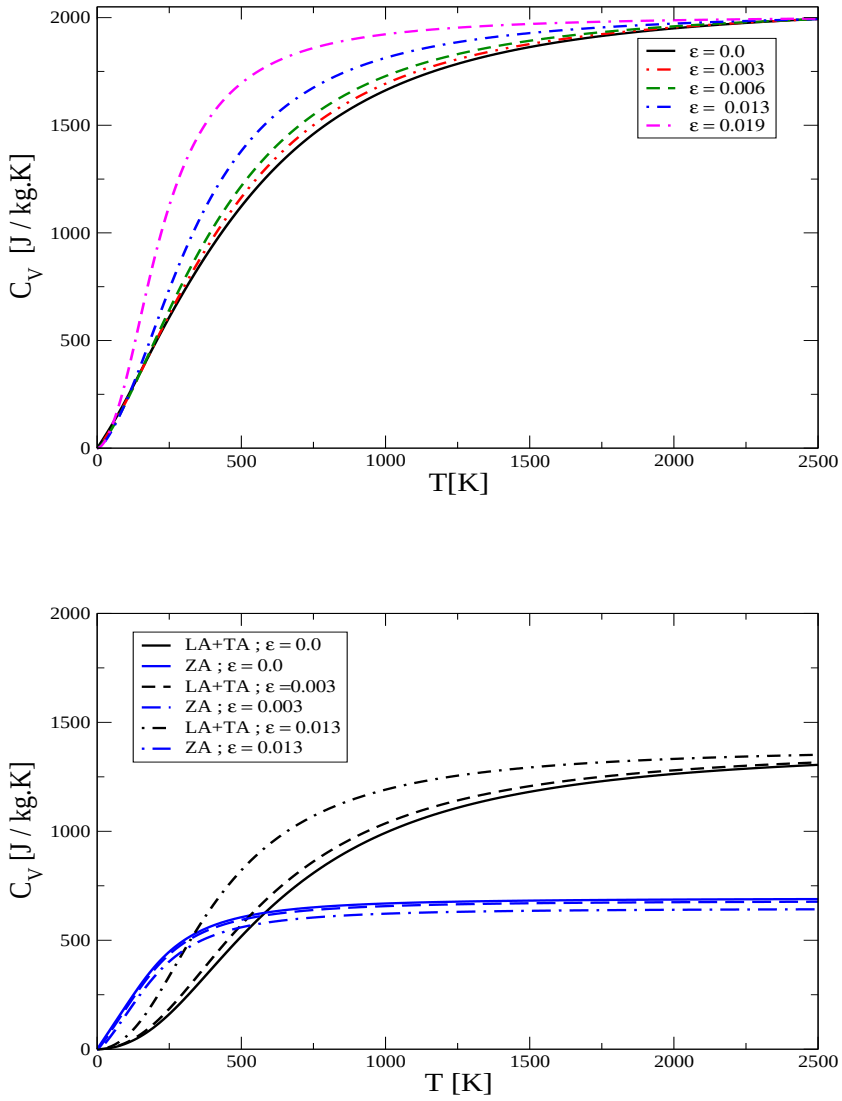

Figure 6.7: Effect of tensile strain on graphene specific heat for a wide range of temperatures: The upper panel shows the total specific heat, the lower panel shows the contributions from in-plane and out-of-plane branches.

The specific heat is altered in the presence of tensile stain: whereas the contribution from the LA and TA modes increases, the contribution from the ZA modes decreases. At a given temperature, the combined increase from the LA and TA modes is larger than the decreases from the ZA modes. The overall effect of strain is to increase the specific heat. These features are shown in Fig. 6.7.

The overall increase of $\mathrm{C_v}$ with temperature has also been noted in another theoretical study [13]. Our computed results reveal that the effect of strain is largest in the intermediate temperature range (e.g., 16% at 200 K for $\epsilon = 0.013$), becoming very small at both low and high temperatures (e.g., 4% at 100 K and 1% at 2000 K for $\epsilon = 0.013$). These strain-related changes in different temperature ranges arise from the joint effect of related changes in the dispersion relations (ω vs q), density of states [$D(\omega)$], and the phonon distribution function [$\bar{n}(\omega, T)$].

6.3.3 Thermal conductivity

6.3.3.1 Unstrained graphene

Figure 6.8 shows the thermal conductivity results for graphene, graphite basal planes, and along the graphite c-axis. The present theoretical results are compared with the experimental measurements reported by Chen *et al.* [27], who used a sample of a monolayer graphene grown by the chemical vapor deposition (CVD) on copper and then suspended over holes with different diameters ranging $2.9 - 9.7$ μm.

For graphene, the results of phonon conductivity calculations were made for a stand-alone sample of size $L_a = 2.9$ μm and a consideration of $A_d = 4.5 \times 10^{-4}$, where $A_d = c_d(\Delta M/M)^2$. In order to fit theory with the experimental data for the suspended sample, we used the following parameters: $B_U = 3.18 \times 10^{-25}$ sK^{-3},

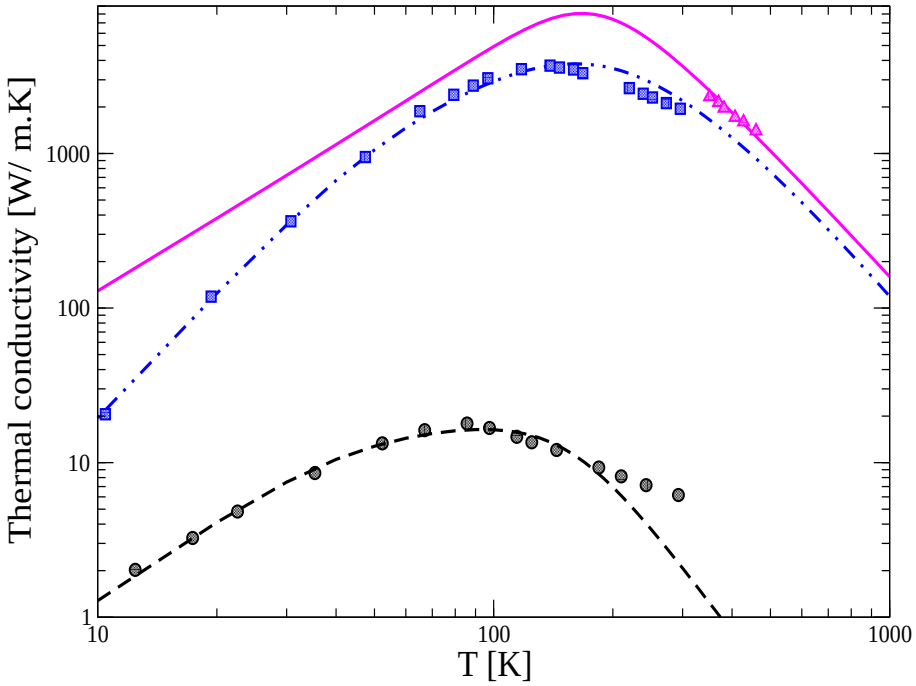

Figure 6.8: Thermal conductivity of graphene (solid line), graphite basal plane (dotted line) and graphite c axis (dashed line), compared with experimental measurements: graphene (up triangles) [27]; graphite in-plane (squares) [28]; graphite c-axis (circles) [29].

and $B_N = 2.12 \times 10^{-25}$ sK^{-3}. For matching theory with experiment for the basal plane conductivity in graphite [28], we considered boundary length $L_a = 8.7$ μm and $A_d = 4.5 \times 10^{-4}$, while keeping the parameters B_U and B_N the same as for graphene.

The conductivity along the c-axis was computed with the consideration of the boundary length $L_c = 0.1$ μm and $A_d = 4.5 \times 10^{-4}$. Due to the presence of strong intraplanar bonds in graphite basal planes and weak interplanar bonds along the c-axis, we had to choose stronger anharmonic interaction parameters ($B_U = 2.23 \times 10^{-22}$ sK^{-3}, and $B_N = 1.48 \times 10^{-22}$ sK^{-3}) in order to match the experimental data for the c-axis thermal conductivity in graphite [29]. Such changes

in the choice for the B_U and B_N parameters are supported by the fact that for graphite the in-plane Grüneisen parameter is smaller than that of the out-of-plane, see Ref. [30].

The highly anisotropic behaviour of the lattice thermal conductivity of graphite is consistent with its anisotropic nature of bonding. At room temperature, the thermal conductivity along the graphite c-axis is 2 W/m.K, graphite basal planes is 2195 W/m.K, and 3541 W/m.K for graphene. The maximum thermal conductivity values computed in the present paper for graphene, graphite basal plane ($K_{xx} = K_{yy} = K_a$), and graphite c-axis (K_{zz}) are 7202 W/m.K at 170 K, 3808 K at 160 K, and 16 W/m.K at 90 K, respectively. It is obvious that at room temperature, the thermal conductivity of graphite along the c-axis is two orders of magnitude smaller than that calculated for graphene. We note that at low temperatures (up to 40 K), the thermal conductivity varies as $T^{1.6}$, $T^{2.4}$, and $T^{1.4}$ for graphene, graphite basal planes, and along the graphite c-axis, respectively. These clear differences in the temperature variation indicate the quasi- two-dimensional, quasi-three-dimensional, and quasi-one-dimensional nature of the thermal conductivity of graphene, graphite basal plane, and along the graphite c-axis, respectively.

Apart from the presence of point defects, it is important also to consider the effect of isotopes, present naturally or introduced intentionally, on the thermal conductivity of graphene. A detailed experimental study of the thermal conductivity of isotopically modified graphene containing various percentages of ^{13}C has recently been presented by Chen *et al.* [31]. Figure 6.9 shows the conductivity results for graphene containing two concentrations of the ^{13}C isotopes: 1.1% and 50%. We used 2.9 μm for the effective boundary length. Our theoretical results are in agreement with the experimental measurements made in the temperature range 300–600 K. It is clear from Fig. 6.9 that the isotopic effect on the conductiv-

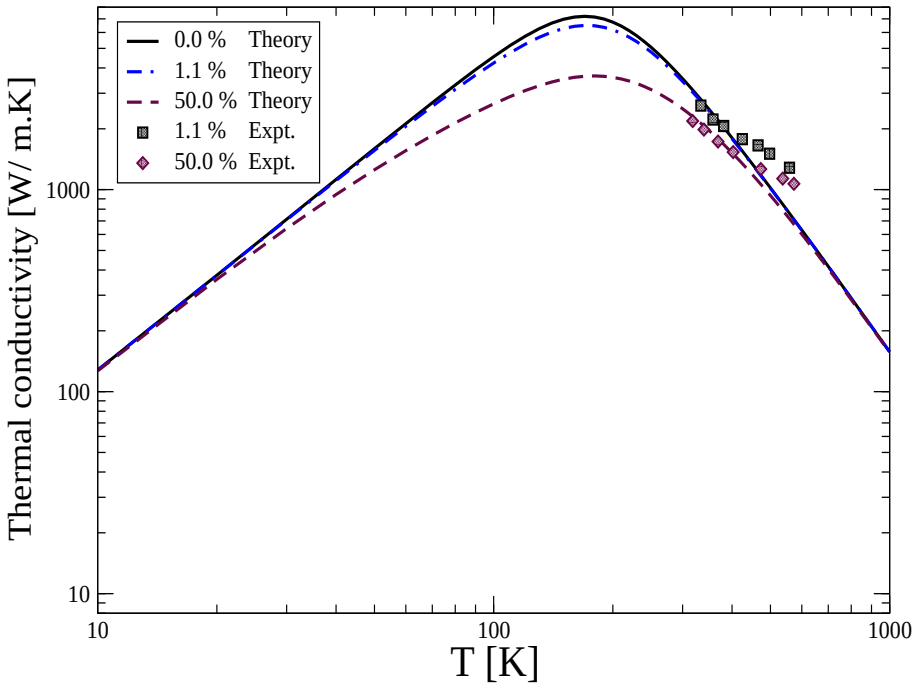

Figure 6.9: The thermal conductivity of graphene with different concentrations of ^{13}C isotopes. The symbols represent the experimental measurements from Ref. [31].

ity is significant in the low- temperature range 50–300 K. Near the conductivity maximum, around 200 K, the conductivity drops by 15% and 49% for the isotopic concentrations 1.1% and 50%, respectively.

6.3.3.2 Strained graphene

It has been reported that the thermal conductivity of graphene is very sensitive to tensile strain [32, 33]. Our work shows that the effect of tensile strain on the conductivity depends on the purity (i.e., level of defects) of graphene. To clarify this, we have computed the conductivity of graphene with two hugely different levels of defect concentration.

Figure 6.10 shows the results for strained graphene with almost no defect (i.e.,

with $A_d = 9 \times 10^{-6}$). Our calculations reveal that the strain-related change in the conductivity is temperature dependent. In general, below room temperature we obtain both reduction as well as increase in the conductivity, depending on the amount of strain. Above room temperature, the conductivity decreases for any magnitude of strain. In particular, our calculations reveal that the conductivity *decreases* with tensile strain for ϵ values of 0.003 and 0.006, but *increases* for ϵ values of 0.013 and 0.019. At 170 K, the conductivity decreases by 2.7% for $\epsilon = 0.006$ and increases by 8.8% for $\epsilon = 0.019$. At 600 K, the conductivity decreases by 11% and 16% when ϵ is set at 0.006 and 0.019, respectively.

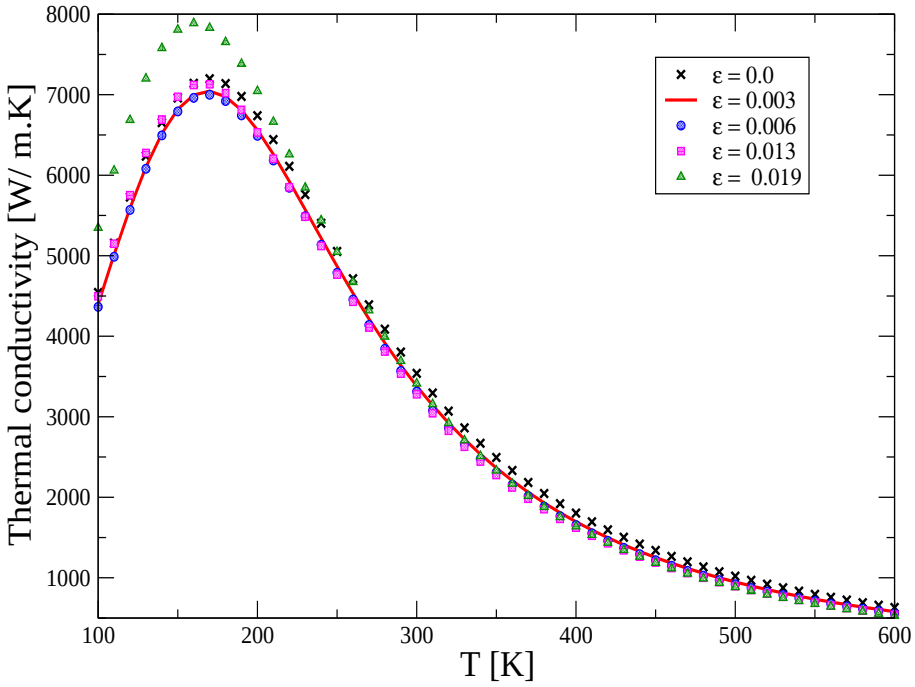

Figure 6.10: Thermal conductivity of defect-free graphene under tensile strain.

In the presence of finite amounts of defects, the effect of tensile strain is to reduce the thermal conductivity at all temperatures. This can be seen from the results

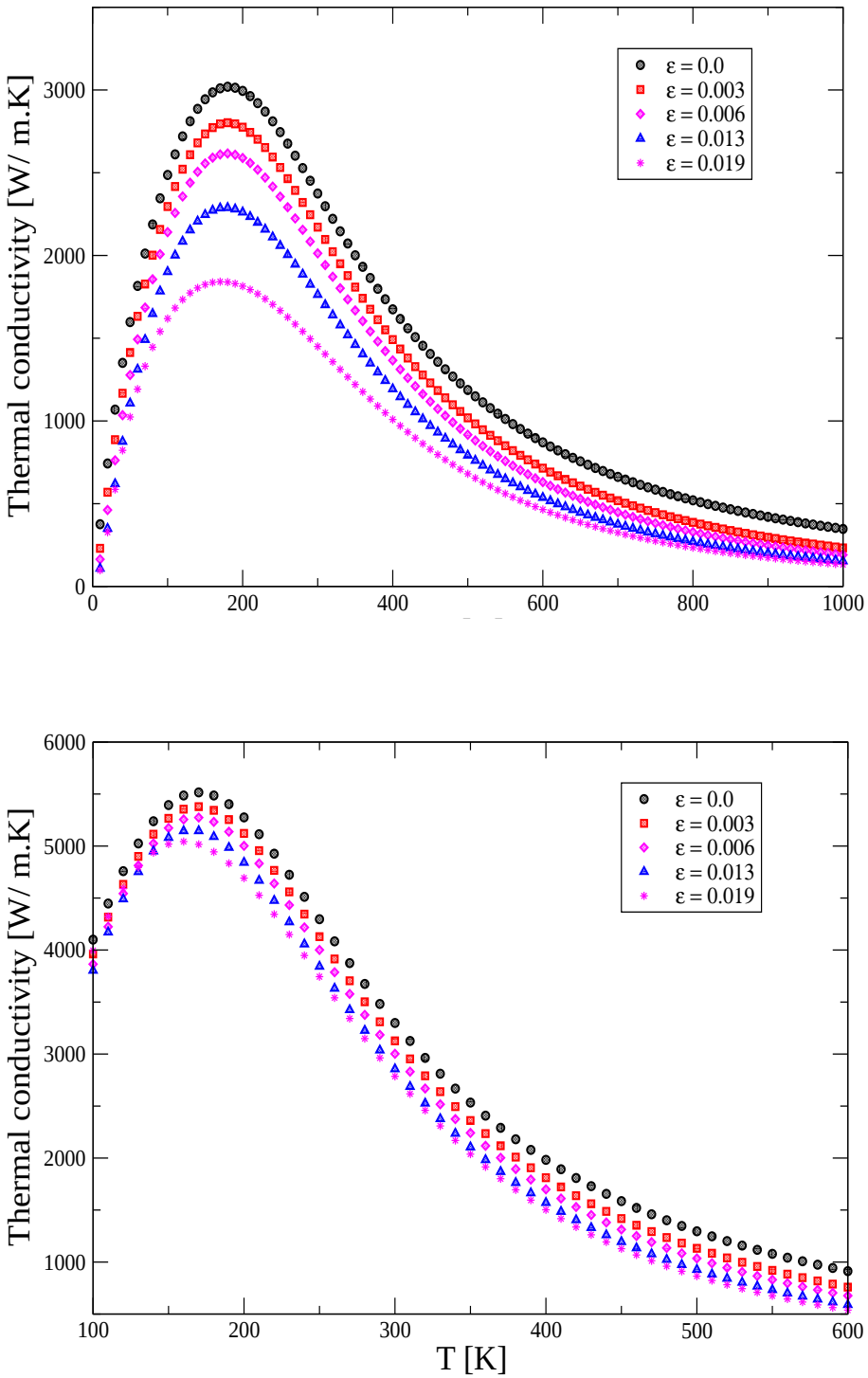

Figure 6.11: Effect of tensile strain on the thermal conductivity of graphene with different amounts of defects. The results shown in the lower and upper panels correspond to $A_d = 5.4 \times 10^{-5}$ and $A_d = 9 \times 10^{-4}$, respectively.

presented in Fig. 6.11 for two defect concentrations: $A_d = 5.4 \times 10^{-5}$ and $A_d = 9 \times 10^{-4}$. The decrease in the conductivity for $A_d = 9 \times 10^{-4}$ and $\epsilon = 0.019$ is 39% at 170 K and 47% at 600 K. The decrease in the conductivity for $A_d = 5.4 \times 10^{-5}$ and $\epsilon = 0.019$ is 9% at 170 K and 41% at 600 K. These results clearly suggest that reduction in the conductivity becomes more pronounced for graphene with larger concentration of defects.

6.3.4 Compression along the graphite c-axis

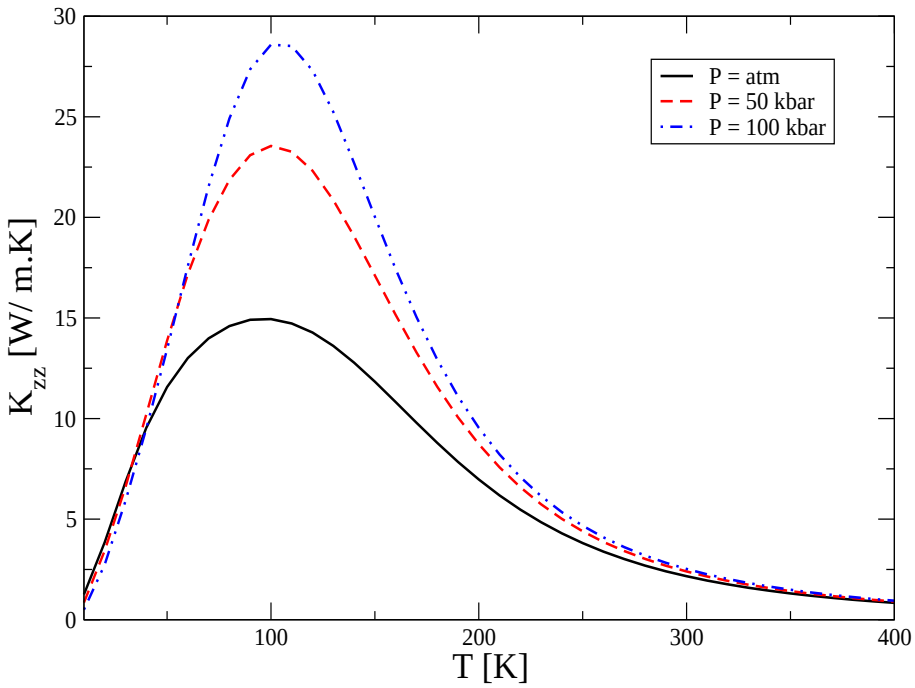

Figure 6.12: Thermal conductivity of along graphite c-axis under compression.

Figure 6.12 shows the effect of pressure (compression) applied along the graphite c-axis. Due to the applied pressure, the interlayer distance (c) or bond length decreases, see Fig. 6.13, and thus C_{33} increase. This pressure causes a decrease of the structural anisotropy (c/a) and enhance the phonon propagation parallel to the

c-axis of graphite. At $T = 100$ K and $P = 100$ kbar, K_{zz} becomes approximately two times larger than its value at ambient pressure. It can be noticed that at relatively low temperatures, the K_{zz} decreases slowly as compression increases and then starts to increase. This can be attributed to two reasons. First, the contribution of the out-of-plane mode along the c-axis is reduced as its velocity $(v_3)_z$ is reduced more than the in-plane modes under compression. As temperature increases, the contributions from the in-plane modes will overcome this reduction and K_{zz} will increase. Second, the expansion along the c-axis as a result of temperature increase and the bending modulus have been ignored in this work. It can be concluded that increasing the thermal conductivity along the graphite c-axis can be achieved by hydrostatic compression.

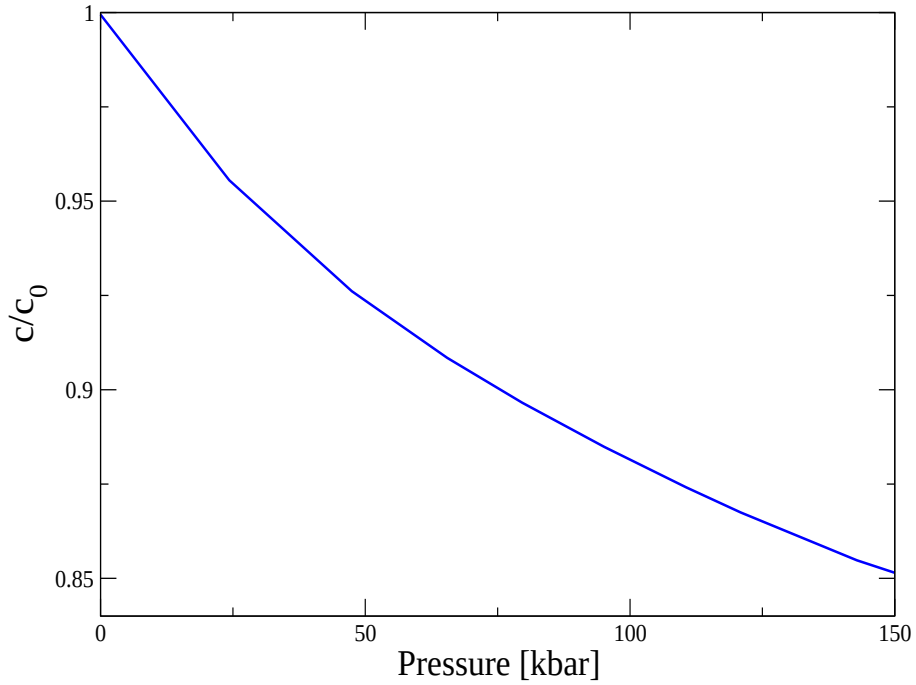

Figure 6.13: Relative interlayer distance c/c_0 of graphite as a function of compression. Reported from [26].

6.3.5 Edge roughness scattering

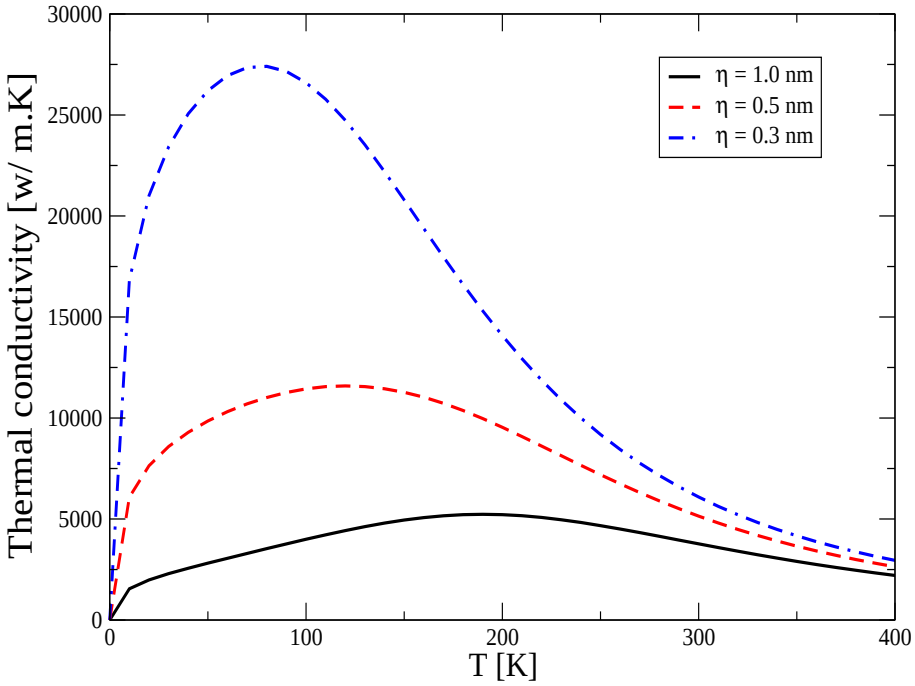

Figure 6.14: Thermal conductivity results for graphene ribbons of $L = 2.9\mu$m with different values of edge roughness η.

Figure 6.14 shows the significant effect of edge roughness on graphene thermal conductivity. It is noticeable that an increase in the roughness of graphene ribbon edges results in a decrease in graphene's ability to conduct heat. This decrease is due to the phonon scattering from the rough edges of the sample. At $T \simeq 100$ K, the thermal conductivity peak is shifted up one order of magnitude from approximately 4000 W/m.K to 25000 W/m.K when η reduced from 1.0 nm to 0.3 nm. Also, the gradual disappearing of the peak as η increases reflects the strong role of η on phonon scatting. As expected, at high temperatures, the impact of edge roughness on thermal conductivity is negligible and the phonon scattering from edge roughness becomes weak.

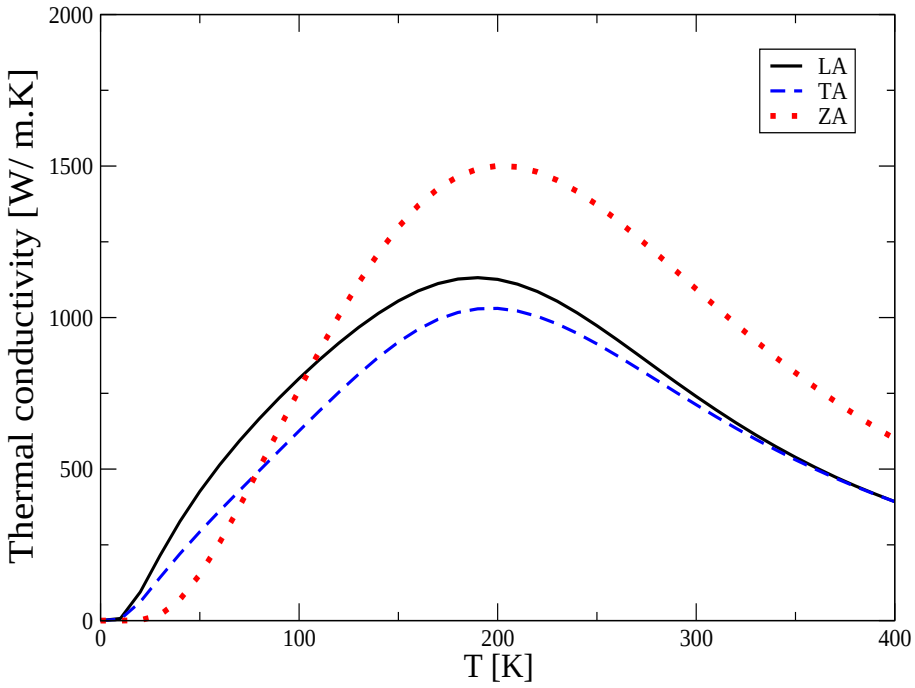

Figure 6.15: Graphene ribbon with edge roughness $\eta = 0.8$ nm and $L = 2.9\mu$m, showing contributions from individual phonon branches.

The contribution from the ZA phonons to the thermal conductivity of graphene is larger than both LA and TA ones at all temperatures, as seen in section 5.3. However, as η increases, the ZA contribution becomes smaller than that from LA and TA phonons only at low temperatures as shown in Fig.6.15. This could be attributed to the assumption that ZA phonons are most likely to be scattered from the edge roughness than the in-plane modes at low temperatures. At high temperatures, the contribution from the ZA phonons start to increase and becomes dominant over the contribution from in-plane phonons. This order of contribution at low temperatures in this work is exactly the opposite of that obtained by Aksamija *et al* [5], where they studied the thermal conductivity of GNRs based on solving the BTE with the full phonon dispersion. In their calculations, high temperature expression for Umklapp phonon scattering is used and they performed

more specific treatment of armchair and zigzag edges, we believe that these are the reasons for conflicting findings.

6.4 Summary

The thermal conductivity in graphene, graphite basal planes, and along the graphite c-axis has been calculated. The theory successfully explains the experimental measurements for these systems. For the considered samples, we find that throughout the temperature range, the conductivity of graphene is larger than that in the basal plane of graphite. In order to explain the huge reduction in the conductivity of graphite along its c-axis, we had to assume much stronger anharmonic interaction parameters, consistent with the fact that the in-plane Grüneisen parameter is smaller than that of the out-of-plane parameter. At low temperatures (up to 40 K), the thermal conductivity varies as $T^{1.6}$, $T^{2.4}$, and $T^{1.4}$ for graphene, graphite basal planes, and along the graphite c-axis, respectively. Significant isotopic effect on the conductivity of graphene was found in the temperature range $50-300$ K, with the maximum reduction at 200 K of 49% for 50% ^{13}C.

The overall effect of strain is to increase the specific heat. It has been shown that the thermal conductivity of graphene can be significantly tuned with the combination of defect concentration and tensile strain. For pure graphene, in the presence of tensile strain the conductivity increases at low temperature, and decreases above room temperature. For graphene with point defects, the effect of strain is to reduce the conductivity at all temperatures. The decrease in the conductivity for the defect concentration $A_d = 9 \times 10^{-4}$ and strain parameter $\epsilon = 0.019$ is 39% at 170 K and 47% at 600 K. Applying compressive pressure along graphite c-axis leads to an improvement of the thermal conductivity along that axis. Edges roughness in graphene ribbons play an important role in the heat

conduction mechanism. Our calculations suggest that at 100 K, the conductivity value of 25000 W/m.K for roughness parameter $\eta = 0.3$ nm decreases to 4000 W/m.K when $\eta = 1.0$ nm.

Bibliography

[1] W. J. de Haas and T. Biermasz, Physica **2**, 673 (1935) ; **4**, 754 (1937) ; **5**, 47 (1938).

[2] H. B. Casimir, Physica **5**, 495 (1938).

[3] R. Berman, F. E. Simon, and J. M. Ziman, Proc. R. Soc. A 220, **171** (1953).

[4] J. Hu, X. Ruan, and Y. P. Chen, Nano Lett. **9**, 2730 (2009).

[5] Z. Aksamija, and I. Knezevic, Appl. Phys. Lett. **98**, 141919 (2011).

[6] Y. Shen, G. Xie, X. Wei, K. Zhang, M. Tang, J. Zhong, G. Zhang, and Y. Zhang, J. Appl. Phys. **115**, 063507 (2014).

[7] B. T. Kelly, *Physics of Graphite* (Applied Science Publishers, London and New Jersey, 1981).

[8] P. W. Bridgman, Am. J. Sci. **7**, 81 (1924).

[9] R. G. Ross, P. Anderson, B. Sundqvist, and G. Bäckström, Rep. Prog. Phys. **47**, 1347 (1984).

[10] X. Li, K. Maute, M. L. Dunn, and R. Yang, Phys. Rev. B. **81**, 245318 (2010).

[11] R. C. Picu, T. Borca-Tasciuc, and M. C. Pavel, J. Appl. Phys. **93**, 3535 (2003).

[12] J. Zhang, X. He, L. Yang, G. Wu, J. Sha, C. Hou, C. Yin, A. Pan, Z. Li, and Y. Liu, Sensors, **13**, 9388 (2013).

[13] F. Ma, H. B. Zheng, Y. J. Sun, D. Yang, K. W. Xu, and P. K. Chu, Appl. Phys. Lett. **101**, 111904 (2012).

[14] X. Zhai, and G. Jin, Europhys. Lett. 96, 16002 (2011).

[15] M. Hanfland, H. Beister, and K. Syassen, Phys. Rev. B **39**, 12598 (1989).

[16] A. S. Ivanov, I. N. Goncharenko, V. A. Somenkov, and M. Braden, High Pressure Res. **14**, 145 (1995).

[17] B. T. Kelly , Carbon **5**, 247 (1967).

[18] B. T. Kelly , Carbon **6**, 71 (1968).

[19] P. G. Klemens and D. F. Pedraza, Carbon, **32**, 735 (1994).

[20] J. Ziman, *Electrons and Phonons: The Theory of Transport Phenomena in Solids* (Oxford University Press, New York, 1960).

[21] D. P. Singh, and Y. P. Joshi, Phys. Rev. B **19**, 3133 (1979).

[22] Y. Wang, J. E. Panzik, B. Kiefer, and K. K. M. Lee, Sci. Rep. **2**, 520 (2012).

[23] P. L. de Andres, F. Guinea, and M. I. Katsnelson, Phys. Rev. B **86**, 144103 (2012).

[24] K. V. Zakharchenko, M. I. Katsnelson, and A. Fasolino, Phys. Rev. Lett. **102**, 046808

[25] W. B. Gauster and I. J. Fritz, J. Appl. Phys. **45**, 3309 (1974).

[26] T. Yagi, W. Utsumi, M. Yamakata, T. Kikegawa, and O. Shimomura, Phys. Rev. B **46**, 6031 (1992). (2009).

[27] S. Chen, A. L. Moore, W. Cai, J. W. Suk, J. An, C. Mishra, C. Amos. C. W. Magnuson, J. Kang, L. Shi, and R. S. Ruff, ACS Nano **5**, 321 (2011).

[28] A. DE Combarieu, J. Physique, **28**, 951 (1967).

[29] B. Dreyfus and R. Maynard, J. Physique, **28**, 955 (1967).

[30] D. T. Morelli and G. A. Slack, *High Thermal Conductivity Materials* (Springer Science/Business Media, New York, 2006), Chap. 2.

[31] S. Chen, Q. Wu, C. Mishra, J. Kang, H. Zhang, K. Cho, W. Cai, A. A. Balandin, and R. S. Ruoff, Nature (London) **11**, 203 (2012).

[32] N. Wei, L. Xu, H. Wang, and J. Zheng, Nanotechnology **22**, 105705 (2011).

[33] D. L. Nika and A. A. Balandin, J. Phys.: Condens. Matter **24**, 233203 (2012).

Chapter 7

Evolution of Thermal Properties From Graphene to Graphite

7.1 Introduction

It is remarkable that compared to most layered systems, fabrication of single-layer graphene (SLG), bi-layer graphene (BLG), tri-layer graphene (TLG), and few-layer graphene (FLG) can be achieved in a controlled manner [1]. This strongly suggests that the FLG systems can be used to understand the fundamental mechanisms and in achieving controlled alteration of thermal conductivity along and perpendicular to the growth direction. In particular, it would be interesting to ascertain the minimum amount of thermal conductivity established when a BLG is formed.

Generally, the intrinsic ability of a material to conduct heat is altered as its dimensionality changes from two-dimensional (2D) to three-dimensional (3D). Lateral (in-plane) thermal conductivity in conventional semiconductor thin films tends to decrease with decreasing thickness. This is due to the domination of the boundary phonon scattering rate [2]. However, an opposite dependence is observed

in FLG where the thermal conductivity is reduced as the number of layers increases [3, 4, 5]. As graphite is composed of multilayer graphene, it is natural to think that studying thermal properties of FLG will elucidate how the thermal conductivity and specific heat of graphene evolve into graphite-like results with increasing number of layers.

The evolution of heat conduction from graphene to bulk graphite has been addressed experimentally by Ghosh *et al.* [3]. In their study, the number of graphene layers was determined by micro-Raman spectroscopy and the measurements of thermal conductivity were performed using a steady-state optical technique. They attributed the reduction in thermal conductivity of FLG to the increase in the number of phonon states available for Umklapp scattering.

Singh *et al.* [4] used linearised BTE and perturbation theory to investigate the thermal conductivity of FLG ($1-4$ layers). They noted that there is a reduction in the thermal conductivity as the number of graphene layers increases. In addition, they concluded that the interplanar interactions create many conducting channels for phonons scattering.

Many simulations based on non-equilibrium molecular dynamics (NEMD) are performed by Wei *et al.* [5] to study thermal conductivities of a single and multilayer graphene. It has been found that the in-plane thermal conductivity of multilayer graphene is reduced as the number of graphene layers increases, and the thermal conductivity of a monolayer graphene at room temperature is around $870\ \mathrm{W/m.K}$. They concluded that the interaction between neighbouring graphene layers imposes resistance to the free vibration of the carbon atoms. Thus, this will lead to a degradation of the phonon transport in a multilayer graphene.

In this work, specific heat and the lattice thermal conductivity tensor of FLG are calculated.

7.2 Theory

The FLG and graphite systems are considered as an assembly of equally spaced elastic layers with compressional and shearing couplings between adjacent layers. According to the theory of elasticity [6], the strength of the interlayer coupling in layered materials increases as the number of layers increases. Two elastic constants, C_{33} and C_{44}, are used to describe the compressional and shearing couplings, respectively. These elastic constants are sensitive to the number of graphene layers, and any change in their values will affect the Debye-like cut-off frequencies and thus the phonon density-of-states. We adopt a convenient approach, within the semicontinuum treatment, to evaluate the effect of C_{33} and C_{44} in changing the Debye-like cut-off frequencies and thus on thermal properties of FLG as the number of layers increases. Only acoustic phonon modes are considered in our calculations: in-plane longitudinal mode LA, in-plane transverse mode TA, and out-of-plane mode ZA.

The total phonon relaxation rate can be expressed as in Eq.(5.14). In order to deal with the in-plane and cross-plane (i.e. along the c-axis) conductivity components we need to use two sample dimensions: an in-plane length L_a and a cross-plane length L_c. Accordingly, there will two different expressions for boundary scattering as expressed in Eq.(6.8). The frequencies ω_z and ω'_z which are directly related to the shearing (C_{44}) and coupling (C_{33}) elastic constants can be seen in Eq.(4.20) and Eq.(4.21).

For graphite, the binding energy between adjacent layers is relatively weak com-

pared to strong binding energy within the layers. The potential energy of two interacting rigid layers separated by a distance c is usually determined using the standard $12-6$ Lennard-Jones potential. Usually, the parameters in that potential are employed for describing the van der Waals potential between graphene sheets per atom, which are fitted to reproduce the interlayer distance and the elastic constant C_{33} for graphite [7, 8]. The value of C_{44} could be attained experimentally. A simple alternative to obtain values of C_{33} and C_{44} as a function of the number of layers in FLG will be employed.

The shear-mode frequency ω_z for FLG sheets as a function of the number of layers was measured by Tan *et al.*[9] using Raman spectroscopy (see Appendix F). The lower cut-off out-of-plane frequency ω_z' for SLG, BLG, and TLG sheets are obtained from Ref. [10]. Using suitable fit of these data, the values of C_{33} and C_{44} for FLG of different number of layers with the help of Eq.(4.20) and Eq.(4.21) can be determined. The data for ω_z was fitted to the form

$$\omega_z = I \exp[a_1 + (a_2/(n + a_3))], \tag{7.1}$$

where n is the number of layers, and I, a_1, a_2, and a_3 as parameters fitted to values 1.01, 0.255, -0.256, and -1.257 respectively. The frequency ω_z' was considered in the form

$$\omega_z' = R_1/[1 + \exp(R_2 - nR_3)], \tag{7.2}$$

where R_1, R_2, and R_3 as parameters fitted to values 3.819, 0.827, and 0.6234, respectively.

7.3 Results and analysis

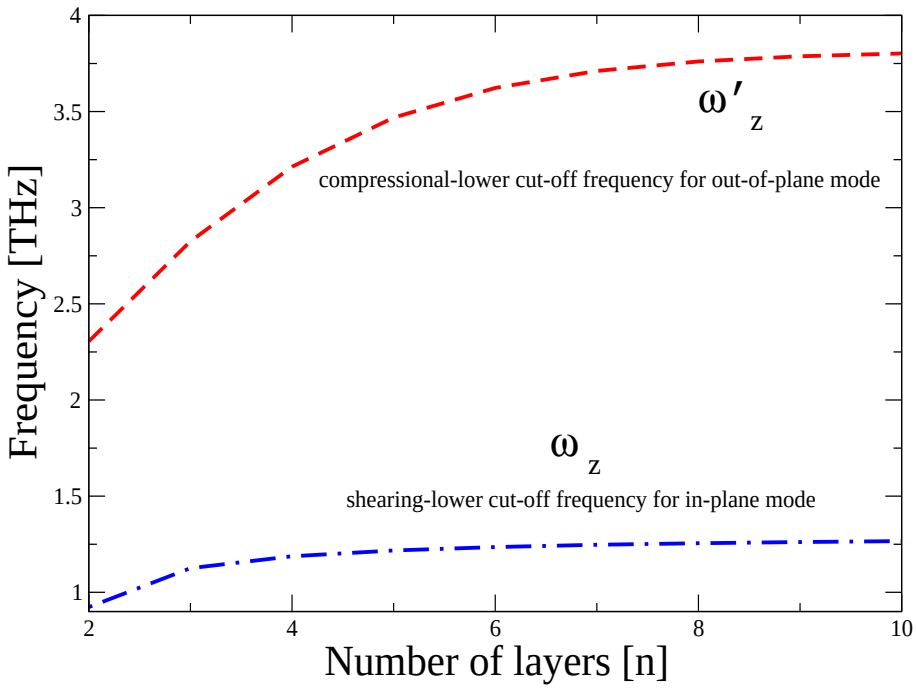

Figure 7.1: Variation of lower cut-off frequencies ω_z and ω_z' with the number of graphene atomic layers.

From Fig. 7.1, it can be noticed that both ω_z and ω_z' have fully saturated to the graphite values for $n \simeq 10$. However, ω_z saturates more rapidly than ω_z'. Table 7.1 lists the values of ω_z and ω_z' as a function of the number of layers. These values have been used to evaluate the specific heat and thermal conductivity of FLG.

Figure 7.2 shows the variation of specific heat C_v with temperature for multilayer graphene sheets and bulk graphite. For SLG there are no shearing and compressional couplings between layers, which means that $C_{33} \approx 0$, $C_{44} \approx 0$ and hence $\omega_z \rightarrow 0$ and $\omega_z' \rightarrow 0$. At low temperatures (< 60 K), a large difference can be seen between the specific heat of SLG and BLG sheets. It can be interpreted to arise

Table 7.1: The shear-mode and out-of-plane vibrational mode frequencies ω_z and ω'_z, and the corresponding shearing and compressional elastic constants C_{44} and C_{33}, as a function of layers in FLG.

Number of layers (n)	ω_z (THz)	ω'_z (THz)	C_{33} (dyn/cm^2)	C_{44} (dyn/cm^2)
2	0.923	2.305	1.337×10^{11}	0.214×10^{11}
3	1.125	2.825	2.009×10^{11}	0.319×10^{11}
4	1.187	3.213	2.6×10^{11}	0.355×10^{11}
6	1.235	3.622	3.304×10^{11}	0.384×10^{11}
10	1.266	3.802	3.639×10^{11}	0.403×10^{11}

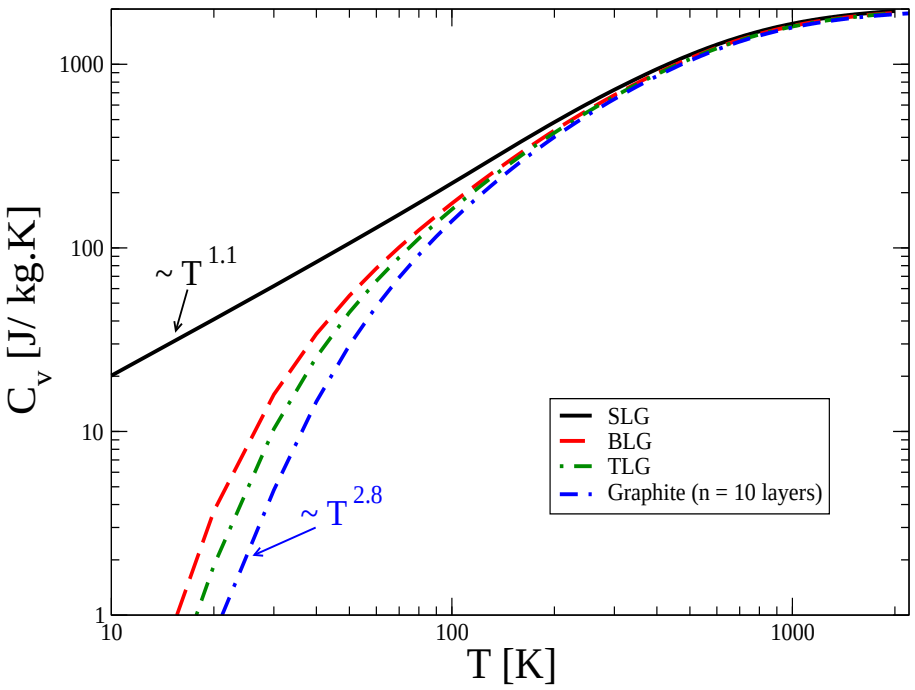

Figure 7.2: Specific heat C_v for multilayer graphene sheets.

from the presence of layer couplings, i.e. due to non-zero values of C_{33} and C_{44}, in BLG. There is a remarkable change in the temperature dependence of $\mathrm{C_v}$ from $\mathrm{C_v} \propto T^{1.1}$ for SLG to $\mathrm{C_v} \propto T^{2.8}$ for BLG.

Phonon conductivity calculations were made by considering the point-defect parameter $A_d = 4.5 \times 10^{-5}$ and the anharmonic scattering parameters: $B_U = 3.18 \times 10^{-25}\mathrm{sK}^{-3}$, and $B_N = 2.12 \times 10^{-25}\mathrm{sK}^{-3}$. The in-plane phonon conductivity calculations were made by considering a sample of size $L_a = 2.9\ \mu$m. Figure 7.3 (upper panel) shows the calculated thermal conductivity for SLG, BLG, and TLG along the basal planes. These calculations reveal that the in-plane thermal conductivity ($K_a \equiv K_{xx} = K_{yy}$) decreases monotonically as the number of layers increases. There is a change of low-temperature dependence from $T^{1.5}$ to $T^{2.7}$ as the dimensionality evolves from strictly two-dimensional for SLG to three-dimensional for bulk graphite. The $T^{2.7}$ temperature dependence of the basal plane thermal conductivity of graphite agrees with the experimental measurement in Ref. [11]. Figure 7.3 (lower panel) shows the thermal conductivities above room temperature along with experimental data available for SLG and bulk graphite. We notice that the difference between the thermal conductivities of SLG and FLG diminishes with increasing temperature, consistent with the trend noted in another theoretical work [4].

The contribution to thermal conductivity by different modes in SLG and TLG are shown in Fig. 7.4. It can be observed that the reduction in thermal conductivity is mainly caused by the reduction in the contribution of the ZA mode. This relatively large reduction in the contribution of the ZA mode as the number of layers increases has been also confirmed by Singh *et al.* [4]. There is insignificant reduction in contributions of the individual LA and TA modes versus the increase in graphene layers number. This is intuitively expected for the in-plane

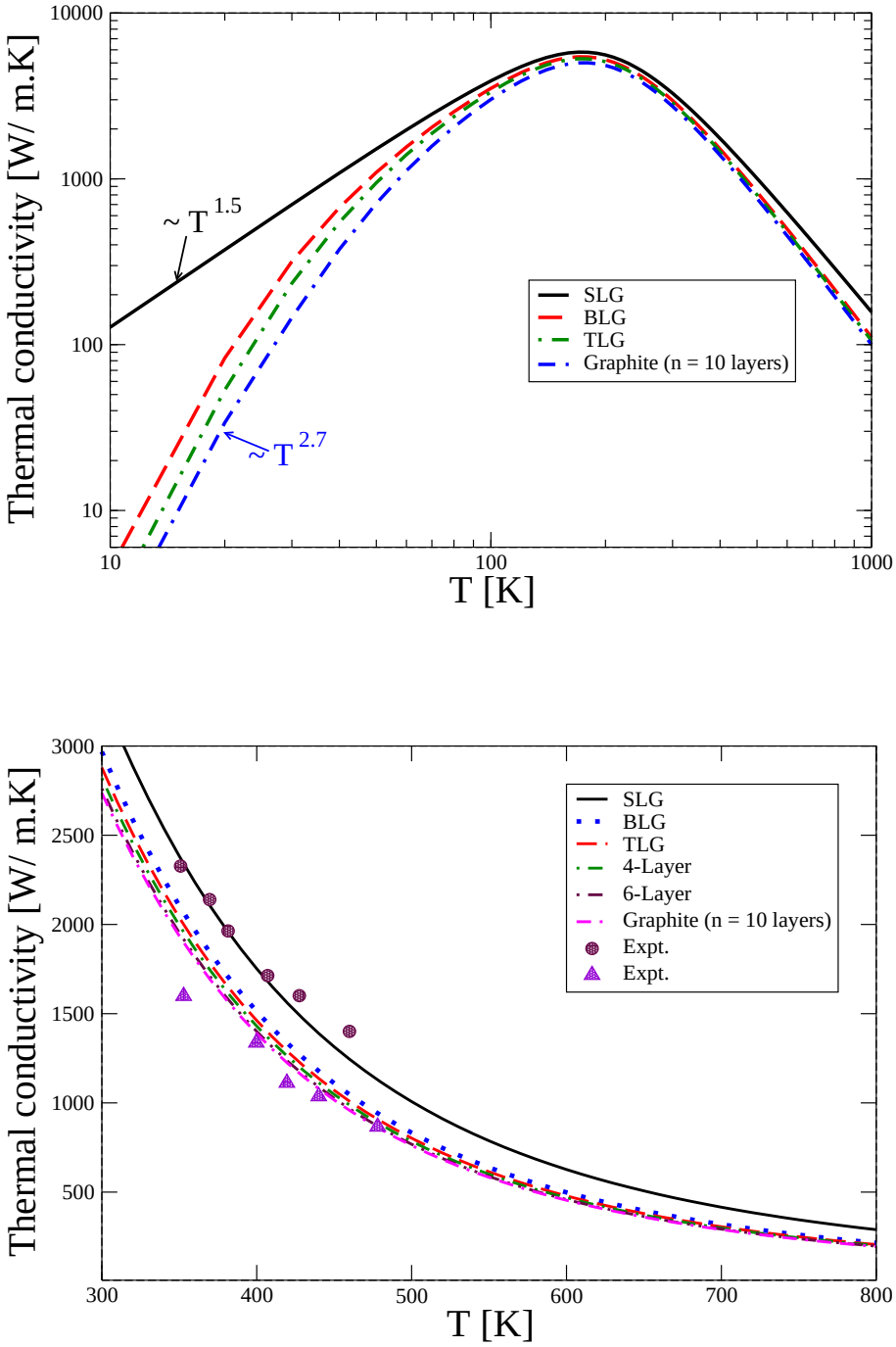

Figure 7.3: (Upper panel): In-plane thermal conductivity for multilayer graphene sheets. (Lower panel): Comparison of computed results with experimental results for SLG and graphite. The symbols represents the experimental measurements: SLG (circles) (Ref. [12]); graphite basal planes (up triangles) (Ref. [13]).

as the addition of layers provides extra pathways for the phonons to conduct heat.

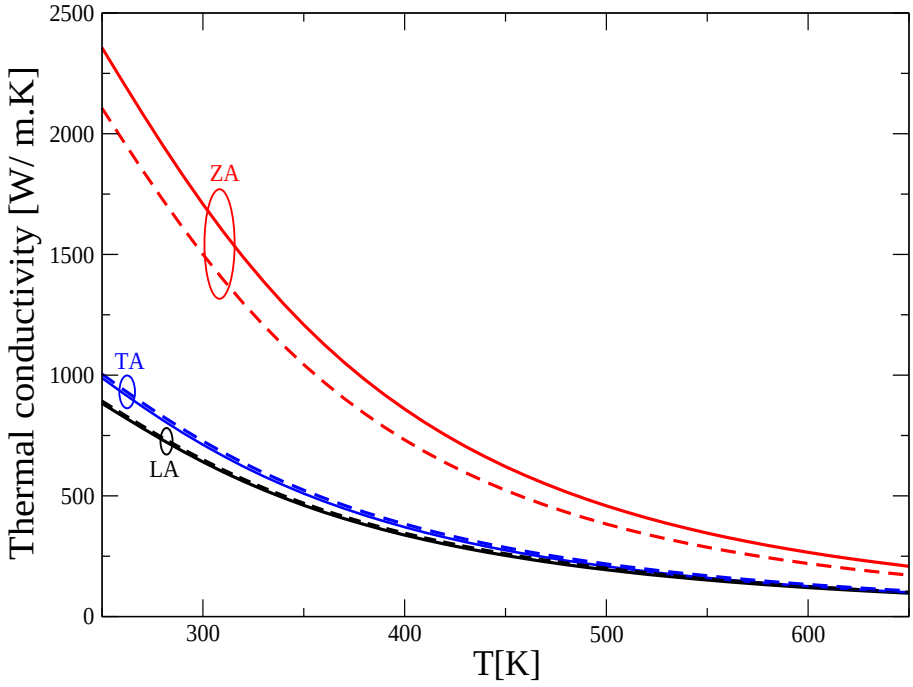

Figure 7.4: Modes contribution to thermal conductivity in SLG and TLG. The solid lines correspond to SLG while the dashed lines correspond to TLG.

It is more interesting to examine the variation of the cross-plane conductivity ($K_c \equiv K_{zz}$) as a function of the number of layers n. Fig. 7.5 shows an increase of K_c as the number of layers increases. The boundary length along the c-axis L_c for FLG was taken as $L_c = (n-1)c$. Of course, $K_c = 0$ for SLG ($n = 1$). For BLG, the K_c starts to emerge with very low values and weak temperature dependency. Higher values of the conductivity are established for FLG. However, for a stand-alone n-layer FLG with the boundary length set to $L_c = (n-1)c$, the temperature dependency remains very weak below room temperature, although there appears to be a mildly increased temperature dependence as n increases. This can be clearly seen from the results for FLG with $n = 3, 4$, and 10.

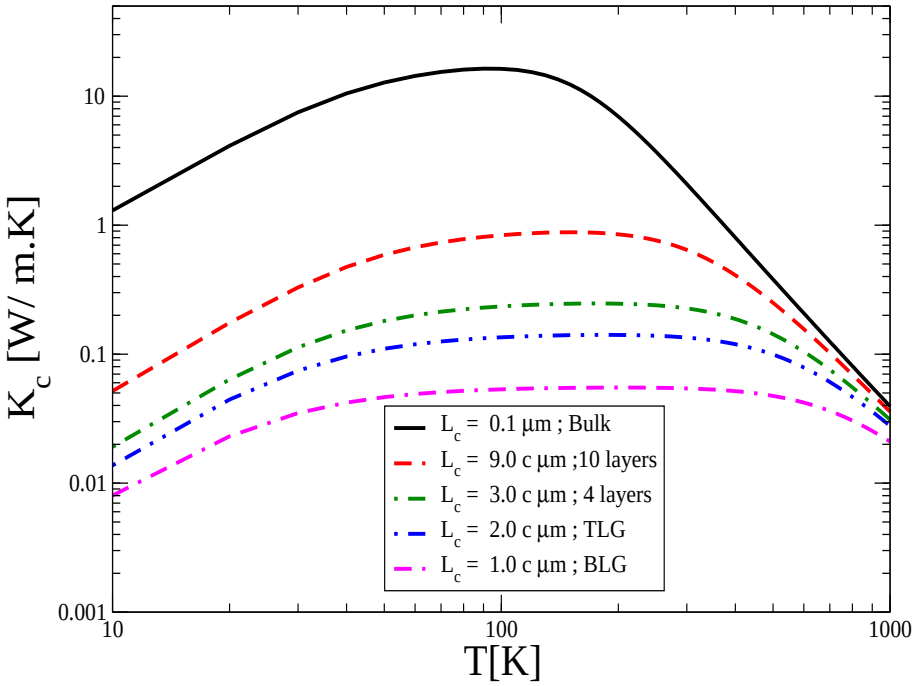

Figure 7.5: Thermal conductivity along c-axis K_c for multilayer graphene sheets.

For BLG as well as FLG, there is a clear temperature dependence and bunching of the conductivity above room temperature, due to increasing role of anharmonic phonon interactions. A finite-size graphite sample can be considered as several FLG stacked upon each other. Calculations for graphite with $L_c = 0.1$ μm suggest that there is a well-established maximum in the K_c *vs.* T curve at around 100 K. The conductivity of bulk graphite at 100 K and for $L_c = 0.1$ μm, K_c is three orders of magnitude higher than that for BLG, and more than an order of magnitude larger than that for FLG with $n = 10$ and $L_c = 9c$. This vindicates the well-known important role of sample size, via boundary scattering of phonons, in determining the magnitude of low-temperature conductivity.

The changes in the room-temperature values of K_a and K_c as a function of the number of atomic planes n in FLG are shown in Fig. 7.6. Compared to SLG, K_a of

BLG is reduced by more than 300 W m^{-1} K^{-1}. The conductivity K_a progressively decreases as the number of layers n increases beyond 2, nearly saturating at the graphite value for $n = 10$.

The changes predicted by our theory for $n = 2, 3$, and 4 are consistent with the measurements made by Ghosh *et al.* [3]. However, a direct comparison of our results with those in Ref. [3] is not possible for two reasons: there is a large error margin in the experimental measurements (e.g. 3000 - 5000 Wm^{-1} K^{-1} at room temperature for single-layer graphene), and the concentration of defects in the samples of different layer numbers is unknown.

In contrast, the variation in K_c is almost linear for ultra-thin FLG (at least up to the layer index $n = 4$). In other words, K_c is governed by L_c. The difference between K_c for FLG and bulk graphite is mainly due to their sample thicknesses: for stand-alone FLG with $n = 10$ the cross-directional sample length is $L_c = 9c$, and for bulk graphite we have considered a film of thickness 0.1μm.

With the development of appropriate experimental techniques, such as the time-domain thermoreflectance (TDTR) method [14] for measuring heat conduction across metal/graphene/oxide interfaces, we anticipate that our theoretical predictions of the cross-plane conductivity results for FLG can be tested in near future.

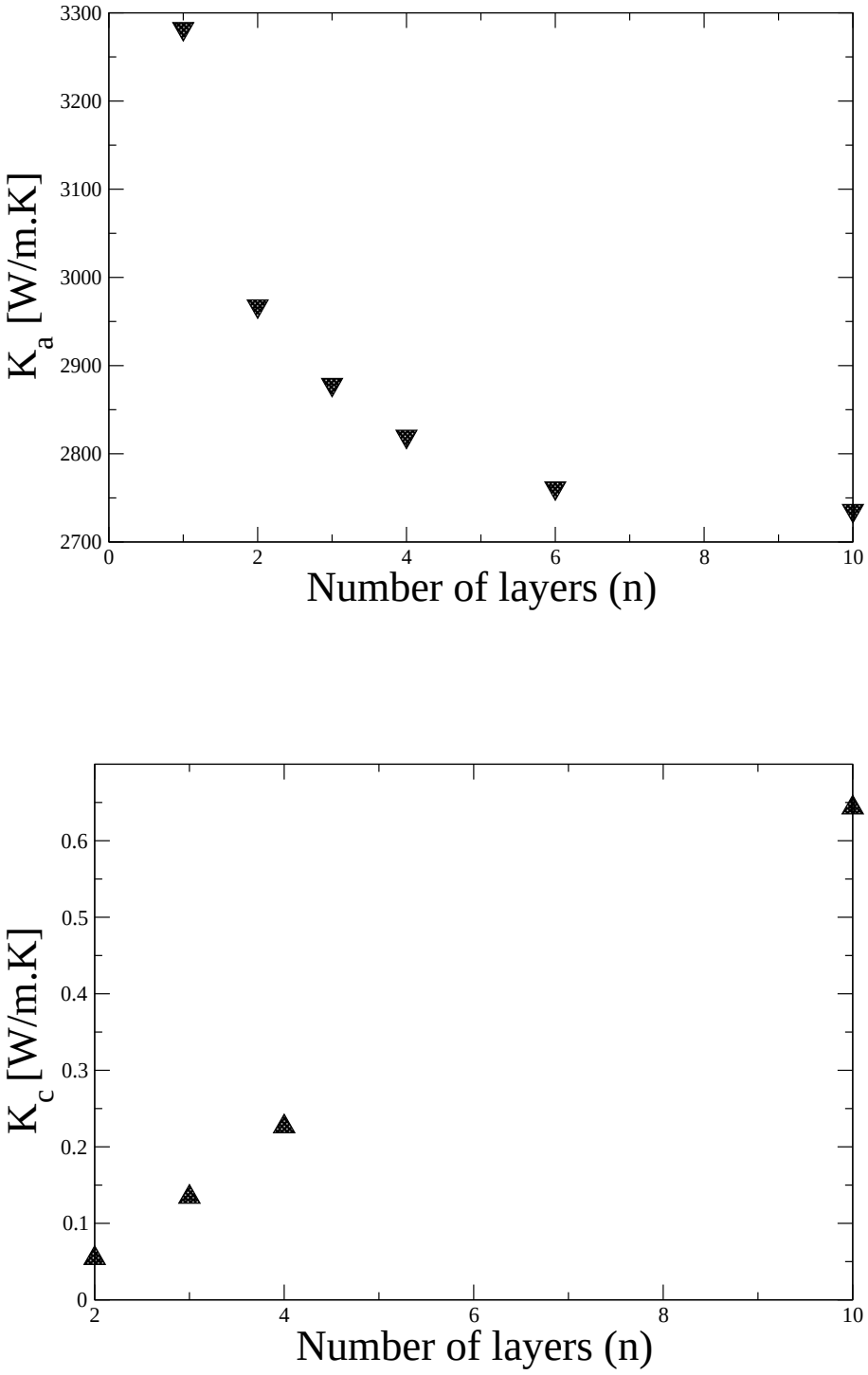

Figure 7.6: Variation of the room-temperature results for K_a (upper panel) and K_c (lower panel) as a function of the number of graphene layers.

7.4 Summary

The establishment of the finite and temperature independent cross-plane conductivity magnitude 0.05 W m^{-1} K^{-1} for BLG is a very interesting result, and points towards a fundamental aspect of the thermal physics of layered materials in general. Based upon our result we suggest that a finite and temperature independent amount of cross-plane low-temperature lattice thermal conductivity should be observed for all materials that can be fabricated as stand-alone bi-layered systems.

Bibliography

[1] W. Bao, F. Miao, Z. Chen, H. Zhang, W. Jang, C. Dames, and C. N. Lau, Nat. Nanotech. **4**, 562 (2009).

[2] W. Liu and M. Asheghi, J. Heat. Transfer. **128**, 75 (2005).

[3] S. Ghosh, W. Bao, D. L. Nika, S. Subrina, E. P. Pokatilov, C. N. Lau, and A. A. Balandin, Nat. Mater. **9**, 555 (2010).

[4] D. Singh, J. Y. Murthy, and T. S. Fisher, J. Appl. Phys. **110**, 044317 (2011). Nat. Mater. **9**, 555 (2010).

[5] Z. Wei, Z. Ni, K. Bi, M. Chen, and Y. Chen, Carbon, **49**, 2653 (2011).

[6] L. D. Landau and E. M. Lifshitz, *Course of Theoretical Physics,* Vol. 7: *Theory of Elasticity* (Pergamon, New York, 1986; Nauka, Moscow, 1987).

[7] R. Saito, R. Matsuo, T. Kimura, G. Dresselhaus, and M.S. Dresselhaus, Chem. Phys. Lett. **348**, 187 (2001).

[8] Y. Shibuta and J. A. Elliott, Chem. Phys. Lett. **512**, 146 (2011).

[9] P. H. Tan, W. P. Han, W. J. Zhao, Z. H. Wu, K. Chang, H. Wang, Y. F. Wang, N. Bonini, N. Marzari, N. Pugno, G. Savini, A. Lombardo, and A. C. Ferrari, Nature Mater. **11**, 294 (2012.)

[10] E. Faizabadi and F. Karbalaii, Proc. of SPIE. **8101**, 81010S (2011).

[11] M. G. Holland, C. A. Klein, and W. D. Straub, J. Phys. Chem. Solids **27**, 903 (1966).

[12] S. Chen, A. L. Moore, W. Cai, J. W. Suk, J. An, C. Mishra, C. Amos. C. W. Magnuson, J. Kang, L. Shi, and R. S. Ruff, ACS Nano **5**, 321 (2011).

[13] G. A. Slack, Phys. Rev. **127**, 694 (1962).

[14] Y. K. Koh, M.-H. Bae, D. G. Cahill, and E. Pop, Nano Lett. **10**, 4363 (2013).

Chapter 8

Summary and Future Work

8.1 Summary

This thesis investigated theoretically the thermal properties of a new unique two dimensional atomic crystal–graphene and graphite, tuning factors affecting thermal properties of graphene, and the evolution of these properties from 2D graphene to bulk graphite. The thermal conductivities of graphene and graphite have been studied using Callaway's effective relaxation time theory and by employing analytical expressions for phonon dispersion relations and vibrational density of states based on the semicontinuum model by Nihira and Iwata proposed by Komatsu and Nagamiya. An overview on graphene physical properties, preparation methods, along with its potential applications have been summarised in chapter 2.

In the phonon dispersion relations for graphene and graphite, there are two acoustic modes of vibrations, in-plane (LA and TA) and out-of-plane (ZA) modes. For these modes, there are two aspects of vibrations, low-frequency layer vibrations and high-frequency atomic vibration. Also, these vibrations are contributing into two components, vibrations along and perpendicular to the basal planes. The

in-plane modes in graphene and graphite are almost similar as observed in chapter 3. However, there is a very slight dissimilarity for the out-of-plane modes which have high contribution than that in graphene.

While the phonon density of states of the in-plane modes at low frequencies shows a linear behaviour in graphene and a nonlinear one in graphite, the phonon density of states of the out-of-plane modes is frequency independent in graphene, but it shows an almost linear dependency on frequencies in graphite. In addition, the phonon density of states of the out-of-plane modes are two orders of magnitude higher than the phonon density of states of the in-plane modes in graphene or graphite. At high temperatures, the specific heat of graphene and graphite are almost identical except at very low temperatures. The low-temperature behaviour of the specific heat for graphene and graphite are tabulated in chapter 4 along with the behaviour of the phonon density of states for both allotropes at low frequencies. It has been clearly noticed that the contribution from the ZA branch is larger than either LA or TA branch at all temperatures up to 2500 K. At 300 K, the contribution from the ZA phonons is approximately 3.1 and 7.2 times larger than the contribution from the TA and LA phonons, respectively.

In chapter 5, the theory of thermal conductivity has been discussed. The approximations of single-mode-relaxation time and effective single-mode-relaxation time have been introduced within the frame of the Boltzmann transport equation. The Callaway theory has been employed in full for computing the thermal conductivity of suspended graphene. It is found that consideration of the momentum conserving nature of three-phonon Normal processes is very important for explaining the magnitude as well as the temperature dependence of the experimentally measured results. At room temperature, the N-drift contribution (the correction term in Callaway's theory) provides 94% addition to the result obtained from the

single-mode relaxation time theory, clearly suggesting that the single-mode relaxation time approach is inadequate for describing the phonon conductivity of graphene. Apart from explaining the experimentally measured data (available in the temperature range 300 - 500 K), the theory suggests that, depending on the level of defects and imperfections, the maximum values of the conductivity may lie in the range of 5000 - 7000 W m^{-1} K^{-1} between 100 - 150 K, and in the range 3000 and 3500 W m^{-1} K^{-1} at room temperature.

The thermal conductivity in graphene, along the graphite basal planes, and along the graphite c-axis have been evaluated in chapter 6. It has been found that the thermal conductivity of graphene is larger than that in graphite basal planes. The c-axis thermal conductivity is significantly lower (two orders of magnitude) than graphene thermal conductivity. At low temperatures (up to 40 K), the thermal conductivity varies as $T^{1.6}$, $T^{2.4}$, and $T^{1.4}$ for graphene, in the graphite basal plane, and along the graphite c axis, respectively. This suggests that the strength of thermal conductivity dependency on temperature decreases due to the decrease in the dimensions of the system. Effects of strain, ^{13}C isotope, and edge roughness on graphene thermal conductivity are evaluated and discussed. Incorporation of the ^{13}C isotope produced significant reduction in the conductivity of graphene in the temperature range 50–300 K. The maximum reduction in graphene thermal conductivity is found at 200 K of 49% for 50% ^{13}C.

In the presence of tensile strain, the specific heat of graphene increases, but the conductivity can decrease or increase depending on the level of the purity and temperature of the sample. It has been shown that the thermal conductivity of graphene can be significantly reduced with the combination of defect concentration and tensile strain. The reduction is more significant for larger defect concentrations. For the high defect concentration $A_d = 9 \times 10^{-4}$, we have estimated

40-50% reduction in the conductivity over the wide temperature range 150-600 K. The increase in the edge roughness leads to a significant reduction in the thermal conductivity of graphene ribbons.

The evolution of thermal properties from graphene to graphite as a function of layer thickness and temperature has been reported in chapter 7. The onset of the inter-layer compressional elastic constant C_{33} and the shear elastic constant C_{44} result in a large difference between the magnitudes and temperature dependencies of the specific heat and in-plane lattice thermal conductivity of bi-layer graphene (BLG) and single-layer graphene (SLG). The changes between BLG and few-layer graphene (FLG) decrease with increase in the number of layers. The cross-plane lattice thermal conductivity increases almost linearly with the number of layers in ultra-thin FLG. The existence of the finite and temperature independent cross-plane conductivity magnitude of 0.05 W m^{-1} K^{-1} for BLG is a very interesting result, and points towards a general basic aspect of the thermal physics of layered crystals.

8.2 Future Work

The work carried out in this thesis can be extended by taking the elastic constants contained in the expressions of the phonon dispersion relation as a function of temperature. The roles of these temperature-dependent parameters in the heat conduction mechanism for graphene and graphite are useful to be investigated.

Thermal conductivity of supported graphene is highly degraded by the effect of substrate. Graphene is supposed to possess high thermal conductivity in graphene-based electronic devices where graphene is placed upon dielectric substrates. Studying the effect of these substrates on the phonon propagation in graphene

is urgently needed in order to determine the criteria to be met in selecting best substrates.

Recently, metal-graphene composites have emerged as a means to produce hybridised properties, leading to electrically and thermally functional materials. It is important to have a good understanding of the thermal conductance mechanisms at the interfaces in order to develop cutting-edge thermal devices.

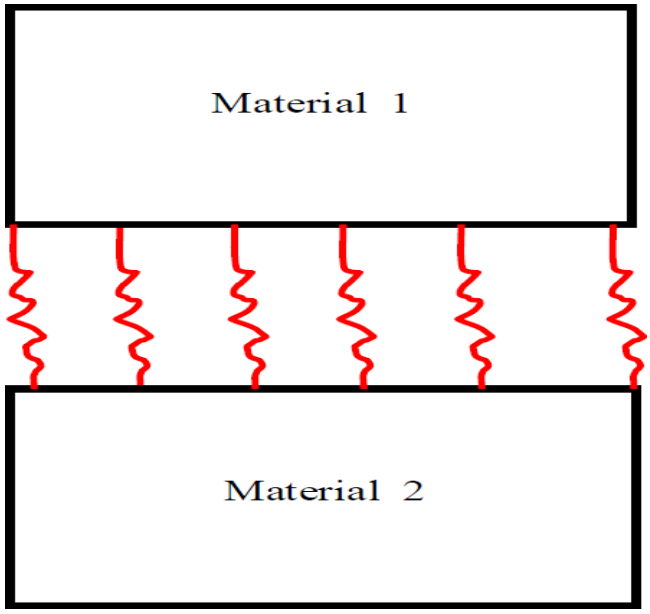

Figure 8.1: Schematic illustration of two dissimilar materials connected by springs representing the bonding force between the atoms.

A discontinuity in temperature occurs at the interface between two different materials will establish a heat current described by a thermal-boundary conductance. This was first noticed by Kapitza in 1941 [1], and universally referred to as the Kapitza resistance or conductance. Thermal conductance between interfaces in solids has been modelled using the acoustic mismatch model (AMM) and the diffusive mismatch model (DMM) which both assume perfect contact at the in-

terface. In the light of the AMM model, all incident phonons are assumed to be totally transmitted through the interface without being reflected or scattered. The thermal interface conductance from a metal film to graphene is given by [2, 3]

$$K = \frac{1}{4}\frac{\hbar^2}{k_B T^2}\sum_p \int_{\omega_{min}}^{\omega_{max}} \xi_{1,p}^{1\to 2}\omega^2 v_{1,p}\,\bar{n}(\bar{n}+1)D_1(\omega)d(\omega), \tag{8.1}$$

where $\xi^{1\to 2}$ is the phonon transmission probability of mode p from metal (material 1) to graphene (material 2) (see Fig.8.1), and $D_1(\omega)$ is the phonon density of states in (material 1). The transmission probability is written as [4]

$$\xi_p^{1\to 2} = \frac{4z_{1,p}z_{2,p}}{(z_{1,p}+z_{2,p})^2 + \frac{\omega^2}{F^2}(z_1 z_2)^2}, \tag{8.2}$$

where $z_{1,p} = \rho_1 v_{1,p}$ is the acoustic impedance which is the product of mass density ρ and the phonon velocity, and F is the spring constant per unit area. A further simplification can be made by considering an average velocity of the LA and TA modes for both metal and graphene, this means that the phonon transmission probability of LA and TA modes from the metal to graphene is equal.

We have made an initial attempt towards calculating the thermal conductance of copper-graphene system and the result is presented in Fig. 8.2. Very weak dependence of the interface thermal conductance on temperature is noticed for $T > 200$ K. This behaviour is reported by another theoretical study [5]. However, this study was investigating thermal conductance for copper-four-layer-graphene and it is found to be $120\,\mathrm{MWm^{-2}K}$ at room temperature. Also, they mentioned that the copper-monolayer-graphene thermal conductance is about $500\,\mathrm{MWm^{-2}K}$ at room temperature. Thermal conductance between metal and FLG, graphite basal planes, graphite c-axis will be interesting to investigate in the future. The values that have been taken in the calculation for the transmission co-

efficient are: the average phonon velocity in copper ($3.30 \times 10^5 \mathrm{cm/s}$), the average phonon velocity in graphene ($1.66 \times 10^6 \mathrm{cm/s}$), copper mass density ($8.96\ \mathrm{g/cm^3}$), and graphene mass density ($2.3\ \mathrm{g/cm^3}$, as graphite). For phonon density of states in copper, the Debye temperature is taken to be 315 K based on its use as a suitable fitting parameter against the experimental data. This preliminary work will be extended in future.

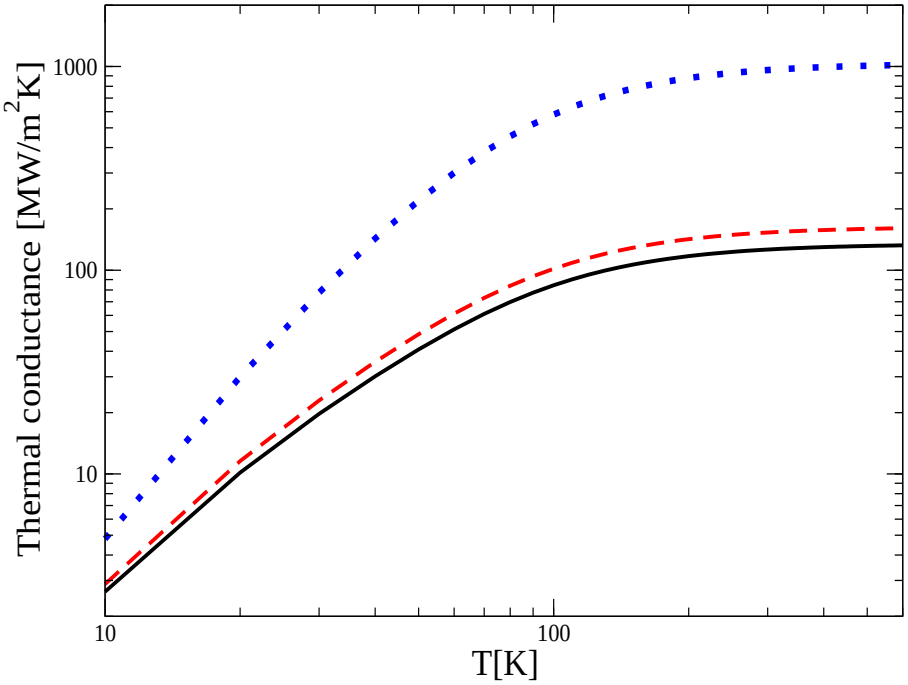

Figure 8.2: Thermal interface conductance between copper and monolayer graphene with arbitrarily chosen values for F which depends on the strength of the binding force at the interface. The values of F are: 0.9×10^{19} (solid line), 1.9×10^{19} (dashed line), and 3.0×10^{19} g. cm^{-2}. s^{-2} (dotted line).

Bibliography

[1] P. L. Kapitza, J. Phys. USSR **4**, 181 (1941).

[2] M. Kazan, Appl. Phys. Lett. **95**, 141904 (2009).

[3] J. C. Duda, J. L. Smoyer, P. M. Norris, and P. E. Hopkins, Appl. Phys. Lett. **95**, 031912 (2009).

[4] R. Prasher, Appl. Phys. Lett. **94**, 041905 (2009).

[5] S-W. Chang, A. K. Nair, and M. J. Buehler, J. Phys.: Condens. Matter **24**, 245301 (2012).

Appendix A

Komatsu approach for phonon dispersion

A.1 Introduction

Graphite crystal considered as a system of thin elastic plates separated by a constant distance. The distance between the carbon atoms which lie in the neighbouring atomic layers is 3.40Å, which is remarkably larger than the atoms in the same layer, which is 1.42Å. A hexagonal crystal had in general five independent elastic constants, $C_{11}, C_{12}, C_{13}, C_{33},$ and C_{44}. For the vibrations of the layers in which the atomic displacements are confined to its plane, one should deal with only two independent constants, C_{11} and C_{12}. A hexagonal layer can therefore be considered as a continuous isotropic medium. The velocities of the transverse and the longitudinal waves in it are

$$v_l = \sqrt{\frac{E}{2\rho(1+\sigma)}}, \qquad v_t = \sqrt{\frac{E}{\rho(1-\sigma^2)}}, \tag{A.1}$$

where ρ, E, and σ are the volume density, the Young's modulus, and the Poisson's ratio respectively. It is more convenient to introduce constants which refer to

surface rather than to volume. We shall define ρ' and E' as follows:

$$\rho' = c\rho, \qquad E' = cE. \tag{A.2}$$

A.2 Equations of a two-dimensional vibrations of a layer

Komatsu [1] has started with the following equations of vibrations:

$$\frac{\partial^2 u_n}{\partial t^2} = \frac{E'}{\rho'(1-\sigma^2)}\left\{\frac{\partial^2 u_n}{\partial x^2} + \frac{1}{2}(1-\sigma)\frac{\partial^2 u_n}{\partial y^2} + \frac{1}{2}(1+\sigma)\frac{\partial^2 v_n}{\partial x \partial y}\right\}, \tag{A.3a}$$

$$\frac{\partial^2 v_n}{\partial t^2} = \frac{E'}{\rho'(1-\sigma^2)}\left\{\frac{1}{2}(1-\sigma)\frac{\partial^2 v_n}{\partial x^2} + \frac{\partial^2 v_n}{\partial y^2} + \frac{1}{2}(1+\sigma)\frac{\partial^2 u_n}{\partial x \partial y}\right\}, \tag{A.3b}$$

$$\frac{\partial^2 w_n}{\partial t^2} = -b^2\left(\frac{\partial^4 w_n}{\partial x^4} + 2\frac{\partial^4 w_n}{\partial x^2 \partial y^2} + \frac{\partial^4 w_n}{\partial y^4}\right) + \mu^2(w_{n+1} + w_{n-1} - 2w_n), \tag{A.3c}$$

where u_n, v_n, and w_n are the displacements of a material points (x, y) in the n-th layer in the $x-$, $y-$, and $z-$directions respectively, and b^2 is related to the bending modulus. If the strain energy φ is taken into account, then for Small interlayer shearing strains

$$\begin{aligned}\varphi = \frac{c.C_{44}}{4}\sum_n \iint \Bigg\{ &\left(\frac{u_{n+1}-u_n}{c} + \frac{\partial w_n}{\partial x}\right)^2 + \left(\frac{u_n - u_{n-1}}{c} + \frac{\partial w_n}{\partial x}\right)^2 \\ &+ \left(\frac{v_{n+1}-v_n}{c} + \frac{\partial w_n}{\partial y}\right)^2 + \left(\frac{v_n - v_{n-1}}{c} + \frac{\partial w_n}{\partial y}\right)^2 \Bigg\} dxdy.\end{aligned} \tag{A.4}$$

The kinetic energy T is

$$T = \sum_n \iint \frac{\rho'}{2}\left\{\left(\frac{\partial u_n}{\partial t}\right)^2 + \left(\frac{\partial v_n}{\partial t}\right)^2 + \left(\frac{\partial w_n}{\partial t}\right)^2\right\} dxdy, \tag{A.5}$$

So by applying Hamilton's principle,

$$\delta \int_{t_1}^{t_2} (T - \varphi) dt = 0, \tag{A.6}$$

the following equations are obtained:

$$\frac{\partial^2 u_n}{\partial t^2} = \frac{\zeta}{c^2}(u_{n+1} + u_{n-1} - 2u_n) + \frac{\zeta}{2c}\left(\frac{\partial w_{n+1}}{\partial x} - \frac{\partial w_{n-1}}{\partial x}\right), \tag{A.7a}$$

$$\frac{\partial^2 v_n}{\partial t^2} = \frac{\zeta}{c^2}(v_{n+1} + v_{n-1} - 2v_n) + \frac{\zeta}{2c}\left(\frac{\partial w_{n+1}}{\partial y} - \frac{\partial w_{n-1}}{\partial y}\right), \tag{A.7b}$$

$$\frac{\partial^2 w_n}{\partial t^2} = \zeta\left(\frac{\partial^2 w_n}{\partial x^2} + \frac{\partial^2 w_n}{\partial y^2}\right) + \frac{\zeta}{2c}\left(\frac{\partial u_{n+1}}{\partial x} - \frac{\partial u_{n-1}}{\partial x} + \frac{\partial v_{n+1}}{\partial y} - \frac{\partial v_{n-1}}{\partial y}\right), \tag{A.7c}$$

where $\zeta = C_{44}/\rho$. By adding the r.h.s. of Eqs.(A.7a), (A.7b), and (A.7c) to the r.h.s of Eqs. (A.3a), (A.3b), and (A.3c) respectively, the new equations of vibrations can be expressed as

$$\begin{aligned}\frac{\partial^2 u_n}{\partial t^2} = {} & \frac{E'}{\rho'(1-\sigma^2)}\left\{\frac{\partial^2 u_n}{\partial x^2} + \frac{1}{2}(1-\sigma)\frac{\partial^2 u_n}{\partial y^2} + \frac{1}{2}(1+\sigma)\frac{\partial^2 v_n}{\partial x \partial y}\right\} + \frac{\zeta}{c^2}(u_{n+1} + u_{n-1} - 2u_n) \\ & + \frac{\zeta}{2c}\left(\frac{\partial w_{n+1}}{\partial x} - \frac{\partial w_{n-1}}{\partial x}\right),\end{aligned} \tag{A.8}$$

$$\begin{aligned}\frac{\partial^2 v_n}{\partial t^2} = {} & \frac{E'}{\rho'(1-\sigma^2)}\left\{\frac{1}{2}(1-\sigma)\frac{\partial^2 v_n}{\partial x^2} + \frac{\partial^2 v_n}{\partial y^2} + \frac{1}{2}(1+\sigma)\frac{\partial^2 u_n}{\partial x \partial y}\right\} + \frac{\zeta}{c^2}(v_{n+1} + v_{n-1} - 2v_n) \\ & + \frac{\zeta}{2c}\left(\frac{\partial w_{n+1}}{\partial y} - \frac{\partial w_{n-1}}{\partial y}\right),\end{aligned} \tag{A.9}$$

$$\begin{aligned}\frac{\partial^2 w_n}{\partial t^2} = {} & + \frac{\zeta}{2c}\left(\frac{\partial u_{n+1}}{\partial x} - \frac{\partial u_{n-1}}{\partial x} + \frac{\partial v_{n+1}}{\partial y} - \frac{\partial v_{n-1}}{\partial y}\right), \\ & - b^2\left(\frac{\partial^4 w_n}{\partial x^4} + 2\frac{\partial^4 w_n}{\partial x^2 \partial y^2} + \frac{\partial^4 w_n}{\partial y^4}\right) + \mu^2(w_{n+1} + w_{n-1} - 2w_n) + \zeta\left(\frac{\partial^2 w_n}{\partial x^2} + \frac{\partial^2 w_n}{\partial y^2}\right),\end{aligned} \tag{A.10}$$

In the above equations, $v_{\mathrm{LA}} = \sqrt{E'/\rho'(1-\sigma^2)}$, and
$v_{\mathrm{TA}} = \sqrt{E'/2\rho'(1+\sigma)} = v_{\mathrm{LA}}\sqrt{(1-\sigma)/2}$.

A.3 Solution of the Equations of Vibrations

The general solution is

$$\begin{aligned} u_n &= U.\exp\{2\pi i(\sigma_x x + \sigma_y y + \sigma_z nc - \nu t)\}, \\ v_n &= V.\exp\{2\pi i(\sigma_x x + \sigma_y y + \sigma_z nc - \nu t)\}, \\ w_n &= W.\exp\{2\pi i(\sigma_x x + \sigma_y y + \sigma_z nc - \nu t)\}, \end{aligned} \tag{A.11}$$

where ν is the phonon frequency. The following simultaneous equations obtained are

$$\begin{aligned} 0 = {} & [v_{\mathrm{LA}}^2\{\sigma_x^2 + (1/2)(1-\sigma)\sigma_y^2\} + (\zeta/c^2\pi^2)\sin^2\pi c\sigma_z - \nu^2]U \\ & + [(1/2)(1+\sigma)\sigma_x\sigma_y v_{\mathrm{LA}}^2]V \\ & + [(\zeta/2\pi c)\sigma_z \sin 2\pi c\sigma_z]W, \end{aligned} \tag{A.12}$$

$$\begin{aligned} 0 = {} & [(1/2)(1+\sigma)\sigma_x\sigma_y v_{\mathrm{LA}}^2]U \\ & + [v_{\mathrm{LA}}^2\{\sigma_x^2 + (1/2)(1-\sigma)\sigma_y^2\} + (\zeta/c^2\pi^2)\sin^2\pi c\sigma_z - \nu^2]V \\ & + [(\zeta/2\pi c)\sigma_y \sin 2\pi c\sigma_z]W, \end{aligned} \tag{A.13}$$

$$\begin{aligned} 0 = {} & [(\zeta/2\pi c)\sigma_z \sin 2\pi c\sigma_z]U \\ & + [(\zeta/2\pi c)\sigma_y \sin 2\pi c\sigma_z]V \\ & [4\pi^2 b^2(\sigma_x^2 + \sigma_y^2)^2 + (\mu^2/\pi^2)\sin^2\pi c\sigma_z + \zeta(\sigma_x^2 + \sigma_y^2) - \nu^2]W. \end{aligned} \tag{A.14}$$

The value of ζ is expected to be small, so that the non-diagonal terms can be neglected such as

$$\frac{\zeta}{2\pi c}\begin{pmatrix}\sigma_x \\ \sigma_y\end{pmatrix} \cdot \sin 2\pi c\sigma_z \begin{pmatrix} U \\ V \\ W \end{pmatrix} \tag{A.15}$$

The secular equation gives the following three roots:

$$\nu_1^2 = v_{\mathrm{LA}}^2(\sigma_x^2 + \sigma_y^2) + (\zeta/\pi^2 c^2)\sin^2(\pi c\sigma_z) \tag{A.16}$$

$$\nu_2^2 = v_{\mathrm{TA}}^2(\sigma_x^2 + \sigma_y^2) + (\zeta/\pi^2 c^2)\sin^2(\pi c\sigma_z) \tag{A.17}$$

$$\nu_3^2 = 4\pi^2 b^2(\sigma_x^2 + \sigma_y^2)^2 + (\mu/\pi^2)\sin^2 \pi c\sigma_z + \zeta(\sigma_x^2 + \sigma_y^2) \tag{A.18}$$

By substituting ν with ω such that $\nu = \omega/2\pi$, and by taking into account that the wave vectors in Komatsu's derivation are expressed in units of 2π, then $q = 2\pi\sigma$ and the above equations can be expressed as

$$\omega_{\mathrm{LA}}^2 = v_{\mathrm{LA}}^2(q_x^2 + q_y^2) + \frac{4\zeta}{c^2}\sin^2(cq_z/2) \tag{A.19}$$

$$\omega_{\mathrm{TA}}^2 = v_{\mathrm{TA}}^2(q_x^2 + q_y^2) + \frac{4\zeta}{c^2}\sin^2(cq_z/2) \tag{A.20}$$

$$\omega_{\mathrm{ZA}}^2 = b^2(q_x^2 + q_y^2)^2 + 4\mu^2\sin^2(cq_z/2) + \zeta(q_x^2 + q_y^2) \tag{A.21}$$

These equations are the phonon dispersion relations for quasi two-dimensional system.

Appendix B

Komatsu approach for Phonon density of states for graphite

B.1 Frequency Distribution Functions

In Appendix A.3, frequency formulas have been obtained for the in-plane waves. For these waves, the contours $\nu = \text{const.}$ are the surfaces of revolution about the σ_z axis in the $\sigma-$space. As seen in Fig. B.1, for all modes, the constant frequency contours are ellipsoids of revolution in this semicontinuum model. In the case of in-plane modes, these constant frequency contours form prolate (cigar-shaped) ellipsoids with the major axis along σ_a direction. In the case of out-of-plane modes, the constant frequency contours are prolate (disc-shaped) with the major axis along the σ_a direction.

The volumes enclosed by one of these surfaces for in-plane and out-of-plane modes are:

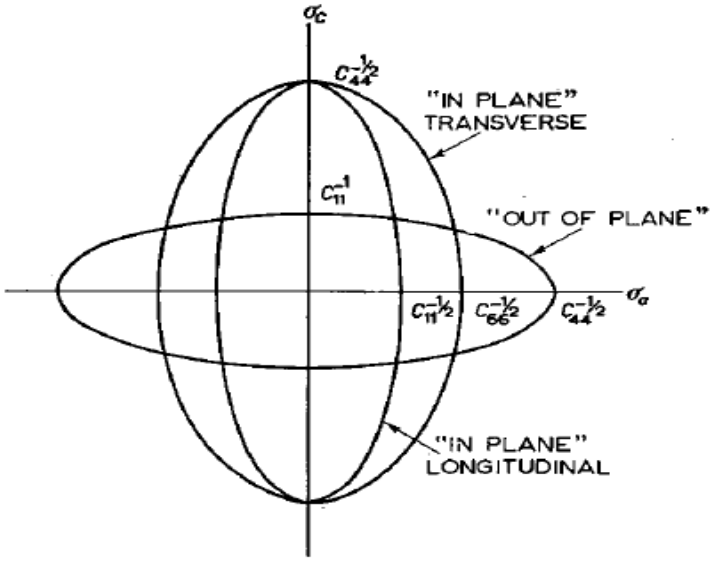

Figure B.1: Contours of constant frequency for graphite in momentum space, for low-frequency modes [2].

B.1.1 In-plane modes

(i) For $\nu \leq \nu_z$

$$V(\nu) = \frac{2\pi}{v_i^2} \int_0^{(1/\pi c)\sin^{-1}(\nu/\nu_z)} (\nu^2 - \nu_z^2 \sin^2 \pi c\sigma_z) \mathrm{d}\sigma_z, \tag{B.1}$$

(ii) For $\nu \geq \nu_z$ The volume would be the space bounded by $\nu = \text{const.}$ and $\sigma_z = \pm 1/2c$

$$V(\nu) = \frac{2\pi}{v^2} \int_0^{1/2c} (\nu^2 - \nu_z^2 \sin^2 \pi c\sigma_z) \mathrm{d}\sigma_z, \tag{B.2}$$

where $\nu_z = \sqrt{\zeta}/\pi c$ and v_i stands for v_l or v_t according as we take either Eq.(A.16) or Eq.(A.17). The frequency distribution functions for the in-plane waves could be obtained from Eq.(B.1) and Eq.(B.2) as follows:

$$f(\nu) = \frac{4V}{v^2 c} \nu \sin^{-1}(\frac{\nu}{\nu_z}), (\nu \leq \nu_z), \tag{B.3}$$

$$f(\nu) = \frac{4V}{v^2 c}\nu\frac{\pi}{2}, (\nu \geq \nu_z), \tag{B.4}$$

where V is the atomic volume.

B.2 Out-of-plane modes

(i) For $\nu \leq \nu_z'$

For the out-of-plane frequency, the volume of the $q-$space is enclosed by $\nu =$const. surface alone when $\nu \leq \nu_z'$ is

$$V(\nu) = \frac{1}{b}\int_0^{(1/\pi c)\sin^{-1}(\nu/\nu_z')} \left[\sqrt{\{(\nu^2 + \zeta^2/16\pi^2 b^2) - \nu_z'^2 \sin^2 \pi c\sigma_z\}} - \zeta/4\pi b\right] \mathrm{d}\sigma_z, \tag{B.5}$$

(ii) For $\nu \geq \nu_z'$

The volume of the $q-$space is enclosed by $\nu =$const. surface and the planes $\sigma_z = \pm 1/2c$ when $\nu \geq \nu_z'$ is

$$V(\nu) = \frac{1}{b}\int_0^{1/2c} \left[\sqrt{\{(\nu^2 + \zeta^2/16\pi^2 b^2) - \nu_z'^2 \sin^2 \pi c\sigma_z\}} - \zeta/4\pi b\right] \mathrm{d}\sigma_z, \tag{B.6}$$

where $\nu_z' = \mu/\pi$. The frequency distribution functions would be as follows:

$$f_3(\nu) = \frac{V\nu}{\pi bc}\int_0^{\sin^{-1}\{1/\sqrt{(1+\zeta^2/16\pi^2 b^2\nu^2)}\}} \frac{\mathrm{d}\varphi}{\sqrt{\left\{1 - \left(\frac{\nu}{\nu_z'}\right)^2 \left(1 + \frac{\zeta^2}{16\pi^2 b^2 \nu^2}\right)\sin^2\varphi\right\}}}, \nu \leq \nu_z'. \tag{B.7}$$

$$f_3(\nu) = \frac{V}{\pi bc}\left(1 + \frac{\zeta^2}{16\pi^2 b^2 \nu^2}\right)^{-1/2}\int_0^{\pi/2} \frac{\mathrm{d}\varphi}{\sqrt{\left\{1 - \left(\frac{\nu_z'}{\nu}\right)^2 \left(1 + \frac{\zeta^2}{16\pi^2 b^2 \nu^2}\right)\sin^2\varphi\right\}}}, \nu \geq \nu_z'. \tag{B.8}$$

Appendix C

Bose-Einstein distribution function

$$\bar{n_s}(\mathbf{q}) = \frac{1}{e^{\frac{\hbar\omega}{k_B T}} - 1} \tag{C.1}$$

If we set $x = \frac{\hbar\omega}{k_B T}$, then Eq.(C.1) becomes

$$\bar{n_p}(\mathbf{q}) = \frac{1}{e^x - 1} \tag{C.2}$$

$$\frac{\partial \bar{n_p}(\mathbf{q})}{\partial T} = \frac{\partial \bar{n_p}(\mathbf{q})}{\partial x} \cdot \frac{\partial x}{\partial T} \tag{C.3}$$

$$\begin{aligned} \frac{\partial \bar{n_p}(\mathbf{q})}{\partial x} &= \frac{\partial}{\partial x}\left(\frac{1}{e^x - 1}\right) = -\frac{e^x}{(e^x - 1)^2} \\ \frac{\partial x}{\partial T} &= \frac{\partial}{\partial T}\left(\frac{\hbar\omega}{k_B T}\right) = -\frac{\hbar\omega}{k_B T^2} \end{aligned}$$

$$\frac{\partial \bar{n_p}(\mathbf{q})}{\partial T} = \frac{\hbar\omega}{k_B T^2} \bar{n_p}(\mathbf{q}) \left(\bar{n_p}(\mathbf{q}) + 1\right) \tag{C.4}$$

Appendix D

The N-drift term

Due to N-processes alone, the rate of change of the total crystal momentum must equal to zero. This can be expressed as

$$\begin{aligned} 0 &= \sum_{\mathbf{q}p} \left(\frac{\partial n_{\mathbf{q}p}}{\partial t} \right)_N \mathbf{q} \\ &= \sum_{\mathbf{q}p} (\mathbf{q}\cdot\mathbf{u}) \frac{\mathbf{q}\cdot\mathbf{u} - \psi_{\mathbf{q}p}}{\tau_N} \bar{n}_{\mathbf{q}p}(\bar{n}_{\mathbf{q}p}+1) \\ &= \sum_{\mathbf{q}p} \left[\frac{(\mathbf{q}\cdot\mathbf{u})^2}{\tau_N} - \frac{(\mathbf{q}\cdot\mathbf{u})\psi_{\mathbf{q}p}}{\tau_N} \right] \bar{n}_{\mathbf{q}p}(\bar{n}_{\mathbf{q}p}+1). \end{aligned} \tag{D.1}$$

The phonon Boltzmann equation reads

$$\left. \frac{\partial n_{\mathbf{q}p}}{\partial t} \right|_{diff} + \left. \frac{\partial n_{\mathbf{q}p}}{\partial t} \right|_{scatt} = 0, \tag{D.2}$$

where the phonon scattering processes considered as the sum of Resistive (R) and Normal (N) phonon scatterings as follows

$$\left. \frac{\partial n_{\mathbf{q}p}}{\partial t} \right|_{scatt} = \left. \frac{\partial n_{\mathbf{q}p}}{\partial t} \right|_{N} + \left. \frac{\partial n_{\mathbf{q}p}}{\partial t} \right|_{R}. \tag{D.3}$$

Equation (D.3) can be expressed as

$$-\mathbf{v}_p(\mathbf{q})\cdot\boldsymbol{\nabla}T\frac{\partial\bar{n}_{\mathbf{q}p}}{\partial T}=\left[-\frac{\mathbf{q}\cdot\mathbf{u}}{\tau_N}\bar{n}_{\mathbf{q}p}(\bar{n}_{\mathbf{q}p}+1)+\frac{\psi_{\mathbf{q}p}}{\tau_N}\bar{n}_{\mathbf{q}p}(\bar{n}_{\mathbf{q}p}+1)+\frac{\psi_{\mathbf{q}p}}{\tau_q}\bar{n}_{\mathbf{q}p}(\bar{n}_{\mathbf{q}p}+1)\right]. \tag{D.4}$$

Introducing a new relaxation time τ^{-1} such that

$$\tau^{-1}=\tau_R^{-1}+\tau_N^{-1} \tag{D.5}$$

and reaclling Eq. (C.4), the above equation can be written as

$$-\mathbf{v}_p(\mathbf{q})\cdot\boldsymbol{\nabla}T\mathbf{q}p\frac{\hbar\omega(\mathbf{q}p)}{k_{\mathrm{B}}T^2}=\psi_{\mathbf{q}p}\left(\frac{1}{\tau_N}+\frac{1}{\tau_R}\right)-\frac{\mathbf{q}\cdot\mathbf{u}}{\tau_N} \tag{D.6}$$

$$\psi_{\mathbf{q}p}=\left(\frac{\mathbf{q}\cdot\mathbf{u}}{\tau_N}-\frac{\hbar\omega(\mathbf{q}p)}{k_{\mathrm{B}}T^2}\,v_p(\mathbf{q})\hat{q}\cdot\boldsymbol{\nabla}T\right)\tau. \tag{D.7}$$

Using the following short-hand notation

$$\langle g\rangle=\sum_{\mathbf{q}p}g_{\mathbf{q}p}\bar{n}_{\mathbf{q}p}(\bar{n}_{\mathbf{q}p}+1). \tag{D.8}$$

Eq. (D.1) can be written as

$$\left\langle\frac{(\mathbf{q}\cdot\mathbf{u})^2}{\tau_N}\right\rangle=\left\langle\frac{(\mathbf{q}\cdot\mathbf{u})\psi_{\mathbf{q}p}}{\tau_N}\right\rangle. \tag{D.9}$$

Substituting Eq.(D.7) in Eq.(D.9) we obtain

$$\left\langle\frac{(\mathbf{q}\cdot\mathbf{u})^2}{\tau_N}\right\rangle=\left\langle\frac{\tau(\mathbf{q}\cdot\mathbf{u})}{\tau_N}\left(\frac{(\mathbf{q}\cdot\mathbf{u})}{\tau_N}-\frac{\hbar\omega(\mathbf{q}p)}{k_{\mathrm{B}}T^2}\,v_p(\mathbf{q})\hat{q}\cdot\boldsymbol{\nabla}T\right)\right\rangle. \tag{D.10}$$

Eq.(D.10) can be written as

$$\left\langle(\mathbf{q}\cdot\mathbf{u})^2\left(\frac{\tau}{\tau_N^2}-\frac{1}{\tau_N}\right)\right\rangle=\left\langle(\mathbf{q}\cdot\mathbf{u})\,\frac{\tau}{\tau_N}\frac{\hbar\omega}{k_BT^2}v_p(\mathbf{q})\hat{q}\cdot\boldsymbol{\nabla}T\right\rangle. \tag{D.11}$$

Let us say that $\mathbf{q}\cdot\mathbf{u}=qu\cos\chi$, then Eq.(D.11) becomes

$$\left\langle q^2u^2\cos^2\chi\left(\frac{\tau}{\tau_N^2}-\frac{1}{\tau_N}\right)\right\rangle=\left\langle qu\cos\chi\frac{\tau}{\tau_N}\frac{\hbar\omega}{k_BT^2}v_p|\boldsymbol{\nabla}T|\right\rangle. \tag{D.12}$$

The value of $|\mathbf{u}|$ can be written as

$$u = -\frac{\hbar|\boldsymbol{\nabla}T|}{k_{\rm B}T^2}\frac{\langle\omega v q\tau\tau_N^{-1}\rangle}{\langle q^2\tau_N^{-1}(1-\tau\tau_N^{-1})\rangle}. \tag{D.13}$$

Substituting u in Eq.(D.7), we can obtain the following expression for $\psi_{\mathbf{q}p}$ in Callaway's approximation:

$$\psi^C_{\mathbf{q}p} = -\frac{\hbar|\boldsymbol{\nabla}T|}{k_{\rm B}T^2}\tau_{\mathbf{q}p}\left[\omega(\mathbf{q}p)v_p(\mathbf{q})\hat{q}\cdot\hat{u} + \frac{\mathbf{q}\cdot\hat{u}}{\tau_N}\frac{\langle\omega v q\tau\tau_N^{-1}\rangle}{\langle q^2\tau_N^{-1}(1-\tau\tau_N^{-1})\rangle}\right]. \tag{D.14}$$

Using this expression for $\psi^C_{\mathbf{q}p}$ in Eq.(5.24), one can write the Callaway's equation for the thermal conductivity as

$$\begin{aligned} K_{\rm C} &= \frac{\hbar^2}{3V_m k_{\rm B}T^2}\left[\langle\tau\omega^2 v_p^2\rangle + \frac{\langle\omega v_p q\tau\tau_N^{-1}\rangle^2}{\langle q^2\tau_N^{-1}(1-\tau\tau_N^{-1})\rangle}\right] \\ &= K_{\rm D} + K_{\rm N-drift} \end{aligned} \tag{D.15}$$

By re-expressing $K_{\rm C}$ in the form

$$K_{\rm C} = \frac{\hbar^2}{3V_m k_{\rm B}T^2}\langle\tau_{\rm C}\omega^2 v_p^2\rangle, \tag{D.16}$$

it is noted that the '*effective*' relaxation time in the Callaway's approximation is

$$\tau_{\rm C} = \tau(1+\frac{\beta}{\tau_N}), \tag{D.17}$$

where β is given by

$$\beta = \frac{q}{\omega(\mathbf{q}p)v_p(\mathbf{q})}\frac{\langle\omega v_p q\tau\tau_N^{-1}\rangle}{\langle q^2\tau_N^{-1}(1-\tau\tau_N^{-1})\rangle}. \tag{D.18}$$

$K_{\rm D}$ and $K_{\rm N-drift}$ can be re-expressed as

$$K_{\rm D} = \frac{\hbar^2}{3V_m k_B T^2}\sum_p\int {\rm d}\omega\omega_p^2(q)v_p^2(q)\tau\bar{n}(\bar{n}+1)D(\omega), \tag{D.19}$$

$$K_{\rm N-drift} = \frac{\hbar^2}{3V_m k_B T^2}\sum_p\frac{\left[\int {\rm d}\omega D(\omega)\omega^2 v_p^2\tau\tau_N^{-1}\bar{n}(\bar{n}+1)\right]^2}{\int {\rm d}\omega D(\omega)\omega^2 v_p^2\tau_N^{-1}(1-\tau\tau_N^{-1})\bar{n}(\bar{n}+1)}. \tag{D.20}$$

It is clear that $\tau_{\rm C} = \tau_{smrt}$ when $\beta = 0$.

Appendix E

Tensile strain on graphene

Strain arises when the bonds in the crystal are compressed or stretched out of equilibrium. The presence of strain can affect the thermal properties of materials, when tensile strain is applied , this usually resulting in phonon mode softening, and the opposite for compressive strain. Experimentally, Raman spectroscopy is the main technique to investigate the physics of phonons in strained graphene [3].

Theoretically, the effect of strain could be studied by using the continuum theory of elasticity. Using the standard theory of free-standing membranes, the Hamiltonian is [4]

$$H = \int d^2\vec{\boldsymbol{r}} \left\{ \frac{\rho_{2\mathrm{D}}}{2}[(\partial_t u_x)^2 + (\partial_t u_y)^2 + (\partial_t h)^2] + \frac{b^2\rho_{2\mathrm{D}}}{2}\left(\frac{\partial^2 h}{\partial x^2} + \frac{\partial^2 h}{\partial y^2}\right)^2 + \frac{\lambda}{2}\left(\partial_x u_x + \partial_y u_y + \frac{(\partial_x h)^2 + (\partial_y h)^2}{2}\right)^2 + \bar{\mu}\left[\left(\partial_x u_x + \frac{(\partial_x h)^2}{2}\right)^2 + \left(\partial_y u_y + \frac{(\partial_y h)^2}{2}\right)^2 + \frac{[\partial_x u_x + \partial_y u_x + (\partial_x h)(\partial_y h)]^2}{2}\right]\right\} \tag{E.1}$$

where $\vec{\mathbf{u}}$ is the in-plane displacement vector and h is the displacement in the out-of-plane direction.

If the effect of the in-plane tension is ignored $\partial_i u_j = 0$, the out-of-plane displacements are considered, and the quadratic terms in h are neglected, we obtain $\omega_3^2 = b^2 q_a^4$. This is the well known dispersion relation for the out-of-plane flexural mode. If an isotropic strain ϵ where $\partial_x u_x = \partial_y u_y = \epsilon$ is applied to the graphene lattice constant, then strain can be incorporated in Eq. E.1. The effective Hamiltonian H_{eff} for h, expanded to second order becomes [4]

$$H_{eff} = \int d^2\vec{\boldsymbol{r}} \left\{ \frac{\rho_{\text{2D}}}{2}(\partial_t h)^2 + \frac{b^2\rho_{\text{2D}}}{2}\left(\frac{\partial^2 h}{\partial x^2} + \frac{\partial^2 h}{\partial y^2}\right)^2 + (\lambda+\bar{\mu})\epsilon[(\partial_x h)^2 + (\partial_y h)^2] \right\}. \tag{E.2}$$

The new dispersion relation of the flexural phonons under strain is

$$\omega_3^2 = b^2 q_a^4 + \frac{2}{\rho_{\text{2D}}}(\lambda+\bar{\mu})\epsilon q^2. \tag{E.3}$$

Appendix F

The Shear Mode of Few-layer graphene

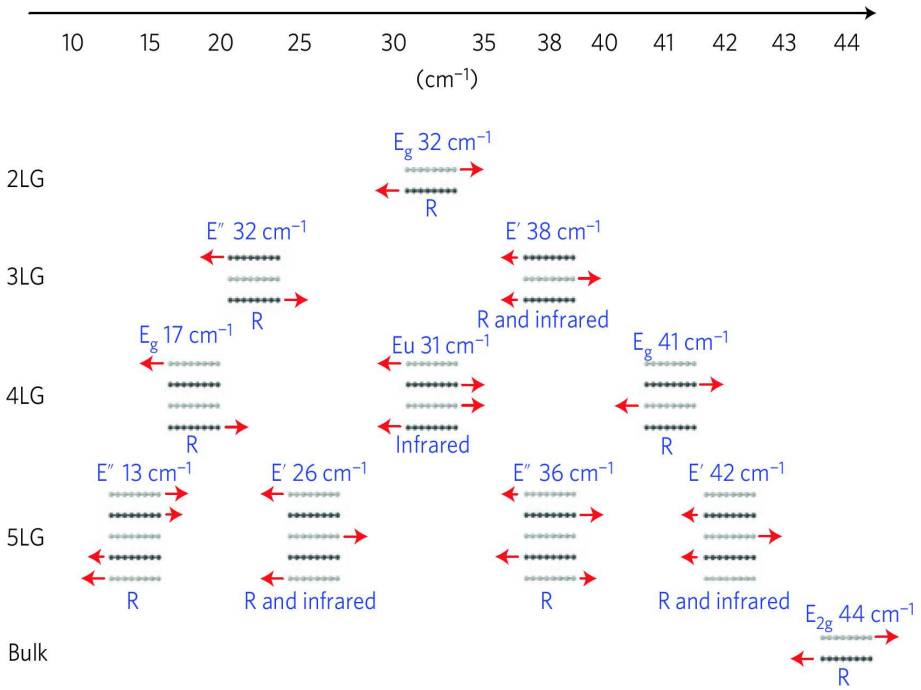

Figure F.1: The frequencies of the in-plane shear modes for bi-layer graphene through to five-layer graphene and bulk graphite. Taken from Ref. [5].

Bibliography

[1] K. Komatsu, J. Phys. Soc. Japan **10**, 346 (1955).

[2] J. C. Bowman and J. A. Krumhansl, J. Phys. Chem. Solids **6**, 367 (1958).

[3] T. M. G. Mohiuddin, A. Lombardo, R. R. Nair, G. Savini, R. Jalil, N. Bonini, D. M. Basko, C. Galiotis, N. Marzari, K. S. Novoselov, A. K. Geim, and A. C. Ferrari, Phys. Rev. B **79**, 205433 (2009).

[4] P. L. de Andres, F. Guinea, and M. I. Katsnelson, Phys. Rev. B **86**, 144103 (2012).

[5] P. H. Tan, W. P. Han, W. J. Zhao, Z. H. Wu, K. Chang, H. Wang, Y. F. Wang, N. Bonini, N. Marzari, N. Pugno, G. Savini, A. Lombardo, and A. C. Ferrari, Nature Mater. **11**, 294 (2012.)